UNIVERSITAT DE VALÈNCIA

INSTITUTO DE CIENCIA MOLECULAR

On the photophysics and photochemistry of biological chromophores: An ab initio quantum chemical study

Supervisors:

Dra. Manuela Merchán

Dr. Luis Serrrano Andrés

Dr. Daniel Roca Sanjuán

TESIS DOCTORAL

ANGELO GIUSSANI

VALENCIA 2014

Programa de doctorado en Química Teórica y Modelización Computacional

Dña. Manuela Merchán, Catedrática del Departamento de Química Física y del Instituto de Ciencia Molecular de la *Universitat de València*, D. Luis Serrano Andrés, Profesor Titular de Química Física y del Instituto de Ciencia Molecular de la *Universitat de València*, y D. Daniel Roca Sanjuán, Investigador Contratado del Instituto de Ciencia Molecular de la *Universitat de València*, confirman que la memoria presentada por el doctorando Angelo Giussani con el título "On the photophysics and photochemistry of biological chromophores: An ab initio quantum chemical study" corresponde a su Tesis Doctoral y ha sido realizada bajo su dirección, autorizando mediante este escrito la presentación de la misma.

En Valencia, Enero de 2014

Dra. Manuela Merchán

Dr. Luis Serrano Andrés (1966-2010)

Dr. Daniel Roca Sanjuán

Doctorando: Angelo Giussani

AGRADECIMIENTOS

En primer lugar quiero agradecer a mi familia, gracias a la cual he tenido la posibilidad de estar en la feliz situación en la que hoy me encuentro. Quiero agradecer a mis directores de tesis Manuela Merchán, Luis Serrano Andrés y Daniel Roca Sanjuán. En particular, deseo agradecer a Luis Serrano Andrés, pues fue quien inicialmente me acogió en el grupo Química Cuántica del Estado Excitado de València (*Quantum Chemistry of the Excited State of València*, QCEXVAL) y que guió mis primeros pasos en el mundo de la Química Cuántica de los Estados Excitados. Su enseñanza no quedará olvidada. También quiero agradecer a Manuela Merchán por haberme dado la posibilidad de seguir adelante con mi trabajo de tesis y de haberme guiado en estos años, tanto desde un punto de vista científico como humano. A Daniel Roca Sanjuán por la cuidadosa revisión del presente trabajo. La amable acogida por el Profesor Marco Garavelli en su grupo de Bolonia ha permitido complementar apropiadamente mi formación científica. Quiero agradecer a mis compañeros de grupo y en general a mis compañeros del ICMol, Instituto de Ciencia Molecular, (Antonio Francés Monerris, Javier Segarra Martí, Vicenta Saurí Peris, Juan José Serrano Pérez, Juan Aragó, Pablo Bidanu, Joaquín Calbo y Vicente Pérez Mondéjar) por el ambiente estimulante, sereno y de compañerismo que ha caracterizado mi periodo de doctorado. En particular, quiero agradecer a mi compañero Antonio por su apoyo humano, tanto dentro como fuera del ICMol. Por último, quiero agradecer a toda la unidad de Química Teórica del ICMol, por su siempre pronta disponibilidad.

PREFACE

The main goal of the present thesis is to describe on the basis of high-level ab initio quantum chemical calculations different aspects of the intrinsic response to UV irradiation of some organic chromophores. In particular, the following systems have been studied:

1. 1-aminonaphthalene, a naphthalene derivative whose interest belongs to the research aimed to gather a better understanding of the photophysical properties of simple aromatic chromophores.

2. The indole system, the main emissive source of proteins and the chromophore of the essential amino acid tryptophan and the neurotransmitter serotonin.

3. The thymine-thymine (6-4) adduct, a DNA photolesion whose mechanism of formation is poorly understood.

4. The cytosine nucleobase, a DNA building block chromophore whose photoresponse has been largely studied in the last decade, and it does not appear clear yet.

5. The asulam molecule, a widely used herbicide.

The main radiative and non-radiative deactivation paths have been analyzed for 1-aminonaphthalene, indole, cytosine, and asulam. For the stacked thymine-thymine system we have analyzed the photoinduced formation mechanism of the DNA photolesion thymine-thymine (6-4) adduct. In order to perform the research project, our approach has been based on the determination of the most relevant features characterizing the potential energy hypersurfaces (PEHs) of the involved electronic

states. In this respect, the spontaneous and possible evolutions of a state from a non-equilibrium geometry (a situation that normally takes place when an excited state is populated by radiation) are mainly determined by the corresponding barrierless and energetically accessible paths along its PEH.

The thesis is organized as follows. In the first chapter, a short overview regarding the importance and beauty of photoinduced processes is introduced, together with the underlying motivations that have catalyzed the study of the analyzed systems. The fundamental concepts on which the thesis is based (as for example the idea of PEH, the definition of photophysics and photochemistry, etc) are subsequently explained in the chapter entitled "Theoretical background". In the "Theoretical methods: problems to be solved" chapter, the two main problems that must be solved are described, and the methods used to treat them are illustrated. In the "Results" chapter, the obtained outcomes are provided, highlighting the scientific contest of the performed research and the provided original contributions. In the "Conclusion" chapter the main results for each of the studied systems are then listed. Finally, a summary of the performed work is provided in Spanish.

LIST OF PUBLICATIONS

1. Giussani, A.; Segarra-Martí, J.; Roca-Sanjuán, D.; Merchán, M. Excitation of Nucleobases from a Computational Perspective I: Reaction Paths *Top. Curr. Chem.* **2013**, DOI 10.1007/128_2013_501.

2. Giussani, A.; Pou-Amérigo, R.; Serrano-Andrés, L.; FreireCorbacho, A.; Martínez-García, C.; Fernández, M.; Sarakha, M.; Canle, M.; Santaballa, J. Combined Theoretical and Experimental Study of the Photophysics of Asulam *J. Phys. Chem. A* **2013**, *117*, 2125.

3. Giussani, A.; Serrano-Andrés, L.; Merchán, M.; Roca-Sanjuán, D.; Garavelli, M. Photoinduced Formation Mechanism of the Thymine-Thymine (6-4) Adduct *J. Phys. Chem. B* **2013**, *117*, 1999.

4. Giussani, A.; Merchán, M.; Roca-Sanjuán, D.; Lindh, R. Essential on the Photophysics and Photochemistry of the lndole Chromophore by Using a Totally Unconstrained Theoretical Approach *J. Chem. Theory Comput.* **2011**, *7*, 4088.

5. Montero, R.; Longarte, A.; Peralta Conde, Á.; Redondo, C; Castaño, F.; Gonzalez-Ramírez, I.; Giussani, A.; Serrano-Andrés, L.; Merchán, M. Photophysics of 1-Aminonaphthalene: A Theoretical and Time-Resolved Experimental Study *J. Phys. Chem. A* **2009**, *113*, 13509.

Contents

Chapter 1

Introduction

1.1 The importance of studying photoinduced processes

Light is undoubtedly an important part of our universe. On Earth it is widely present due to solar radiation. It is characterized by extremely interesting properties whose study belongs to the knowledge of the basic elements of Nature. Apart from its intrinsic importance, light induces fundamental processes that are essential for the biological systems of the Earth. Light is in fact the most efficient medium in order to transmit energy and information. Light is the main source of energy on Earth, which is first converted to electrical and next to chemical energy in the so-called photosynthesis [1]. This complex process that takes place in many living organisms (among them green algae and plants) converts carbon dioxide and water into organic material and molecular oxygen. Molecular oxygen can subsequently be used to produce chemical energy in most of the living organisms (including humans) through the fundamental mechanisms of aerobic cellular respiration [1]. Most of the free

molecular oxygen present in the Earth, which is a basic reactant in the so-important aerobic cellular respiration, is produced as a byproduct of photosynthesis. For the aforementioned reasons, it is easily understandable the outstanding importance of the photoinduced process of photosynthesis for life in the Earth. Another fundamental process which is mediated by light is vision. Vision can be regarded as the ability to interpret the light emitted or reflected by the surrounding environment as information, and it constitutes an important sensorial skill in humans and in many animals. Light is consequently used as a precious medium for transmission of information. The first step in order to decode light is of course a photoinduced phenomenon. In human eyes this task is accomplished by different photoreceptors (as, for example, the well studied rhodopsin molecule [2,3]) whose significant response to light interaction is a cis-trans photoisomerization of a carbon-carbon double bound [4]. Besides these beneficial photoinduced processes, others can cause less useful and even deleterious consequences. As a remarkable example of such cases, the interaction of light with the genetic material and, in particular, with its nucleobase constituents may lead to the formation of mutagenic and carcinogenic products. Two major classes of photoproducts have been detected in DNA as a consequence of UV exposure during a sufficient time: the so-called cyclobutane pyrimidine dimers (Pyr<>Pyr) and pyrimidine-pyrimidone (6-4) adducts [5,6]. Interestingly, these photoinduced formation mechanisms have been proven to be efficiently quenched by the intrinsic ability of single canonical nucleobases to rapidly dissipate the absorbed energy, an important property rarely shared with most of the modified nucleobases [7]. Also, very interesting is the fact that such photolesions can be efficiently repaired through photoinduced mechanisms started by the photoactivation of specific enzymes (mainly flavoenzymes) [8,9]. Even if the presented ex-

amples are only a few of the total photoinduced reactions that occur in the biological systems present on Earth, their relevance unambiguously demonstrates the importance of studying photoinduced processes. Such a research is also pushed by different practical applications. For example, the solar radiation is used in solar cell devices to convert light into electricity by means of the photovoltaic effect. In medicine, the interaction of light alone or with a drug is used in the so-called phototherapy [10], which is normally employed to treat some specific illness, as the neonatal jaundice. The study of photoinduced processes is consequently catalyzed by different motivations. Firstly, the simple but vital curiosity that lead us to study photoinduced processes taking actually place in living organisms. Secondly, the importance of understanding photoinduced processes in order to have a clear vision of fundamental mechanisms on which the biological systems of Earth are based on. Finally, by their already existing and promising future applications.

1.2 Studied systems

1.2.1 Basic aromatic biological chromophores

1.2.1.1 1-aminonaphthalene

Natural and artificial chromophores can be considered almost infinite in number. Despite such complexity, it is possible to individuate some basic molecular chromophores whose modification leads to the formation of many other systems. It is then reasonable to classify chromophores according to their intrinsic molecular structure. For example, all nucleobases that can be regarded as a modified pyrimidine molecule are normally referred as pyrimidine nucleobases. The properties of a class of chromophores can consequently be related to those of the parent

structure. This leads both to the identification of a possible common photophysical and photochemical behavior expected for a certain class of chromophores, and to the study of the effects due to a particular modification, as for example the introduction of a given functional group. Depending on the specific substitution, the photophysical and photochemical properties of a system can significantly change. As an example, the non-canonical nucleobases, obtained by modification of the canonical nucleobases, do not normally share the well-documented photostability of the parent structures [7].

Naphthalene is among such basic molecular chromophores, having a simple structure composed by two-fused benzene rings. The molecule 1-aminonaphthalene can be considered as a modified naphthalene structure in which a hydrogen atom has been substituted by an amino group (see Figure 1.1). The description of its photophysical and photochemical response is a precious tool in order to study more complex systems, to understand the intrinsic properties of naphthalene, and the effects produced by the amino group. In general, substituted aromatic molecules with electron-donating groups have been shown to play an important role in different photochemical and photobiological processes. For example, in the bichromophoric systems employed to analyze electronic energy transfer (EET) and photoinduced electron transfer (PET), substituted aromatic molecules such as aminobenzonitrile act as a donor or acceptor [11-13].

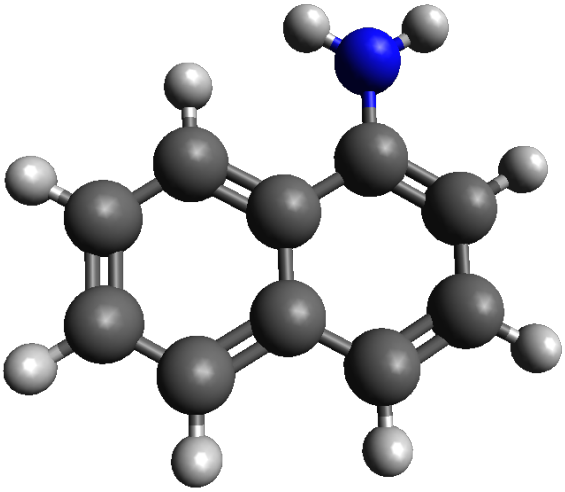

Figure 1.1: 1-aminonaphthalene molecule.

For the mentioned reasons, the study of the photophysical behavior that characterizes 1-aminonaphthalene has been undertaken. The present work is the result of a combined theoretical and experimental research carried out in collaboration with the experimental group of Fernando Castaño at the *Universidad del País Vasco*, where transient ionization signals at femtosecond time resolution have been collected for the entitled molecule. The comparison of the photophysical standpoints obtained on the basis of theoretical calculations and experimental data is certainly instructive.

1.2.1.2 Indole, the main emissive source of proteins

Many different biological functions in most living organisms are performed by proteins. In order to understand their importance, it is just sufficient to recall that most of the enzymes are proteins. They are very

complicate systems normally built by more than one hundred amino acids, bound together through the formation of peptide bonds. The activity and specific function of a protein is dictated by the sequence of the amino acids building blocks and by its three-dimensional structure. These features determine in fact the so-called binding site, which is the region of the protein that normally interacts with a particular substrate. Characteristics of the binding site define then the molecules that the protein can recognize and influence. In order to study the biological role of a protein, it is consequently essential to establish, apart from its amino acid sequence, its three-dimensional structure. One of the most powerful techniques able to achieve such a goal is X-ray diffraction [14]. Its main inconvenient is that it provides information of only crystallized proteins, whose spatial conformation can significantly change with respect to their native form. A different way to get information of the spatial arrangement of a protein, which can be applied directly in biological systems, is by analyzing its fluorescence features. Such strategy is based on the fact that their chromophoric parts are significantly sensitive to microenvironmental conditions. Consequently, it is possible to relate the photophysical properties of a protein with its three-dimensional structure. The case of a protein in an aqueous solution represents an illustrative example. If the conformation determines that the chromophores are directly surrounded by water molecules, then a certain fluorescent radiation is produced. Otherwise, if the chromophores are enclosed in the same protein, a different emission is produced.

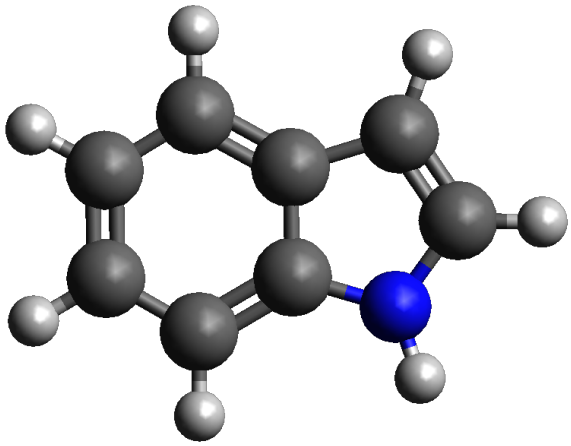

Figure 1.2: Indole molecule.

The amino acids tryptophan, tyrosine, phenylalanine, and histidine can be considered as the main aromatic chromophoric constituents of proteins. [15,16]. Among them, tryptophan is undoubtedly the most important emissive source. The basic chromophore of tryptophan is indole (see Figure 1.2), which is also present in other biologically relevant molecules as the neurotransmitter serotonin (see Figure 1.3). Indole is a π-conjugated heterocyclic organic molecule. It has a bicyclic structure, composed of a benzene ring fused together with a pyrrole ring. In order to provide the necessary information to understand the photoresponse of more complex systems, in the context of the present thesis, the photophysics of the basic aromatic molecule indole has been studied, due also to its intrinsic importance as a natural chromophore.

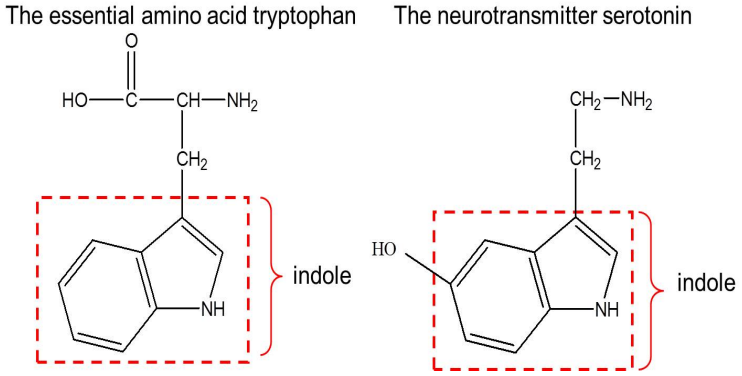

Figure 1.3: Tryptophan and serotonin molecules, in which the indole structure is highlighted.

1.2.2 DNA related chromophores

DNA (deoxyribonucleic acid) is certainly one of the most important molecules for life. It has the fundamental role of keeping, transmitting, and preserving the genetic information of living organisms. It provides the instructions to build the sequences of amino acids that form the needed proteins. Chemically, it is a double-strand helix constituted by two polymers built of repeating units called nucleotides, which in turn contain a nucleobase, a sugar, and a phosphate group. Four different nucleobases named canonical are normally present in DNA: two pyrimidine nucleobases, which are cytosine and thymine; and two purine nucleobases, which are adenine and guanine. Different DNA systems are characterized by different sequences of nucleobases. The specific arrangement of a DNA molecule is the way in which the genetic information is stored. In fact, for each specific sequence of nucleobases, a specific sequence of amino acids is encoded. Consequently, the integrity of DNA in a living organism is undoubtedly a necessary requirement for its correct functionality. The nucleobases involved in DNA are chro-

mophores [5]. The absorbed radiation promotes the population of their excited states, and subsequently they can evolve to the formation of photoproducts, which can seriously compromise the so-important chemical integrity of DNA, that is the preservation of the genetic information. Different protection mechanisms are operating against such deleterious occurrences. Firstly, the four nucleobases that form the genetic material are characterized by a high photostability [7]. The gained energy can in fact be efficiently released in an ultrafast (in the order of the femtosecond) non-radiative process, leading the molecule back to the original equilibrium structure of the ground state. Interestingly, the process is a feature of canonical nucleobases, normally not present in non-canonical nucleobases. Secondly, there are specific photoactivated enzymes able to repair such DNA damages [8,9].

In the performed research we have analyzed two important aspects of the photophysics and photochemistry of DNA: the photoinduced mechanism of production of an important DNA lesion, and the intrinsic photostability of a DNA building block molecule.

1.2.2.1 Thymine-Thymine (6-4) adduct, a DNA photolesion

The most frequent and important DNA photoproducts are caused by reaction of two adjacent pyrimidine nucleobases in the same strand. They can be classified in two main groups: the cyclobutane pyrimidine dimers (Pyr<>Pyr) and the pyrimidine-pyrimidone (6-4) adducts [5,6]. The former are the results of a photocycloaddition between the carbon-carbon double bonds of two pyrimidine molecules, which form a cyclobutane structure. The latter are produced by the reaction of a carbon-carbon double bond and a carbonyl or an amino group belonging to different moieties. Probably due to its higher yield of formation in cellular DNA, the mechanism of production of Pyr<>Pyr dimers has

been extensively studied [17-24], while little is known about the processes that lead to pyrimidine-pyrimidone (6-4) adduct formation. The present thesis compiles the great efforts addressed to unveil the intrinsic mechanisms of the photoinduced formation of such group of photoproducts, considering in particular the thymine-thymine (6-4) adduct (see Figure 1.4).

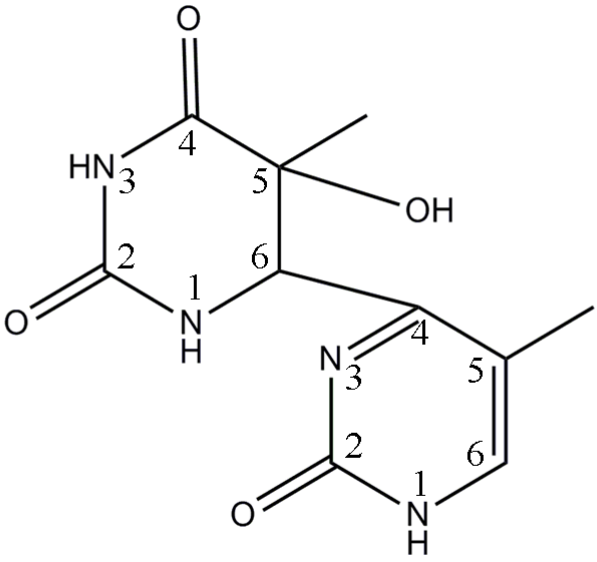

Figure 1.4: Structure and atom labeling of the thymine-thymine (6-4) adduct.

1.2.2.2 Cytosine, a DNA building block chromophore

As previously highlighted, the chromophores normally present in DNA (the canonical pyrimidine and purine nucleobases) have been shown by

different outstanding theoretical and experimental groups to be highly photostable, since their respective bright excited states can efficiently decay back to the original equilibrium geometry of the ground state [7]. The details of the mechanism that allows such important property have been the object of many debates, due to the intrinsic difficulty to describe such phenomenon and the different approaches used to explain it. Along the years, the description of the photophysical behavior of cytosine (see Figure 1.5) has proven to be particularly challenging. In the context of the present thesis, the theoretical works aim to rationalize from a static point of view the photophysics of cytosine up to date have been critically analyzed. Inspired by a suggestion present in a previous paper [25], a CASPT2 minimum energy path (MEP) calculation from the Franck-Condon (FC) region on the bright excited state has been performed.

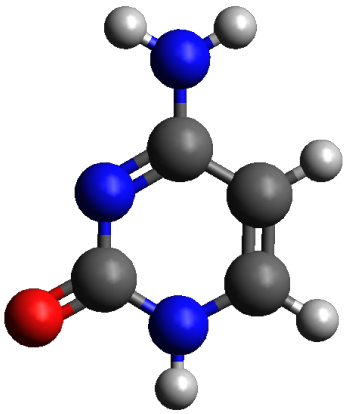

Figure 1.5: Cytosine molecule.

1.2.3 Chromophores introduced by humans

1.2.3.1 Asulam, a widely used pesticide

Chemistry has undoubtedly provided many different tools for human progress, which have changed society and have enormously increased human possibilities. Just to mention a couple of examples, it is sufficient to think about the impact of plastic materials and batteries in normal life. Besides the undeniable advantages that chemical industry has in general introduced, considerable negative consequences have also been created. In fact, the use and/or production of chemical compounds is frequently a source of pollutants which represent a real risk for both humans and ecosystems. For example, exhausted batteries contain dangerous elements as lead, mercury, and cadmium. Catalyzed by such concerns a new branch of chemistry aimed to research substances and processes that minimize the environmental impact appeared: the so-called green chemistry. Among the different fields in which chemistry (and unfortunately chemical pollutants) plays a pivotal role, it is the primary sector of the economy. Indeed, one of the main problems associated with agriculture is related to the use of large quantities of chemical products, such as pesticides, fertilizers, and herbicides. Their presence in the environment may cause serious problems for human health, as well as for the equilibrium of ecosystems [26]. This fact has prompted the study and development of methods for the degradation of such substances, and it has been shown that in many cases this aim can be achieved by photodegradation. A photodegradable pesticide will definitely constitute a highly-desirable chemical agent. Of course, the key requirement is that the by-products of photodegradation will not be toxic, and ideally the photodegradation process should be mediated by solar radiation after a given period of time. In order to evaluate the possibility of obtain-

ing photodegradable pesticides, the understanding of the photophysics and photochemistry of the most used molecules in agriculture constitutes a basic requirement. A commonly employed class of compounds are the so-called carbamate insecticides. Chemically, such molecules are esters derived from the carbamate acid. They are used as pesticides due to the ability of inactivating the enzyme acetylcholinesterase, whose capacity to hydrolyze acetylcholine is of fundamental importance in biological neurotransmission processes. Among carbamate systems, the study of the molecule asulam, methyl((4-aminophenyl)sulfonyl)carbamate or N-(4-aminophenyl)sulfonylcarbamic acid methyl ester (see Figure 1.6) is particularly interesting since it is a common herbicide employed for bracken control [27,28]. In the context of the present thesis, a contribution in this field of research has been provided through the exploration of the photophysics and photochemistry of asulam by means of the CASPT2//CASSCF protocol. Such a work has been performed in collaboration with the experimental group headed by Professor Juan Arturo Santaballa, at the *Universidade da Coruña*.

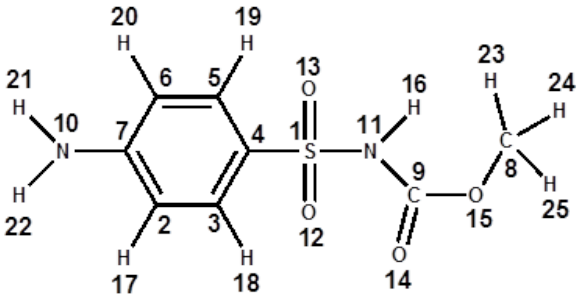

Figure 1.6: Structure and atom numbering of asulam.

1.3 References

[1] Horton, H. R; Moran, L. A; Ochs, R. S; Rawn, J. D; Scrimgeour, K. G. In *Principles of Biochemistry*; Prentice Hall: Upper Saddle River, 1996, pp 435-458.

[2] Mathies, R. A.; Lugtenburg, J. In *Molecular Mechanism of Vision*; Stavenga, D. G.; DeGrip, W. J.; Pugh, E. N. J., Eds.; Elsevier: New York, 2000; Vol. 3, pp 55-90.

[3] Kandori, H.; Shichida, Y.; Yoshizawa, T. *Biochemistry* (Moscow) **2001**, *66*, 1197.

[4] Hurley, J. B.; Ebrey, T. G.; Honig, B.; Ottolenghi, M. *Nature* **1977**, *270*, 540.

[5] Cadet, J.; Vigny, P. In *Bioorganic Photochemistry*; Morrison, H., Ed.; John Wiley & Sons, Inc.: New York, 1990; Vol. 1, pp 1-272.

[6] Sinha, R. P.; Hader, D. P. *Photochem. Photobiol. Sci.* **2002**, *1*, 225.

[7] Serrano-Andrés, L.; Merchán, M. *J. Photochem. Photobiol. C: Photochem. Rev.* **2009**, *10*, 21.

[8] Rupert, C. S.; Goodgal, S. H.; Herriott, R. M. *J. Gen. Physiol.* **1958**, *41*, 451.

[9] Todo, T.; Takemori, H.; Ryo, H.; Ihara, M.; Matsunaga, T.; Nikaido, O.; Sato, K.; Nomura, T. *Nature* **1993**, *361*, 371.

[10] Bonnett, R. *Chemical Aspects of Photodynamic Therapy*; Gordon and Breach Science, Amsterdam, 2000.

[11] Chattoraj, M.; Bal, B.; Closs, G. L.; Levy, D. H. *J. Phys. Chem.* **1991**, *95*, 9666.

[12] Chattoraj, M.; Bal, B.; Shi, Y.; Closs, G. L.; Levy, D. H. *J. Phys. Chem.* **1993**, *97*, 13046.

[13] Syage, J. A.; Felker, P. M.; Zewail, A. H. *J. Chem. Phys.* **1984**, *81*, 2233.

[14] Ashcroft, N. W.; Mermin, N. D. *Solid State Physics*; Sauders College, Philadelphia, USA, 1976.

[15] Wetlaufer, D. B. Ultraviolet spectra of proteins and amino acids. In *Advances in Protein Chemistry*; Anfinsen, C. B., Anson, M. L., Bailey, K., Edsall, J. T., Eds.; Academic Press: New York, 1962; Vol. 17.

[16] Demchenko, A. P. *UltraViolet Spectroscopy of Proteins*; Springer-Verlag: Berlin, 1986.

[17] Roca-Sanjuán, D.; Olaso-González, G.; González-Ramírez, I.; Serrano-Andrés, L.; Merchán, M. *J. Am. Chem. Soc.* **2008**, *130*, 10768.

[18] Serrano-Pérez, J. J.; González-Ramírez, I.; Coto, P. B.; Merchán, M.; Serrano-Andrés, L. *J. Phys. Chem. B* **2008**, *112*, 14096.

[19] Climent, T.; González-Ramírez, I.; González-Luque, R.; Merchán, M.; Serrano-Andrés, L. *J. Phys. Chem. Lett.* **2010**, *1*, 2072.

[20] Manson, F.; Laino, T.; Tavernelli, I.; Rothlisberger, U.; Hutter, J. *J. Am. Chem. Soc.* **2008**, *130*, 3443.

[21] Schreier, W. J.; Schrader, T. E.; Koller, F. O.; Gilch, P.; Crespo-Hernández, C. E.; Swaminathan, V. N.; Carell, T.; Zinth, W.; Kohler, B. *Science* **2007**, *315*, 625.

[22] Mouret, S.; Baudouin, C.; Charveron, M.; Favier, A.; Cadet, J.; Douki, T. *Proc. Natl. Acad. Sci. U.S.A.* **2006**, *103*, 13765.

[23] Kwok, W. M.; Ma, C.; Phillips, D. L. *J. Am. Chem. Soc.* **2008**, *130*, 5131.

[24] Cuquerella, M. C.; Lhiaubet-Vallet, V.; Bosca, F.; Miranda, M. A. *Chem. Sci.* **2011**, *2*, 1219.

[25] Serrano-Andrés, L.; Merchán, M. In *Radiation Induced Molecular Phenomena in Nucleic Acids;* Eds. M. K. Shukla and J. Leszczynski, Springer, The Netherlands, 2008, pp 435-472.

[26] Gevao, B.; Semple, K. T.; Jones, K. C. *Environ. Pollut.* **2000**, *108*, 3.

[27] European Food Safety Authority. Conclusion on the Peer Review of the Pesticide Risk Assessment of the Active Substance Asulam. *EFSA J.* **2010**, *8*, 1822.

[28] Tomašević, A. V.; Gašić, S. M. In *Insecticides: Basic and Other Applications*; Larramendy, S. S. M., Ed.; InTech: Rijeka, Croatia, 2012; pp 39-60.

Chapter 2

Theoretical background

2.1 Fundamental concepts in quantum chemistry

2.1.1 Potential energy hypersurface

The equation that is normally assumed to describe in a good approximation the states of a system formed by electrons and nuclei (as for example an isolated molecule), without considering explicitly its relativistic effects, is the so-called time-independent Schrödinger equation (see equation 2.1) [1]. It constitutes an eigenvalue-eigenfunction problem for the Hamiltonian operator $\hat{H}(r,R)$ (see equation 2.2), where each of its eigenfunction $\Psi_n(r,R)$ represents a wave function of a particular state of the system, whose energy is given by the corresponding eigenvalue $E_n(r,R)$.

$$\hat{H}(r,R)\Psi_n(r,R) = E_n(r,R)\Psi_n(r,R) \tag{2.1}$$

$$\hat{H}(r,R) = \hat{T}_{Nu} + \hat{T}_{el} + \hat{V}_{Nu-el} + \hat{V}_{el-el} + \hat{V}_{Nu-Nu} \tag{2.2}$$

where $\hat{T}_{Nu}$ represents the kinetic operator for the nuclei; $\hat{T}_{el}$ corresponds to the kinetic operator for the electrons; $\hat{V}_{Nu-el}$ stands for the operator for the Coulomb attraction between electrons and nuclei; $\hat{V}_{el-el}$ is the operator for the Coulomb repulsion between electrons; $\hat{V}_{Nu-Nu}$ accounts for the operator of the Coulomb repulsion between nuclei. In the preceding and following equation r and R represent the coordinates of the electrons and nuclei, respectively.

It is worth reminding that this equation could be obtained from the more general time-dependent Schrödinger equation in the case that the potential energy felt by the system does not depend on time, and when only the so-called stationary states are considered (which are particular solutions product of a function depending on time and a function depending on the spatial coordinates) [1].

Except for hydrogen-like atoms, the time-independent Schrödinger equation cannot be solved exactly since the Hamiltonian operator is not separable in terms that depend on a single variable. A commonly used assumption in order to simplify the problem is the Born-Oppenheimer approximation (BOA) [1-4], which is based on the fact that nuclei are much heavier than electrons and therefore they move more slowly. Justified by such physical fact, it is reasonable to consider that the electronic distribution instantaneously adapt itself according to any movement of the nuclei. Then it is possible to regard a molecule as a system composed of objects (the nuclei) immersed in an external potential field (created by the electrons and by the nuclear repulsion energy) that vary according to the their coordinates. Mathematically the BOA leads to a separation of the time-independent Schrödinger equation in two related eigenvalue-eigenfunction problems. The first equation describes the motion of the electrons in the field of the nuclei considered fixed at some positions, and it is normally referred as the electronic problem or

the electronic Schrödinger equation (see equation 2.3) [1,2]. The second equation describes the motion of the nuclei in the average field of the electrons, obtained by the resolution of the electronic problem. The electronic Schrödinger equation is an eigenvalue-eigenfunction problem for the so-called electronic Hamiltonian operator $\hat{H}^{el}(r;R)$ (see equation 2.4) that describes the original system in which the nuclei are considered fixed at some positions. The electronic Hamiltonian depends on the nuclear coordinates through the term accounting for the Coulomb attraction between electrons and nuclei, making the solutions dependent parametrically on the chosen fixed nuclear configuration.

$$\hat{H}^{el}(r;R)\psi_i(r;R) = E_i^{el}(r)\psi_i(r;R) \tag{2.3}$$

$$\hat{H}^{el}(r;R) = \hat{T}_{el} + \hat{V}_{Nu-el} + \hat{V}_{el-el} \tag{2.4}$$

Actually, the operator $\hat{V}_{Nu-Nu}$ appears also in the Hamiltonian describing a system composed of moving electrons in the presence of fixed nuclei. Since in such a case the repulsion between the nuclei is constant, and because any constant added to an operator only adds to the operator eigenvalues and has no effect on the operator eigenfunctions, the $\hat{V}_{Nu-Nu}$ term does not appear in the definition of the electronic Hamiltonian.

The electronic problem has several solutions, each of which represents an electronic state with a particular electronic energy given by the corresponding eigenvalue. In the framework of the BOA the electronic energy can be regarded as the value of the potential field that the electrons apply to the nuclei for the molecule in that particular geometry and electronic state.

The BOA can formally be derived writing the time-independent

Schrödinger wave function in the complete basis set of the solutions of the electronic problem. It is important to notice that no approximations have been introduced in this first step.

$$\Psi_n(r,R) = \sum_i \varphi_n^i(R)\psi_i(r;R) \tag{2.5}$$

Inserting the previous expression into the time-independent Schrödinger equation (equation 2.1), and multiplying to the left by $\psi_i(r;R)$, it is possible to obtain:

$$E_n\varphi_n^i = [\hat{T}_{Nu} + V_i]\varphi_n^i + \sum_j \hat{\Lambda}_{ij}\varphi_n^j \tag{2.6}$$

Where $V_i = E_i^{el} + V_{Nu-Nu}$ is the electronic energy plus the nuclear repulsion energy, and $\hat{\Lambda}_{ij}$ are the non-adiabatic coupling terms, equal to:

$$\hat{\Lambda}_{ij} = -\frac{\hbar^2}{2} < \psi_i|\triangle_R|\psi_j > -\hbar^2 < \psi_i|\nabla_R|\psi_j > \nabla_R \tag{2.7}$$

The main contribution to $\hat{\Lambda}_{ij}$ is given by the last term of the preceding expression (the so-called derivative coupling) which can be expressed making use of the Hellmann-Feynman theorem [1] as:

$$< \psi_i|\nabla_R|\psi_j >= \frac{< \psi_i|\nabla_R\hat{H}^{el}\psi_j >}{E_j^{el} - E_i^{el}} \tag{2.8}$$

The BOA consists in considering negligible the non-adiabatic coupling terms $\hat{\Lambda}_{ij}$. The assumption is in agreement with the above presented physical interpretation and motivation of the BOA, since the non-adiabatic coupling terms account for the variation in the electronic wave function due to nuclear displacements. In such a way, the time-independent

Schrödinger equation is reduced to:

$$[\hat{T}_{Nu} + V_i]\varphi_n^i = E_n\varphi_n^i \tag{2.9}$$

Where V_i is given by the eigenvalue of the corresponding electronic problem plus the nuclear repulsion term. Consequently, as anticipated above, the time-independent Schrödinger equation is divided in two related eigenvalue-eigenvector problems: the electronic problem and equation 2.9, called nuclear Schrödinger equation [1-2]. The solution of the time-independent Schrödinger equation in the framework of the BOA is then equal to a product of an electronic wave function and a nuclear wave function:

$$\Psi_n(r, R) \approx \varphi_n^i(R)\psi_i(r; R) \tag{2.10}$$

In that way a system can be considered in a certain electronic state (characterized by the electronic wave function $\psi_i(r; R)$ and the corresponding electronic energy $E_i^{el}(r; R)$), and in a particular nuclear state (having the nuclear wave function equal to $\varphi_n^i(R)$ and nuclear energy E_n). The nuclear Schrödinger equation and consequently both the nuclear wave function and energy can be further divided in three contributions associated with the vibrational, rotational, and translational nuclear states of the system, here named in decreasing energy ordering. It is important to notice that the nuclear states (and consequently the possible vibrational, rotational, and translational states) depend on the particular electronic state in which the system is considered, since the electronic energy is part of the nuclear Hamiltonian (see Figure 2.1).

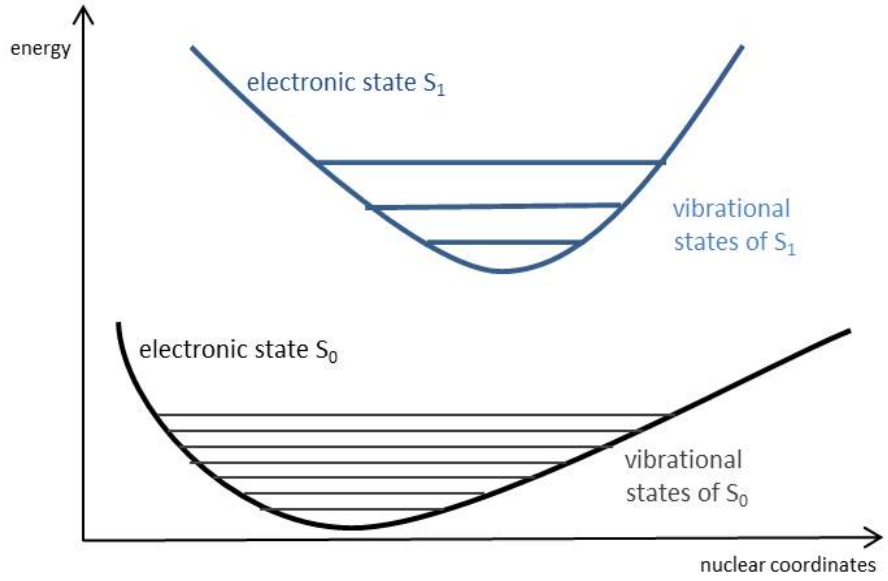

Figure 2.1: Potential energy hypersurface for two electronic states in which the respective vibrational states have also been represented.

As stated above, in the BOA a molecular system can be regarded as a collection of particles (the nuclei) subject to a potential field. Since the behavior of a system immersed in an external potential field is strongly affected by the characteristics of the latter, most of the efforts for describing a molecule within the BOA are devoted to the determination of such external field, and in particular to the part of it caused by the electrons. The determination of the potential field apply by the electrons to the nuclei is accomplished by the resolution of the electronic problem for each of the possible nuclear configurations that the system can adopt. Addition of the nuclear repulsion energy to the electronic energy of a particular electronic state constitutes the potential energy

for the system in that particular state. The collection of all the values of the potential energy as a function of the nuclear coordinates corresponds to the potential energy hypersurface (PEH) of that state [1-3]. A PEH consequently represents the potential field that the nuclei feel for the system in a given electronic state at their respective coordinates. Then the nuclear coordinates of a system (its geometry) will evolve according to such potential field, and will normally tend to a stable conformation (i.e. a minimum of the corresponding PEH). For the same system, different electronic states are characterized by different PEHs.

The concept of PEH is one of the basic tools in order to explain and predict chemistry, since according to the exposed model the stability of a geometry and the possible deformations that a molecule may undergoes through are determined in good approximation by the topography features of the corresponding PEHs. In a thermal reaction, the energy required for a molecular system in a stable conformation of its lowest-energy electronic state (the ground state) to evolve to a different minimum structure, is determined by the lowest energy barrier that separate such points in the corresponding PEH. In the case of photoinduced processes involving more than one electronic state, the chemical process will be determined by the features of all the corresponding PEHs, and in particular by the relation among them.

2.1.2 Interaction of radiation and matter

Different approaches can be employed in order to describe the interaction of matter with light. The one used in the present thesis, which will be briefly introduced in the followings lines, is referred as semiclassical treatment [1]. The name reflects the fact that the molecular system is considered quantum-mechanically while the radiation is described as a

classic electromagnetic wave of oscillating electric and magnetic fields. A further approximation that is also adopted here is to consider only the interaction created by the radiation electric field, which is normally much bigger that the interaction caused by the radiation magnetic field.

A molecule exposed to radiation for a certain period of time constitutes a system subject to an external potential field that depends on time. The description of such a situation is given by the solutions of the corresponding time-dependent Schrödinger equation, which can be obtained using time-dependent perturbation theory [1]. The total Hamiltonian of the system can in fact be regarded as the sum of a main term describing the isolated molecule, plus a small perturbation representing the electric potential field produced by the radiation. According to time-dependent perturbation theory, a system in a single stationary state $e^{(-iE_n t/\hbar)}\Psi_n(R,r)$ will be described after the application of a small and short time-dependent perturbation by the following wave function, that is a superposition of the initial stationary states:

$$\Phi(t,R,r) = \sum_m b_m(t) e^{(-iE_m t/\hbar)} \Psi_m(R,r) \tag{2.11}$$

The coefficients b_m of such an expansion, whose absolute square value gives the probability to find the system in the corresponding state, are equal to:

$$b_m(t) = \delta_{mn} - \frac{i}{\hbar}\int_0^t e^{[i(E_m - E_n)t/\hbar]} < \Psi_m|\hat{H}'|\Psi_n > dt \tag{2.12}$$

where $\hat{H}'$ is the perturbation. For the study situation $\hat{H}'$ is given by the radiation electric field, which in the case of a plane-polarized electromagnetic wave traveling in the z direction is equal to:

$$\hat{H}' = -\varepsilon_0 \sum_i Q_i x_i sin(2\pi\nu t - 2\pi z_i/\lambda) \tag{2.13}$$

where Q_i indicates the charges of the system, while ν and λ are the frequency and the wavelength of the electromagnetic wave, respectively. Using the last expression in equation 2.12, and neglecting the term $2\pi z_i/\lambda$ due to its little contribution to the integral $< \Psi_m|\hat{H}'|\Psi_n >$, it is possible to obtain:

$$\begin{gathered} b_m(t) = \delta_{mn} + \\ \frac{\varepsilon_0}{2\hbar i} < \Psi_m| \sum_i Q_i x_i |\Psi_n > \left[\frac{e^{i(\omega_{mn}+\omega)t}-1}{\omega_{mn}+\omega} - \frac{e^{i(\omega_{mn}-\omega)t}-1}{\omega_{mn}-\omega} \right] \end{gathered} \tag{2.14}$$

where the following definitions have been used:

$$\begin{gathered} \omega_{mn} = (E_m - E_n)/\hbar \\ \omega = 2\pi\nu \end{gathered} \tag{2.15}$$

Expression 2.14 consequently gives the coefficients characterizing the superposition of states that represent the wave function of a molecular system initially described by the stationary state $e^{(-iE_n t/\hbar)}\Psi_n(R,r)$ after a short interaction with the electric field generated by a radiation having ν frequency. In the case that one of the following equations is satisfied:

$$\omega_{mn} = \omega \tag{2.16}$$

$$\omega_{mn} = -\omega \tag{2.17}$$

the corresponding b_m coefficient will be particularly large, and conse-

quently the system will be mainly described by the $e^{(-iE_m t/\hbar)}\Psi_m(R,r)$ state. Using the expressions 2.15 is easy to verify that equation 2.16 and 2.17 are satisfied in the case in which $(E_m - E_n) = h\nu$ and $(E_n - E_m) = h\nu$, respectively. In both situations the exposure to a radiation having ν frequency will cause the transition from the state Ψ_n to the state Ψ_m, but since ν is always positive, in the first case $E_m > E_n$, while in the second case $E_n > E_m$. Such phenomena are normally called absorption and stimulated emission, respectively [1].

According to expression 2.14, the b_m coefficient are also proportional to $< \Psi_m | \sum_i Q_i x_i | \Psi_n >$. The latter is called the transition dipole moment (TDM) [1,5], and its presence in equation 2.14 impose that a transition between the n and the m states will be allowed only if the corresponding transition dipole moment is not equal to zero. For example, a transition between states having different spin multiplicity will not be allowed according to the presented theoretical treatment.

The energy gap associated to the transition from the n to the m state can be divided in electronic and nuclear components since, if the BOA is valid, each time-independent wave function can be decomposed in the product of an electronic and a nuclear wave function. The interaction of a compound with a radiation having a frequency equal to the energy gap between two electronic states whose corresponding TDM is not equal to zero will cause the transfer of population from the initial to the final state. In the present thesis we will study the interaction of different molecular systems with radiations able to promote electronic transfers, which are of particular interest since they can cause fluorescence and phosphorescence emission and they can catalyze photochemical reactions. Such radiations are normally taking place in the UV-vis region of the spectrum. Depending on the precise energy of the radiation, the absorption process populates an excited electronic state in an excited

nuclear state, as for example an excited vibrational state.

In general, the probability that the interaction of a molecular system with radiation causes a transition from the n to the m state can be estimated by computing the so-called oscillator strength f [5]:

$$f = \frac{2}{3}(E_m - E_n)TDM^2 \tag{2.18}$$

where the energies and the transition dipole moment are expressed in atomic units. The presence of the square of the transition dipole moment in the definition of the oscillator strength is intimately related with the equation for the coefficients b_m (see equation 2.14), in which TDM appears. The oscillator strength is actually a classically derived magnitude that can be related to the relative area of the electronic transition band and that it can be compared with the experimental outcomes based on shapes and band-widths.

2.1.3 Conical intersection and singlet-triplet intersystem crossing region

In a photoinduced process normally more than one electronic state of the system are involved in the global mechanism. As shown in the preceding subsection, the interaction of radiation and matter can in fact promote the system into an excited state, from which the possible ways of deactivation of the absorbed energy determine the photoinduced events. One of the possible relaxation mechanisms that can be operative is the so-called internal conversion process (IC) [3,5], which is the radiationless transfer of the population of an electronic state to a different electronic state having the same spin multiplicity. The mechanism is mediated by an appropriate coupling of the two involved states, which in turn is normally caused by a small or zero energy difference between the cor-

responding electronic energies. A region where two electronic states get close in energy without crossing is called an avoided crossing, while a region characterized by a real crossing is named conical intersection (CI) [3,5-8]. Both situations may be involved in actual internal conversion processes, although CIs are able to promote much more efficiently an ultrafast population transfer, a property that can be regarded as the most important feature in the determination of a photoinduced event.

In order to understand the capacity of CIs to efficiently mediate internal conversion processes, it is instructive to analyze the main assumption introduced with the BOA. As explained in subsection 2.1.1, through the BOA the time-independent wave function of a system is expressed as the product of an electronic wave function and a nuclear wave function. This has been possible by neglecting the non-adiabatic coupling terms. When such approximation is valid, it is plausible to see the system as in a particular electronic state. On the contrary, in the situation in which the ignored terms are considerably large, the system cannot be regarded any more in a single electronic state, but must be considered in all the electronic states that give significant non-adiabatic coupling elements. In a CI the derivative coupling term between the two crossing states tends to infinity and is consequently not negligible. In fact, as shown in equation 2.8, the derivative coupling is inversely proportional to the energy gap of the involved states. A CI is then a region of the PEH in which the BOA is not valid. Consequently, the system in a CI cannot be regarded in a single electronic state, being equally described by the corresponding relevant electronic functions. For the mentioned reasons, in a CI an internal conversion process is efficiently promoted.

An important point that must be established is the actual presence of CIs in polyatomic systems, which can be addressed by analyzing the

conditions that must be fulfilled in a CI region [6]. Considering a basis set $\{\xi_1, \xi_2\}$ that spans the space of two electronic wave functions ψ_1 and ψ_2, it is possible to write the latter in the form:

$$\psi_i = c_1^i \xi_1 + c_2^i \xi_2 \quad i = 1, 2 \tag{2.19}$$

The corresponding electronic energies can be derived by the secular equation:

$$\begin{bmatrix} H_{11} - E & H_{12} \\ H_{21} & H_{22} - E \end{bmatrix} \begin{bmatrix} c_1 \\ c_2 \end{bmatrix} = 0 \tag{2.20}$$

where H_{11}, H_{22}, H_{21}, and H_{12} are the elements of the matrix representation of the electronic Hamiltonian in the $\{\xi_1, \xi_2\}$ basis set. The electronic energies are given by the following expression, in which the equality between H_{12} and H_{21} has been considered:

$$E_i = \frac{1}{2}\left[(H_{11} + H_{22}) \pm \sqrt{(H_{11} - H_{22})^2 + 4H_{12}^2}\right] \quad i = 1, 2 \tag{2.21}$$

Then the two electronic energies will be degenerate if the following two independent conditions are satisfied:

$$\begin{cases} H_{11} = H_{22} \\ H_{12} = 0 \end{cases} \tag{2.22}$$

In a system described by $3N - 6$ independent variables nuclear coordinates, where N is the number of atoms, the solution of the above described system of two equations will fix the value of two independent nuclear coordinates. This definitely proves the existence of CI in polyatomic systems, which are characterized by more that two independent

nuclear coordinates. The first equation of expression 2.22 determines one coordinate, denoted by the symbol R_1, the second equation fixes a second coordinate, referred as R_2. The space spanned by such coordinates and its orthogonal complement space are called the branching space and the seam or intersection space, respectively [3,5-8]. The names reflect the fact that from the geometry of a CI in which the values of R_1 and R_2 are determined by the fulfillment of expression 2.22, a displacement in the intersection space will not affect the crossing between the two electronic states, while a displacement in the branching space will lift the degeneracy. For that reason, a CI in a system with more than three degrees of freedom can be regarded as a $(3N-8)$-dimensional hyperline in the $3N-6$ nuclear space.

In order to further study such important regions, it is useful to describe the topography at and near a CI [6]. Expanding up to first order at a CI point (linear approximation) the elements of the electronic Hamiltonian matrix that appears in equation 2.21, the following expressions are derived:

$$\begin{aligned} H_{11} &= W + \nabla_R H_{11} \cdot R1 \\ H_{22} &= W + \nabla_R H_{22} \cdot R_1 \\ H_{12} &= \nabla_R H_{12} \cdot R_2 \end{aligned} \tag{2.23}$$

where W is the common value of both H_{11} and H_{22} at the CI. Substituting these equalities in the previously obtained equation for the electronic energies (equation 2.21), the next expressions are obtained:

$$E_i = \tfrac{1}{2}\left[(2W + \nabla_R(H_{11} + H_{22}) \cdot R_1)\right.$$
$$\left. \pm\sqrt{(\nabla_R(H_{11} - H_{22}) \cdot R_1)^2 + 4\,(\nabla_R H_{12} \cdot R_2)^2}\right] \qquad (2.24)$$
$$i = 1, 2$$

$$E_i = W + s_{12} \cdot R_1 \pm \sqrt{(g_{12} \cdot R_1)^2 + (h_{12} \cdot R_2)^2} \;\; i = 1, 2 \qquad (2.25)$$

in which the following definitions have been used:

$$h_{12} = \nabla_R H_{12} \qquad (2.26)$$

$$g_{12} = \frac{h_{11} - h_{22}}{2} \qquad (2.27)$$

$$s_{12} = \frac{h_{11} + h_{22}}{2} \qquad (2.28)$$

The equality 2.25 is mathematically an equation of an elliptic double cone. In fact, if the energies of the two states are plotted against the R_1 and R_2 coordinates, a characteristic double-cone shape will appear (see Figure 2.2). From the above analysis, it seems convenient to describe the space spanned by R_1 and R_2 through the so-called intersection adapted coordinates x_1 and x_2, defined as follows:

$$x_1 = \frac{g_{12}}{\|g_{12}\|} \qquad (2.29)$$

$$x_2 = \frac{h_{12}}{\|h_{12}\|} \qquad (2.30)$$

which are called the gradient difference vector and the non-adiabatic coupling vector, respectively [3,5-8].

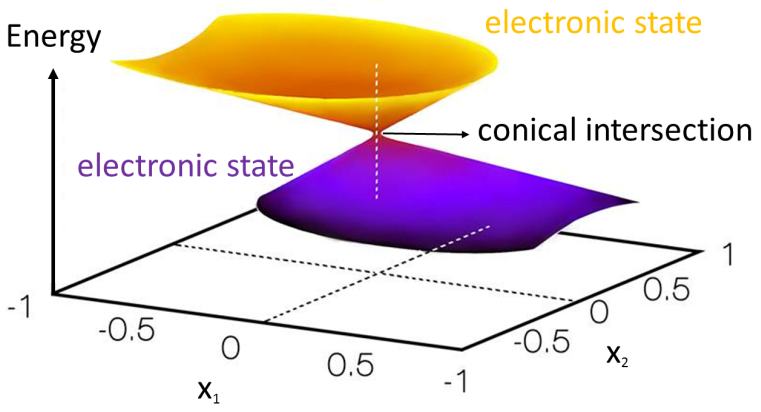

Figure 2.2: PEHs of two electronic states at and near a CI between them, represented in the branching space spanned by the gradient difference and the non-adiabatic coupling vectors.

The values of $\|g_{12}\|$, $\|h_{12}\|$, and s_{12} describe the topography near a CI according to the presented linear approximation. In particular, the parameters $\|g_{12}\|$ and $\|h_{12}\|$ specify the slope of the cone in the two directions x_1 and x_2, while the projections of s_{12} along x_1 and x_2 determine the tilt of the cone and in particular if a CI is sloped or peaked [5-8]. In a sloped CI both PEHs present a downhill slopes and touch each other at the crossing points, while in a peaked CI both PEHs are elliptical cones pointing against each other with a common tip (see Figure 2.3). The sloped or peaked nature of a CI has been proven to

influence the probability that the population of the original state pass to the second state [8,9].

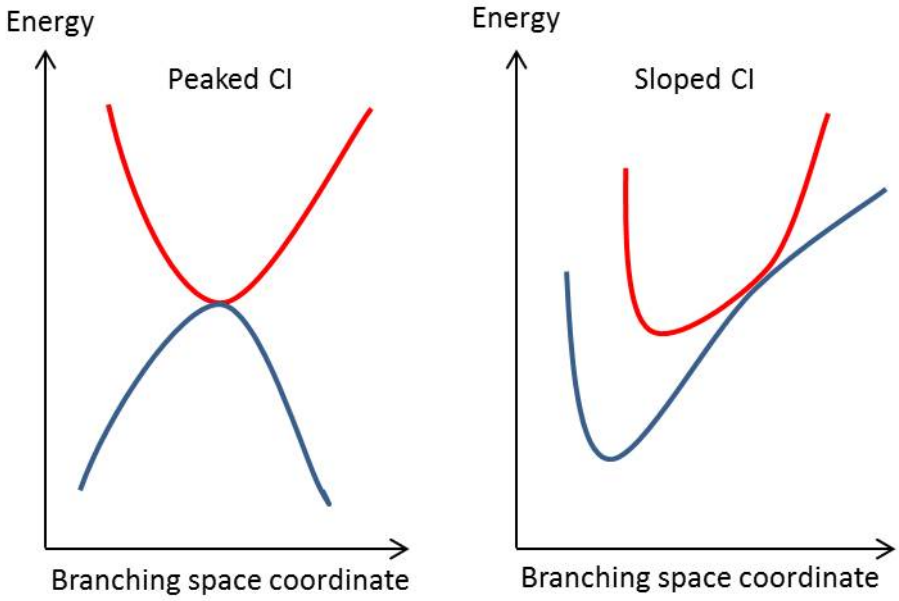

Figure 2.3: PEHs of two electronic states at and near a peaked CI and at and near a sloped CI.

A similar situation as the one described in CIs occurs when the crossing states have different spin multiplicity, as for example in a singlet-triplet crossing region (STC), where a singlet and a triplet state are degenerate in energy [3,5-8]. At such points, the same conditions previously determined for CIs must be fulfilled (see expression 2.22), which are reduced to one since the non-adiabatic coupling term, H_{12}, is always zero due to the different spin multiplicity. For that reason, only

one nuclear coordinate is specified in order to fulfill the requirement, and a STC region constitutes a $(3N-7)$-dimensional hyperplane in the $3N-6$ nuclear space. The degeneracy is preserved along all the coordinates but the corresponding gradient difference vector.

Consideration of only the kinetic and electrostatic terms in the Hamiltonian of the system leads to solutions of the time-independent Schrödinger equation characterized by specific spin symmetry. Consequently, a singlet wave function can be written in the basis of all the solutions of the electronic problem with singlet spin symmetry. According to that, the population of a state will not pass to a state having a different spin multiplicity. Such transfers are nevertheless possible due to relativistic effects, and in particular to the interaction of the electron spin magnetic moment with the magnetic moment due to the orbital motion of electrons [3,10]. The term accounting for such phenomenon, called spin-orbit operator ($\hat{H}_{SO}$), determines the mixing of states having different spin multiplicity, and consequently causes that the solutions of the time-independent wave function must be written in a basis of functions with different spin multiplicity. The importance of such interaction between two states is determined by the corresponding spin-orbit coupling (SOC), which in the case of a singlet S_k state and a triplet T_l state can be expressed as follows [3,5,11]:

$$SOC_{lk} = \sqrt{\sum_{u} \left| < T_{l,u} | \hat{H}_{SO} | S_k > \right|^2} \quad u = x, y, z \tag{2.31}$$

As in the BOA, in which neglecting the non-adiabatic coupling terms allows to write the solution of the time-independent Schrödinger equation as a single electronic wave function, neglecting the SOCs here allows to write the solution of the time-independent Schrödinger equation in term of functions having the same spin symmetry. These are normally

good approximations, but not in certain particular regions of the PEHs. As shown above, at a CI region the BOA fails and the system must be described by the crossing electronic states. Similarly, in a STC region characterized by a high value of SOC between the crossing states, it can be shown that the system must be described by the involved electronic states. Such a situation determines the transfer of population between states having different spin multiplicity, a phenomenon called intersystem crossing process [3,5].

2.2 Fundamental concepts in photophysics and photochemistry

2.2.1 Definition of photophysics and photochemistry

Photophysics and photochemistry belong to the field of science concerning the interaction of radiation with matter [5,6,12,13]. These areas of research study the absorption of energy as radiation and the processes induced by it, which consequently means all the mechanisms that a system may experiment in order to dissipate the gained energy. The difference between the two disciplines is that photophysics studies the processes that started and ended at the same geometry and state (the so-called Franck-Condon, FC, geometry), while photochemistry deals with those events that lead to a chemical change [5].

Adopting the given general definitions of photophysics and photochemistry, any photoinduced event caused by the absorption of radiation will be a possible subject of these disciplines. Despite that, photophysics and photochemistry are normally considered to describe photoinduced processes determined by UV-vis light, although the interaction with infrared radiation can also be considered part of them. Consequently, the

states that play the most important role in these studies are basically electronic states, since the energies involved in UV and visible radiation are between 3.10-12.4 eV and 1.70-3.10 eV, respectively [14].

Four physical phenomena are mainly induced when a molecular system absorbs UV-vis radiation:

- Fluorescence emission (F): spontaneous emission of radiation from an electronic excited state that has the same spin multiplicity that the receiving state (normally the ground state).

- Phosphorescence emission (P): spontaneous emission of radiation from an electronic excited state that has a different spin multiplicity that the receiving state (normally the ground state).

- Internal conversion process (IC): passage of part of the population from one to another electronic state that has the same spin multiplicity, without any loss of energy by radiation.

- Intersystem crossing process (ISC): passage of part of the population from one to another electronic state that has a different spin multiplicity, without any loss of energy by radiation.

The theoretical background needed in order to describe absorption, internal conversion, and intersystem crossing processes have been provided in the preceding section, while in order to explain spontaneous fluorescence and phosphorescence emission the machinery of quantum electrodynamics is required. In the present semiclassical treatment of the interaction of matter and light (see subsection 2.1.2) spontaneous emission is considered to take place in the region in which no other mechanisms of relaxation are possible, as for example in a well-defined minimum of the lowest singlet excited state.

According to the above definitions the very same physical phenomenon, as for example the absorption and subsequently emission of radiation from a populated excited state, can be classified as a photophysical or a photochemical process, depending only on the initial and final geometry. As pointed out above, and as explained in detail in the following section, the PEH represents one of the most useful concepts to study both photophysics and photochemistry. The definition of photophysics and photochemistry together with the described photoinduced phenomena are presented in Figure 2.4.

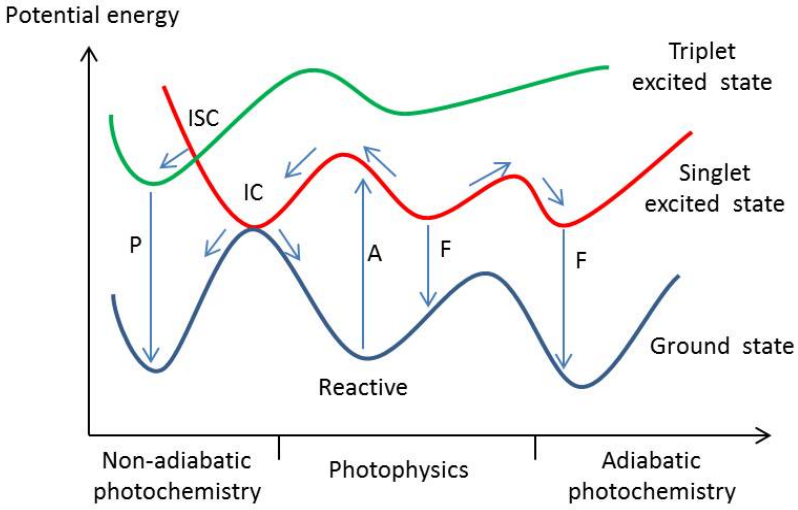

Figure 2.4: Main photophysical and photochemical processes: absorption (A), fluorescence emission (F), phosphorescence emission (P), internal conversion process (IC), and intersystem crossing process (ICS).

2.2.2 Photochemical reaction path approach

The following lines briefly explain the strategy that has been adopted in the present thesis in order to describe photoinduced processes. Such a way of working is based on the concept of PEH (and consequently on the BOA), the semiclassical treatment of the interaction of matter and light, and the next defined photochemical reaction path approach [5,6,13,15].

The system is initially considered in a minimum geometry of its ground state. The interaction with radiation can cause transfer of population to one or more excited states whose vertical transitions have the largest values of oscillator strength. The so-populated excited states are normally in a non-equilibrium geometry of their respective PEHs, and consequently will evolve to a more stable situation. Such energy relaxation determines the global photoinduced process. The photochemical reaction path approach considers that the most probable way in which the system will evolve from the FC region depends on the local properties of the PEH such as slopes, barriers, saddle points, etc. According to such strategy, the system from a non-equilibrium structure will primarily evolve along the direction of the gradient and any particular region of the PEH will be considered relevant only if it is energetically accessible to the system. The main decay path experimented by a non-equilibrium geometry is then obtained by the computation of the corresponding minimum energy path (MEP), which can be defined as the path from a non-equilibrium geometry and state to the first present minimum region encountered following the direction of the gradient recalculated in each new step [5,6,13,16,17]. The MEP can be regarded as the trajectory followed by a classical particle sliding with infinitesimal velocity and no excess energy under the influence of the potential field

described by the PEH. A region of the PEH can be considered energetically accessible from a starting geometry if there is a connected path between the involved structures characterized by an energy barrier to be surmounted not higher than the average energy associated with vibrational excitation. Using such an approach, the relevance to a particular photoinduced process of a minimum, a transition state, a CI, and any other region of the PEHs is deduced not only by its intrinsic characteristics, but mostly by the ability of the system to actually populate such a geometry. For example, a low-lying CI between the bright and the ground states could play a minor role in the main photoresponse of the system if such a degenerate region cannot be reached.

The study of the evolution of a given non-equilibrium geometry and state is not a simple task, but it can be satisfactorily accomplished performing the corresponding MEP calculation. An even more difficult goal is the study of the connection between two particular structures. It may happen that the bright state decays to a weakly bonded minimum, and it would be interesting to map the connection between such geometry and an optimized CI with the ground state. It would be important, in particular, to know whether an energy barrier is present between such points, as well as its magnitude. Unfortunately, for such a situation there is not a computational technique that unambiguously provides the sought answer. This condition makes the determination of photoinduced reactions much more difficult that the description of thermally activated processes. The latter can be described in the framework of transition state theory and the most probable connected path along the ground state PEH is unambiguously drawn by the computation of an intrinsic reaction coordinate (IRC) calculation from the saddle point connecting the reactive and the product [18]. Since a relevant CI could geometrically be any kind of point of the PEH, the determination of

the path connecting a minimum structure and a CI cannot be obtain in a general way, but must be analyzed for each particular case. A reasonable approximation able to provide a connected path between two points of a PEH is the computation of a linear interpolation of internal coordinate calculation. A so-obtained path does not take into account the topography of the PEH, as for example the direction of the gradient, but the absence of any energy barrier along it ensures the existence of a barrierless path connecting the involved structures.

It is important to note that the information given by the MEP undertaken by a system is structural, and provides insight into the photoresponse from vibrational cold excited states such as those encountered in experiments in which slow excited state motion and/or thermal equilibration is possible (in cold jets, in cold matrices, and in solution). In the case of a "hot" system (having high excess of vibrational energy), the deactivation may significantly deviate from the MEP, and a dynamics treatment of the problem would be required.

2.3 References

[1] Levine, I. N. *Quantum Chemistry*; Prentice-Hall: New Jersey, USA, 2000.

[2] Levine, I. N. *Molecular Spectroscopy*; John Wiley & Sons: New York, USA, 1975.

[3] Domcke, W.; Yarkony, D. R.; Köppel, H. *Conical Intersections*; World Scientific Publishing Co. Pte. Ltd.: Singapore, Japan, 2004.

[4] Szabo, A.; Ostlund, N. S. *Modern Quantum Chemistry*; Dover Publications: Mineola, New York, USA, 1996.

[5] Serrano-Andrés, L.; Serrano-Pérez, J. In *Handbook of Computational Chemistry*; Leszczynski J (ed), Springer Netherlands 2012, pp 483-560.

[6] Robb, M. A.; Garavelli, M.; Olivucci, M.; Bernardi, F. In *Reviews in Computational Chemistry*; Lipkowitz K. B. and Boyd, D. B. Eds., Wiley-VCH, New York, 2000, Vol 15, pp 87-212.

[7] Yarkony, D. R. *Chem. Rev.* **2012**, *112*, 481.

[8] Matsika, S.; Krause, P. *Annu. Rev. Phys. Chem.* **2011**, *62*, 621.

[9] Paterson, M. J.; Robb, M. A.; Blancafort, L.; DeBellis, A. D. *J. Phys. Chem. A* **2005**, *109*, 7527.

[10] Marian, C. M. *WIREs Comput. Mol. Sci.* **2012**, *2*, 187.

[11] Merchán, M.; Serrano-Andrés, L.; Robb, M.A.; Blancafort, L. *J. Am. Chem. Soc.* **2005**, *127*, 1820.

[12] Klessinger, M.; Michl, J. *Excited States and Photochemistry of Organic Molecules*; VCH Publishers: New York, USA, 1995.

[13] Merchán, M.; Serrano-Andrés, L. In *Computational Photochemistry, 1st ed.*; Olivucci, M., Ed.; Elsevier: Amsterdam, The Netherlands, 2005; Vol. 16, pp 35-91.

[14] Braslavsky, S. E. *Pure Appl. Chem.*, 2007 Vol. 79, No. 3, pp. 293–465.

[15] Fuß, W.; Lochbrunner, S.; Müller, A.M.; Schikarski, T.; Schmid, W.E.; Trushin, S.A. *Chem. Phys.* **1998**, *232*, 161.

[16] Truhlar, D.G.; Steckler, R.; Gordon, M.S. *Chem. Rev.* **1987**, *87*, 217.

[17] De Vico, L.; Olivucci, M.; Lindh, R. *J. Chem. Theory Comput.* **2005**, *1*, 1029.

[18] McKee, M. L.; Page, M. in *Reviews in Computational Chemistry*; Lipkowitz K. B. and Boyd, D. B. Eds., VCH Publishers, New York, 1993, Vol. 4, pp. 35-65.

Chapter 3

Theoretical methods: problems to be solved

In the present thesis we have mainly dealt with two problems: the so-called electronic problem for different configurations of the nuclei and the exploration of the potential energy hypersurfaces (PEHs) of different electronic states of the systems. The electronic problem is the resolution of the eigenfunctions-eigenvalues equation (see equation 2.1), which results from the application of the Born-Oppenheimer approximation to the time-independent Schrödinger equation, without considering any relativistic effects [1,2]. Its eigenvalues are the electronic energies of the different states of the system, which are characterized by the corresponding eigenfunctions.

The result of the addition of the nuclear repulsion energy to the electronic energy of a state constitutes the magnitude of the potential energy for the system in that particular state and geometry. The collection of all the values of the potential energy of a state as a function of the nuclear coordinates builds the PEH of that state. Determination of crit-

ical points of a PEH (such minima, saddle points, conical intersections (CIs), etc), makes possible to correlate different PEHs of the system. In general, it allows the characterization of the regions of the PEHs that can be populated after the absorption of radiation, constituting indeed the exploration of the PEHs of a system.

3.1 Electronic structure theory methods

The presence of the electronic repulsion operator makes the electronic Hamiltonian not separable in terms that depend on a single variable, and consequently it leads to the impossibility of solving exactly the electronic Schrödinger equation, in practice, for systems formed by more than one electron. Therefore, in those cases, the resolution of the electronic problem must be done by the introduction of some approximations. In the following lines one of the most common and important approximation introduced in order to solve the electronic problem is presented: the so-called Hartree-Fock (HF) method [1,2]. Next, three methods aimed to improve the HF description are shown, which are: the Configuration Interaction (CI) method , the Complete Active Space Self-Consistent Field (CASSCF) method, and the Complete Active Space Second-Order Perturbation Theory (CASPT2) method [1,2]. Despite the fact that other methods do exist in order to improve the HF result, as the Coupled-Cluster and the Møller-Plesset methods, here we focus on the CASSCF and CASPT2 strategies, because they are nowadays the only methods able to deal with medium-size systems and multi-configurational problems as those treated in the present thesis. Particular attention will be devoted to the resolution of the corresponding equations. Finally, since all of the employed computational strategies make use of a one-electron basis set in order to expand the electronic wave function, a brief subsec-

tion devoted to a particularly important basis set, the so-called atomic natural orbitals (ANO) basis sets, is provided.

3.1.1 The Hartree-Fock method

As mentioned above, the electron-electron repulsion operator determines the impossibility of obtaining exact solutions of the electronic Schrödinger equation in many-electron systems. A first remarkable approximation is to discard such a term, and consequently treat the electrons as independent particles subject to the potential field generated by the fixed nuclei. The wave function ψ_i describing the system is then equal to the product of the wave functions (the so-called molecular orbitals ϕ_j) representing the electrons.

$$\psi_i(r_1, r_2, ..., r_N) = \prod_{j=1}^{N} \phi_j(r_j) \tag{3.1}$$

Since equation 3.1 is the wave function of a many-electron system, it must be antisymmetric with respect to the interchange of coordinates of two electrons. The fulfillment of this condition transforms the wave function in the following form, the so-called Slater determinant [1]:

$$\psi_i(r_1, r_2, ..., r_N) = (N!)^{-\frac{1}{2}} \sum_{n=1}^{N!} (-1)^{p_n} P_n\{\phi_1(r_1)\phi_2(r_2)....\phi_N(r_N)\} \tag{3.2}$$

where P_n is an operator that generates the n^{th} permutation of the electron labels $1, 2, \ldots N$ and p_n is the number of transpositions (simple interchanges) required to obtain this permutation.

The HF approximation consists in taking as many-electron wave function a single configuration state function (CSF), which is formed

by one or a linear combination of Slater determinants. The HF method consists in determining the orbitals used to build such configuration state function by means of the variational principle. The aim of a HF calculation is then to obtain a stationary point of the expectation value of the electronic energy with respect to the orbitals occupying a single configuration state function.

In second quantization, a Slater determinant formed by some of the elements composing a basis of M orthogonal orbitals $\{\phi_p\}_{p=1,M}$ is expressed as an occupation-number vector of an abstract linear vector space (the Fock space) [2]:

$$|\mathbf{k}>=|k_1,k_2,...,k_M>\ ,\ k_p=\begin{cases}1 & \phi_p\ occupied\\ 0 & \phi_p\ unoccupied\end{cases} \tag{3.3}$$

In the HF method the optimization is performed with respect to unitary variations in the orbitals. A unitary matrix U can in general be expressed as the matrix exponential of an anti-Hermitian matrix k:

$$U^\dagger = U^{-1}\ ,\ U = exp(k) \tag{3.4}$$

$$k^\dagger = -k \tag{3.5}$$

It is possible to show that a unitary transformation U of the orbitals $\{\phi_p\}$ describing a single Slater determinant $|\mathbf{k}>$ to a different set of orthogonal orbitals $\{\tilde{\phi}_p\}$, determines the following change of the original determinant into $|\tilde{\mathbf{k}}>$, according to the next equations:

$$\tilde{\phi}_p = \sum_q \phi_q U_{qp} \tag{3.6}$$

$$|\tilde{\mathbf{k}}>= exp(-\hat{k})|\mathbf{k}> \tag{3.7}$$

$$\hat{k} = \sum_{pq} k_{pq} a_p^\dagger a_q \tag{3.8}$$

where k_{pq} are the elements of the anti-Hermitian matrix k (called orbital rotation parameters), $a_p^\dagger$ is the creation operator associated with orbital ϕ_p, and a_q is the annihilation operator associated with orbital ϕ_q. In the more general case of CSF, the transformation can be expressed in a totally similar fashion:

$$|\tilde{CSF}>= exp(-\hat{k})|CSF> \tag{3.9}$$

Equation 3.8 expresses the anti-Hermitian operator $\hat{k}$ associated with a general unitary transformation of the orbitals. However, considering only real orbitals and spin-symmetry constraint rotations, the operator $\hat{k}$ reduces to:

$$\hat{k} = \sum_{p>q} k_{pq} E_{pq}^- \tag{3.10}$$

$$E_{pq}^- = E_{pq} - E_{qp} \tag{3.11}$$

$$E_{pq} = a_{p\alpha}^\dagger a_{q\alpha} + a_{p\beta}^\dagger a_{q\beta} \tag{3.12}$$

where E_{pq} is the so-called singlet excitation operator, defined as shown in equation 3.12 in terms of spin-orbital creation and annihilation operators. For a general transformation of the wave function, equation 3.10 can be further simplified, since not all the rotational parameters

k_{pq} are required for such purpose. The latter are refereed as redundant parameters, and can be defined as those that fulfill the following condition:

$$E_{pq}^{-}|CSF>=0 \tag{3.13}$$

According to equation 3.8 and 3.9, a CSF can be expressed as the product of the matrix exponential of an appropriate anti-Hermitian matrix k and a fixed CSF built by a fixed set of orthogonal orbitals. This means that a general CSF can be written in a fixed basis of orthogonal orbitals as a function of the matrix k:

$$|CSF(\mathbf{k})>=exp(-\hat{k})|CSF> \tag{3.14}$$

Consequently, the expectation value of the electronic energy in HF theory is a function of the matrix k:

$$E(\mathbf{k})=<CSF(\mathbf{k})|\hat{H}|CSF(\mathbf{k})> \tag{3.15}$$

$$E(\mathbf{k})=<CSF|exp(\hat{k})|\hat{H}exp(-\hat{k})|CSF> \tag{3.16}$$

Writing equation 3.15 in a Taylor expansion around $k=0$, and using the Baker-Campbell-Hausdorff expansion [2] in equation 3.16,

$$E(\mathbf{k})=E^{(0)}+\mathbf{k^{T}E^{(1)}}+.... \tag{3.17}$$

$$E(\mathbf{k})=<CSF|\hat{H}|CSF>+<CSF|\left[\hat{k},\hat{H}\right]|CSF>+.... \tag{3.18}$$

it is possible to write the first derivatives of the expectation value of the

electronic energy with respect to the rotational parameters k_{pq} at the expansion point $k = 0$, as follows:

$$E_{pq}^{(1)} =< CSF| \left[E_{pq}^{-}, \hat{H} \right] |CSF > \tag{3.19}$$

that for real orbitals reduces to:

$$E_{pq}^{(1)} = 2 < CSF| \left[E_{pq}, \hat{H} \right] |CSF > \tag{3.20}$$

which is also equal to:

$$E_{pq}^{(1)} = -2 < CSF|\hat{H}E_{pq}^{-}|CSF > \tag{3.21}$$

Then the condition that an optimized HF state $|HF >$ must fulfill can be expressed as:

$$< HF| \left[E_{pq}, \hat{H} \right] |HF >= 0 \tag{3.22}$$

or equivalently as:

$$< HF|\hat{H}E_{pq}^{-}|HF >= 0 \tag{3.23}$$

in which the HF state has been written in term of a set of orbitals where $|HF >$ correspond to $k = 0$.

Equation 3.22 consequently constitutes the condition that an HF calculation must pursue by means of unitary rotations between all the couples of orbitals whose corresponding rotational parameters are not redundant. In a configuration state function is possible to classify the orbitals according to their occupation numbers in three classes. If an orbital is doubly occupied in all the Slater determinants used to build the CSF, then is refereed as an inactive orbital; if the occupation number

of an orbital is zero in all the Slater determinants that form the CSF, then is called virtual orbital; if an orbital has unspecified or arbitrary occupancy, then is referred as an active orbital. Inactive orbitals shall be labelled as *i, j, k, l*; virtual orbitals as *a, b, c, d, e*; and active orbitals as *v, w, x, y, z*. Using equations 3.11 and 3.12 and the above given definition of redundant parameters (equation 3.13), it can be shown that rotations mixing different classes are always non-redundant, and that rotations mixing inactive orbitals or virtual orbitals among themselves are always redundant. Rotations among active orbitals can either be redundant or nor, depending on the specific case. Taking into account these considerations, the HF condition for a closed-shell $|cs>$ system reduced to:

$$< cs|\hat{H}E_{ai}|cs >= 0 \tag{3.24}$$

This result, which is known as the Brillouin theorem [2], imply that a closed-shell HF state does not interact with singlet excited configurations.

A closed-shell HF state is represented by a variational optimized Slater determinant, which describes a state where each electron behaves as an independent particle (subject to Fermi correlation). It should then be possible to obtain such a state through the resolution of a one-electron Schrödinger equation, generating one independent-particle solution for each electron. The effective Hamiltonian of such one-electron Schrödinger equation (that will be further referred as $\hat{f}$ and called Fock operator) is a spin-free one-electron operator, and can consequently be expressed as follows:

$$\hat{f} = \sum_{pq} f_{pq} E_{pq} \tag{3.25}$$

The particular form of $\hat{f}$, specified by the values of the f_{pq}, must determine that the product generated by its eigenvalues represent a variationally optimized state. For a closed-shell system such a requirement is fulfilled rewriting the expectation value appearing in equation 3.24 as follows:

$$\begin{array}{c} < cs|\hat{H}E_{ai}|cs >=< cs|\left[E_{ai},\hat{H}\right]|cs >= \\ -\sum_{\sigma} < cs|\left[a^{\dagger}_{i\sigma},\left[a_{a\sigma},\hat{H}\right]\right]_{+}|cs > \end{array} \tag{3.26}$$

and imposing the equality:

$$f_{pq} = \frac{1}{2}\sum_{\sigma} < cs|\left[a^{\dagger}_{q\sigma},\left[a_{p\sigma},\hat{H}\right]\right]_{+}|cs > \tag{3.27}$$

In such a way, through the diagonalization of the Fock matrix it is possible to ensure the fulfillment of the HF condition.

Inserting equation 3.27 into expression 3.25, the Fock operator is defined as:

$$\hat{f} = \frac{1}{2}\sum_{\sigma}\sum_{pq} < cs|\left[a^{\dagger}_{q\sigma},\left[a_{p\sigma},\hat{H}\right]\right]_{+}|cs > E_{pq} \tag{3.28}$$

Substituting the Hamiltonian operator $\hat{H}$ appearing in equation 3.27 with its general expression in second quantization:

$$\hat{H} = \sum_{pq} h_{pq}E_{pq} + \sum_{pqrs} g_{pqrs}e_{pqrs} + h_{nuc} \tag{3.29}$$

(where h_{pq} represents the one-electron integrals of the electronic kinetic operator plus the electrons-nucleus repulsion operator , g_{pqrs} are the two-electron integrals of the electron-electron repulsion operator, h_{nuc} represents the nuclear-nuclear repulsion, and e_{pqrs} is the so-called two-

electron excitation operator) it is possible to write the elements of the Fock matrix in terms of the one and two-electron integrals h_{pq} and g_{pqrs}:

$$f_{pq} = h_{pq} + \sum_{i} (2g_{pqii} - g_{piiq}) \tag{3.30}$$

Diagonalization of the above constructed Fock matrix leads to the so-called canonical conditions [35,47]:

$$f_{pq} = \epsilon_p \delta_{pq} \tag{3.31}$$

Resolution of the latter expression will consequently provide a set of orbitals (the so-called canonical orbitals) that can be used to build a CSF for which the expectation value of the electronic energy is stationary: an optimized HF state. It must be noticed that the canonical conditions represents a set of non-linear equations that cannot be solved by a single diagonalization of the Fock matrix, since the canonical orbitals are not simply the eigenvectors of the Fock matrix, but they are also the orbitals from which the Fock matrix itself is constructed (see equation 3.27). Equation 3.31 is normally solved by means of the self-consistent field method. In this manner, the Fock matrix is initially constructed from a starting set of orthogonal orbitals, and then diagonalized. From the result of the diagonalization, a new set of orthogonal orbitals is obtained. The Fock matrix is then re-built using the new orbitals and an iterative process is thus established, where the Fock matrix is repeatedly constructed and diagonalized until the orbitals from which it is constructed are the same, within a given criteria, as those generated by its diagonalization.

By definition, the canonical orbitals diagonalize the Fock matrix. The Fock operator in the basis of canonical orbital can then be written

as:

$$\hat{f} = \sum_{p} \epsilon_p E_{pp} \tag{3.32}$$

from which is easy to show that the canonical orbitals are eigenfunctions of the Fock operator:

$$\hat{f} a^{\dagger}_{p\sigma} |vac> = \epsilon_p a^{\dagger}_{p\sigma} |vac> \tag{3.33}$$

whose eigenvalues, using equation 3.30, are equal to:

$$\epsilon_p = h_{pp} + \sum_{i} (2g_{ppii} - g_{piip}) \tag{3.34}$$

Actually the resolution of equation 3.31 produces a number of canonical orbitals that is normally larger that the number of electrons of the system. More specifically, the number of canonical orbitals will be equal to the dimension of the subspace spanned by the basis set employed. The HF state of a N-electron system is then obtained using the N canonical orbitals having the lowest eigenvalue of the Fock operator, since such a choice will determine the lowest expectation value of the electronic energy. The canonical orbitals employed to build the HF state are denoted as occupied orbitals, while the remaining are named virtual orbitals.

For a canonical occupied orbital ϕ_i and a canonical virtual orbital ϕ_a the corresponding eigenvalues are equal to:

$$\epsilon_i = h_{ii} + \sum_{j \neq i} (2g_{iijj} - g_{ijji}) + g_{iiii} \tag{3.35}$$

$$\epsilon_a = h_{aa} + \sum_{j} (2g_{aajj} - g_{ajja}) \tag{3.36}$$

Analyzing such expressions, it is possible to consider the eigenvalue of an occupied orbital ϕ_i as the energy resulting from the interaction of an electron place in ϕ_i with all the remaining electrons that form the system. The eigenvalue of a virtual orbital ϕ_a represents instead the energy resulting from the interaction of an electron place in ϕ_a with all the electrons of the system.

A powerful way of resolving the canonical conditions is by means of the so-called Roothaan-Hall formulation of the HF theory, in which the molecular orbitals $\{\phi_p\}$ are expanded in a set of atomic orbitals $\{\chi_\mu\}$ whose expansion coefficients $C_{\mu p}$ are used as variational parameters [1-4].

$$\phi_p = \sum_\mu \chi_\mu C_{\mu p} \tag{3.37}$$

In such a way, the otherwise required expensive transformation of the two-electrons integrals in the basis of the molecular orbitals it is not necessary. It is possible to shown that the expectation value of the electronic energy for a closed-shell HF state is equal to :

$$E(\mathbf{C}) = 2\sum_i h_{ii} + \sum_{ij}(2g_{iijj} - g_{ijji}) + h_{nuc} \tag{3.38}$$

Since the orbitals are chosen to be orthogonal, it is convenient to define the following HF Lagrangian:

$$L(\mathbf{C}) = E(\mathbf{C}) - 2\sum_{ij} \lambda_{ij}(< \phi_i|\phi_j > -\delta_{ij}) \tag{3.39}$$

Using the latter expression, the variational condition can be expressed in an unconstrained form as:

$$\frac{\partial L(\mathbf{C})}{C_{\mu k}} = 0 \tag{3.40}$$

that leads, in the case of real orbitals, to:

$$f_{\mu k} = \sum_{j} S_{\mu j} \lambda_{jk} \tag{3.41}$$

where $S_{\mu j}$ is equal to the integral between the atomic orbital χ_μ and the molecular orbital ϕ_j. Multiplication of equation 3.41 from the left by a set of orthonormal virtual orbitals that are orthogonal to the occupied molecular orbitals and by the set of occupied molecular orbitals gives:

$$f_{ak} = 0 \quad , \quad f_{ik} = \lambda_{ik} \tag{3.42}$$

Since for real orbitals the matrix λ is symmetric ($\lambda_{ik} = \lambda_{ki}$), it may be diagonalized by an unitary transformation that leaves the HF energy unchanged.

$$\lambda_{ik} = \epsilon_i \lambda_{ik} \tag{3.43}$$

Using such expression and expanding the molecular orbital in the atomic basis set according to equation 3.37, it is possible to write equation 3.41 as:

$$\sum_{\nu} f_{\mu\nu}^{AO} C_{\nu k} = \epsilon_k \sum_{\nu} S_{\mu\nu} C_{\nu k} \tag{3.44}$$

$$f_{\mu\nu}^{AO} = h_{\mu\nu} + \sum_{i} (2 g_{\mu\nu ii} - g_{\mu ii\nu}) \tag{3.45}$$

Equation 3.44 in matrix form constitutes the Roothaan-Hall equation [1-4]:

$$\mathbf{f^{AO}C} = \mathbf{SC}\epsilon \tag{3.46}$$

whose resolution will determine an optimized HF state.

Two points regarding equation 3.46 must be noticed. Firstly, for the same reason exposed with respect to the resolution of the canonical conditions (see equation 3.31), the Roothaan-Hall equation cannot be solved by a simple diagonalization but is instead work out using the self-consistent field approach. Secondly, as previously anticipated the Roothaan-Hall formulation avoid the expensive transformation of the two-electrons integrals in the basis of the molecular orbitals since the $\mathbf{f^{AO}}$ matrix can be entirely evaluated in the atomic orbital basis as follows:

$$f_{\mu\nu}^{AO} = h_{\mu\nu} + \sum_{\rho\sigma} D_{\rho\sigma}^{AO}(g_{\mu\nu\rho\sigma} - \frac{1}{2}g_{\mu\sigma\rho\nu}) \tag{3.47}$$

$$D_{\rho\sigma}^{AO} = 2\sum_{i} C_{\rho i}C_{\sigma i} \tag{3.48}$$

where the matrix $\mathbf{D^{AO}}$ is the atomic orbital representation of the one-electron density matrix $\mathbf{D}$ for a closed-shell system

$$D_{pq} =< cs|E_{pq}|cs > \tag{3.49}$$

$$\mathbf{D^{AO}} = \mathbf{CDC^{T}} \tag{3.50}$$

For small and medium size systems, the presented Roothaan-Hall formulation of the HF theory yields reasonable results, in particular when combined with the so-called DIIS acceleration scheme and the direct evaluation of the Fock matrix [2,5,6]. For large systems, diagonaliza-

tion of the Fock matrix required in the resolution of the Roothaan-Hall equation becomes however computationally impracticable, since such an operation scales to the third power with respect to the size of the system. In such cases, the problem is better solved using the so-called density-based HF theory [2]. The approach consists in a direct optimization of the HF energy expressed as a function of the one-electron density matrix in the atomic orbital basis $\mathbf{D^{AO}}$:

$$E(\mathbf{D^{AO}}) = Tr\mathbf{D^{AO}}\mathbf{h^{AO}} + \frac{1}{4}Tr\mathbf{D^{AO}}\mathbf{G^{AO}}(\mathbf{D^{AO}}) + h_{nuc} \tag{3.51}$$

$$G^{AO}_{\mu\nu}(\mathbf{D^{AO}}) = \sum_{\rho\sigma}(2g_{\mu\nu\rho\sigma} - g_{\mu\rho\sigma\nu})D^{AO}_{\rho\sigma} \tag{3.52}$$

The main advantage of such methods is the avoidance of the expensive diagonalization step required in the Roothaan-Hall formulation of the HF theory.

3.1.2 The Configuration Interaction method

The HF theory considers as wave function of a many-electron system a single configuration state function. The electrons are then described as independent particles subject only to Fermi correlation, and consequently the probability of finding two electrons having different spin in the same region of space is not equal to zero. The motion of electrons with opposite spins is then not correlated, due to an inadequate treatment of the Coulomb repulsion between the electrons. Such a fact is reflected in the HF energy, which is above the lower eigenvalue of the electronic Schrödinger equation. The absolute value of the difference between the latter and HF energy is called the electronic correlation en-

ergy [1,2]. For the reason mentioned above, the HF description is said to constitute a non-correlated method, and the missing description (either in the energy and in the wave function) is called electronic correlation. The next described methods aim to the partial recovering of such electronic correlation. Mathematically, the exact electronic wave function can be expanded in a basis form by all the Slater determinants that can be built distributing the electrons into all the orbitals that results from an HF calculation performed with an infinite atomic one-electron basis set. Since the number of determinants so defined is infinite, and since they will be obtained using molecular orbitals expressed in an infinite atomic orbital basis set, the impossibility of handling such a representation of the wave function is clear. The expansion of the electronic wave function in the basis of all the Slater determinants that can be obtained from distributing all electrons among all the available orbitals (independently if the orbitals have been built from an infinite atomic basis set or not) is called full CI expansion. In the ideally case in which the orbitals have been obtained from an infinite atomic basis set, the variational optimization of the full CI expansion leads to the exact electronic wave function; in the realistic case of a truncated atomic basis set, the variational optimization of the full CI expansion constitutes the exact electronic wave function in the space spanned by the employed atomic basis set. Even in that case, a full CI expansion is computationally extremely expensive except for relatively small molecular systems, since the number of Slater determinants increases very rapidly with the number of electrons and with the number of orbitals.

The CI method considers as the electronic wave function a linear combination of Slater determinants, the expansion coefficients of which are variationally determined [1,2]. Normally such determinants are formed by the substitution of one or more occupied orbitals of the

HF determinant with one or more virtual orbitals. The CI method rarely makes used of an entire full CI expansion but employs the latter in a truncated way, in which the electronic wave function is expanded in the basis of only certain classes of determinants. The set of determinants used in a CI calculation is refereed as the configuration space. For example, one common way to perform a CI calculation is to consider only the singly and doubly excited determinants obtained from the HF determinant substituting one or two occupied orbitals by one or two virtual orbitals, respectively. The strategy is known as the Singly and Doubly Excited Configuration Interaction method (SDCI). Normally, all forms of truncated CI methods (where the full CI expansion has been somehow truncated) improve the description of the molecular property with respect to a simple HF calculation. The truncated CI approaches have, however, a serious deficiency: they are not size consistent, which means that the energy of a many-particle system is not proportional to the number of constituent molecules in the limit of an infinite number of particles.

According to the above description, the electronic wave function $|\mathbf{C}>$ in the framework of the CI method is equal to:

$$|\mathbf{C}>=\sum_i C_i|i> \tag{3.53}$$

where $|i>$ are Slater determinants and the linear coefficients C_i are obtained by a variational optimization of the expectation value of the electronic energy:

$$\frac{\partial}{\partial C_i} < \mathbf{C}|\hat{H}|\mathbf{C} >= 0 \tag{3.54}$$

As proven by the variational principle, the solutions of the expression

3.54 represent the eigenfunctions of the following eigenvalue problem:

$$\mathbf{HC} = E\mathbf{C} \tag{3.55}$$

$$H_{ij} =< i|\hat{H}|j > \tag{3.56}$$

Consequently, the CI problem can be solved either performing an optimization of the expectation value of the electronic energy as described in equation 3.54, or by the resolution of the eigenproblem defined by equations 3.55 and 3.56.

Due to the normalization imposed to the wave function, the coefficients C_i are subjected to the condition:

$$\sum_i C_i^2 = 1 \tag{3.57}$$

which causes that only M-1 of the total M C_i coefficients are actually independent. Equation 3.53 then contains a redundancy related to normalization. The normalization condition is however easily eliminated using the following parametrization of the wave function:

$$|\mathbf{C} >= \frac{\sum_i C_i|i >}{\sqrt{\mathbf{C^T C}}} \tag{3.58}$$

The variation in the wave function is normally described with respect to some normalized reference state $|0 >$:

$$|0 >= \sum_i C_i^{(0)}|i > \tag{3.59}$$

$$|\mathbf{c} >= \sum_i c_i|i > \tag{3.60}$$

$$|\mathbf{C}>=|0>+|\mathbf{c}> \tag{3.61}$$

In order to better control the redundancy, it is useful to consider the variation of the wave function orthogonal to the reference state:

$$|\mathbf{C}>=|0>+\hat{P}|\mathbf{c}> \tag{3.62}$$

$$\hat{P}=1-|0><0| \tag{3.63}$$

where $\hat{P}$ projects out of the space spanned by $|0>$. The following parametrization of the wave function is introduced:

$$|\mathbf{C}>=\frac{|0>+\hat{P}|\mathbf{c}>}{\sqrt{1+<\mathbf{c}|\hat{P}|\mathbf{c}>}} \tag{3.64}$$

which allows to easily control the redundancy since $|\mathbf{C}>$ becomes parallel to the reference state $|0>$. Using equation 3.64 the CI energy results equal to:

$$E(\mathbf{c})=\frac{E^{(0)}+2\mathbf{c^T PHC^{(0)}}+\mathbf{c^T PHPc}}{1+\mathbf{c^T Pc}} \tag{3.65}$$

where $\mathbf{H}$ and $\mathbf{P}$ are the matrix representations of the Hamiltonian and the projector $\hat{P}$. The electronic gradient and Hessian at $\mathbf{c}=\mathbf{0}$ are, respectively:

$$\mathbf{E^{(1)}}=2\mathbf{PHC^{(0)}}=2(\mathbf{H}-E^{(0)}\mathbf{1})\mathbf{C^{(0)}} \tag{3.66}$$

$$\mathbf{E^{(2)}}=2\mathbf{P}(\mathbf{H}-E^{(0)}\mathbf{1})\mathbf{P} \tag{3.67}$$

In order to optimize the CI electronic energy as a stationary point

of the expectation value of the electronic energy, the Newton method is usually employed. According to it, from a starting point $\mathbf{x}$ an improved wave function $\mathbf{c}$ will be obtained by the following equation:

$$\mathbf{E^{(2)}}(\mathbf{x})\mathbf{c} = -\mathbf{E^{(1)}}(\mathbf{x}) \tag{3.68}$$

Considering as starting point the reference state $|0>$, the expression becomes:

$$\mathbf{E^{(2)}}(\mathbf{C^{(0)}})\mathbf{c} = -\mathbf{E^{(1)}}(\mathbf{C^{(0)}}) \tag{3.69}$$

From the initial point $|0>$, the optimization of the wave function must be directed orthogonally to the reference state $|0>$, since according to equation 3.64 any variation $|\mathbf{c}>$ perpendicular to $|0>$ will not change the wave function. It is then sufficient to consider only the solutions $|\mathbf{c}>$ of equation 3.69 that satisfied the condition:

$$\mathbf{C^{(0)^T}}\mathbf{c} = 0 \tag{3.70}$$

Making use of 3.70, it is possible to write equation 3.69 as

$$(\mathbf{E^{(2)}} + 2\alpha\mathbf{C^{(0)}}\mathbf{C^{(0)^T}})\mathbf{c} = -\mathbf{E^{(1)}} \tag{3.71}$$

where α is a numerical constant different from zero. Defining the following non-singular modified Hessian matrix $\mathbf{G}$:

$$\mathbf{G^{(2)}} = \mathbf{E^{(2)}} + 2\alpha\mathbf{C^{(0)}}\mathbf{C^{(0)^T}} \tag{3.72}$$

the Newton step (the solution of equation 3.69) can be then expressed as:

$$\mathbf{c} = -(\mathbf{G^{(2)}})^{-1}\mathbf{E}^{(1)} \tag{3.73}$$

which leads to the next final expression for $\mathbf{c}$:

$$\mathbf{c} = -\mathbf{C^{(0)}} + \frac{(\mathbf{H} - E^{(0)}\mathbf{1})^{-1}\mathbf{C^{(0)}}}{\mathbf{C^{(0)^T}}(\mathbf{H} - E^{(0)}\mathbf{1})^{-1}\mathbf{C^{(0)}}} \tag{3.74}$$

Substituting the latter in equation 3.64, the new normalized and improved CI vector $\mathbf{C}$ results equal to:

$$\mathbf{C} = \frac{(\mathbf{H} - E^{(0)}\mathbf{1})^{-1}\mathbf{C^{(0)}}}{\left\|(\mathbf{H} - E^{(0)}\mathbf{1})^{-1}\mathbf{C^{(0)}}\right\|} \tag{3.75}$$

The process is then repeated until a CI vector for which the gradient of the electronic energy becomes zero.

One shortcoming of the Newton method is that for each iteration in order to obtain a new CI vector (named macro iterations), a relatively large number of so-called micro iterations are needed for solving the linear equations 3.69. In order to reduce the number of micro iterations, a possible solution is to employ a quasi-Newton step [2,7]. The strategy makes use of an approximate Hessian matrix that can be more easily inverted, obtained replacing the true Hamiltonian with an approximate one. In such a way, the number of micro iterations becomes equal to the number of macro iterations, although the latter increase with respect the original implementation of the Newton method.

As previously point out, the CI wave functions are solutions of the eigenvalue problem defined by equations 3.55 and 3.56, and can consequently be obtained by the resolution of the eigenvalue-eigenfunction equation 3.55. For large CI expansions, the Hamiltonian matrix is impossible to be managed, and even more complex will be its diagonalization in order to obtained its eigenvalues and eigenvectors. Usually a complete diagonalization is not needed since in most of the cases the interest in centered in only a few eigenvalues. Selected eigenvalues of

the Hamiltonian can be determined by iterative methods, in which the individual values of the matrix $\mathbf{H}$ are not required and the eigenvalues and eigenvectors are generated by a sequence of linear transformations or contractions of the form:

$$\sigma = \mathbf{HC} \tag{3.76}$$

where $\mathbf{C}$ is some trial vector and σ the linearly transformed trial vector. Even if the CI problem is resolved performing an optimization of the electronic wave function, as in the above described Newton method, the evaluation of the improved CI vector (see equation 3.75) will require linear transformation as the one described by equation 3.76.

A very efficient method to perform the presented linear transformations is the so-called direct CI method [8], introduced by Roos in the earlier 1970s. It consists on carrying out the vector contractions directly from the second-quantization representation of the one- and two-electron operators $\hat{g}$ and $\hat{h}$ that constitute the Hamiltonian, that is, directly from the integrals h_{pq} and g_{pqrs}. Such a strategy is convenient for two reasons. Firstly, since the one and two electron operators couple only determinants that differ in at most one and two occupations, respectively, the determinant-based representations of the one and two electron operators $\mathbf{h}^{\mathbf{SD}}$ and $\mathbf{g}^{\mathbf{SD}}$ are very sparse. Secondly, for large CI expansion the construction of the entire $\mathbf{h}^{\mathbf{SD}}$ and $\mathbf{g}^{\mathbf{SD}}$ matrices will be extremely computational demanding.

In order to properly implement the direct CI method, it is important to develop a scheme of work that efficiently determines for each Slater determinant all the determinants to which it is connected by single and double excitations, thereby identifying the nonzero elements of the Hamiltonian matrix directly. The goal is achieved representing

Slater determinants as products of alpha and beta strings, and by using graph to order these strings [2,9,10]. These techniques together provide in fact a compact way of addressing and storing information about the occupations of the Slater determinants and of representing the determinants belonging to a particular expansion.

3.1.3 Complete Active Space Self-Consistent Field method

As mentioned in the preceding section, the variational optimization of a full CI expansion will provide the exact electronic wave function, at least in the space spanned by the chosen atomic basis set. Such an expansion of the wave function is then able to recover all the electronic correlation missed in the HF description. The electron correlation is normally classified as static and dynamic. The former is related to the presence of near-degeneracies among configurations while the latter arises from the Coulomb repulsion of the electrons. The used of truncated CI expansions will consequently provide only part of the total electronic correlation. In the design of a truncated CI expansion it is important to distinguish between static and dynamical correlation [2]. Static correlation is treated by retaining, in the truncated expansion, the dominant configurations of the full CI expansion, as well as those configurations that are nearly degenerate with the dominant configurations. These configurations are often referred to as the reference configuration of the CI wave function. Dynamic correlation is subsequently treated by adding to the wave function configurations generated by excitations out of the reference space, for example all singly and doubly excited determinants.

In order to choose the appropriate reference space, it is mandatory to distinguish between the so-called single-configuration and the multi-configuration systems. The formers are mainly described by the single

configuration that constitutes the HF wave function, which consequently forms the reference space. The latter are described by more than one configuration. It is then necessary to use a more flexible set of orbitals from which all the relevant configuration can be obtained. It is important to notice that the single- or multi-configuration nature of a system depends on the particular situation in which is considered. A molecule can be described by a single configuration at the minimum of the ground state, while it has a multi-configuration character in other regions of the PEH, as in the dissociation limit or in CIs. Consequently, if such regions are analyzed (as it normally occurs in photophysical and photochemical studies) is fundamental to use a method able to describe the multi-configuration character of the system.

An important computational strategy able to effectively describe the multi-configuration character of a system is the so-called Multiconfigurational Self-Consistent Field (MCSCF) method [2]. In the MCSCF algorithms, the electronic wave function is expressed as a CI expansion where the orbitals are variationally optimized simultaneously with the coefficients of the electronic configuration, thereby ensuring that the orbitals employed in the wave function are optimal for the problem at hand. One of the most successfully implementation of multiconfigurational self-consistent field theory is the so-called CASSCF method [11]. The available orbitals in order to construct the Slater determinants of the CI expansion in the CASSCF method are partitioned into a set of inactive orbitals, a set of active orbitals, and a set of secondary orbitals. The CASSCF wave function will then be formed by all Slater determinants in which the inactive orbitals are always doubly occupied, the active orbitals have any possible occupation consistent with the total number of electrons and spatial and spin constraints of the system, and the secondary orbitals are always unoccupied. The resulting set of de-

terminants is refereed as the CAS space. Having defined the number of inactive orbitals, the number of electrons that can be distributed among the active orbitals is consequently fixed. Such quantity is referred as the number of active electrons.

According to the above discussion, the CASSCF wave function can in general be expressed as:

$$|\mathbf{k}, \mathbf{C}>= exp(-\hat{k}) \sum_i C_i |i> \tag{3.77}$$

where $|i>$ are Slater determinants, C_i are the expansion coefficients, and $\hat{k}$ is the anti-Hermitian operator related with an unitary transformation of the orbitals. The parametrization of the CASSCF wave function is a straightforward combination of the parametrization of the HF wave function (see equation 3.14) and of the CI wave function (see equation 3.64).

$$|\mathbf{C}>= exp(-\hat{k}) \frac{|0> + \hat{P}|\mathbf{c}>}{\sqrt{1 + <\mathbf{c}|\hat{P}|\mathbf{c}>}} \tag{3.78}$$

$$|0>= \sum_i C_i^{(0)} |i> \tag{3.79}$$

$$|\mathbf{c}>= \sum_i c_i |i> \tag{3.80}$$

$$\hat{k} = \sum_{p>q} k_{pq} E_{pq}^{-} \tag{3.81}$$

where $|0>$ is the reference state, and the operator $\hat{P}$ projects out the component of the reference state from $|\mathbf{c}>$. Equation 3.78 allows to easily control the redundancy due to the configuration space, since it becomes parallel to the reference state (see the discussion in the "Configuration Interaction method" section). As in HF theory, the operator

$\hat{k}$ should contain only the parameters k_{pq} associated to nonredundant orbital rotations. In the CASSCF theory, the question of orbital redundancies is more difficult because of the coupling to the configuration space. In general, it can be proof that redundant rotations satisfy the following condition:

$$E_{pq}^{-}|0>=\sum_{i} c_i|i> \tag{3.82}$$

The orbital rotation induced by E_{pq}^{-} is then redundant if its effect on $|0>$ may be consider by a variation in the configuration space. It turns out that in the CASSCF theory all intraspace rotations (such as inactive-inactive, active-active, and virtual-virtual rotations) are redundant, while all interspace rotations (such as inactive-active, active-virtual, virtual-inactive) are not, at least in the sense expressed by equation 3.82.

According to the adopted parametrization of the wave function (see equation 3.78), the latter can be represented by the next defined vector λ that highlights its dependence on the configuration and orbital parameters $\mathbf{c}$ and $\mathbf{k}$:

$$\lambda = \begin{pmatrix} \mathbf{c} \\ \mathbf{k} \end{pmatrix} \tag{3.83}$$

The gradient and the Hessian matrix can then be written in the following block form:

$$\mathbf{E^{(1)}} = \begin{pmatrix} {}^{\mathbf{c}}\mathbf{E^{(1)}} \\ {}^{\mathbf{o}}\mathbf{E^{(1)}} \end{pmatrix} \tag{3.84}$$

$$\mathbf{E^{(2)}} = \begin{pmatrix} {}^{\mathbf{cc}}\mathbf{E^{(2)}} & {}^{\mathbf{co}}\mathbf{E^{(2)}} \\ {}^{\mathbf{oc}}\mathbf{E^{(2)}} & {}^{\mathbf{oo}}\mathbf{E^{(2)}} \end{pmatrix} \tag{3.85}$$

where the left superscripts **c** and **o** indicate differentiation with respect to configuration and orbital parameters, respectively. It is possible to show that at $\lambda = \mathbf{0}$, the gradient is equal to:

$$ {}^{c}E_{i}^{(1)} = 2 < i|\hat{P}\hat{H}|0 > \tag{3.86} $$

$$ {}^{o}E_{pq}^{(1)} =< 0| \left[E_{pq}^{-}, \hat{H} \right] |0 > \tag{3.87} $$

As for the CI method, the CASSCF wave function can be obtained through the optimization of the electronic energy by means of the Newton method. Considering as starting point the vector $\zeta^{(\mathbf{0})}$:

$$ \zeta^{(\mathbf{0})} = \begin{pmatrix} C^{(0)} \\ 0 \end{pmatrix} \tag{3.88} $$

it is sufficient to take into account the modifications of the wave function that are orthogonal to $\zeta^{(\mathbf{0})}$, since according to the adopted parametrization, only such variations can actually affect the CASSCF wave function. Then each Newton step λ satisfies the following equation:

$$ \lambda = \mathbf{P}\lambda \tag{3.89} $$

where $\mathbf{P}$ is the matrix representation of the operator $\hat{P}$ that projects out of the space spanned by $\zeta^{(\mathbf{0})}$. Since the Newton method may sometimes lead to very long steps that cannot be justified based on the second-order expansion of the energy function, the Newton strategy is better implemented in a more sophisticated version called trust-region method [12]. In the improved modified Newton method, the local quadratic expansion of the electronic energy is optimized within a restricted region around the expansion point, the so-called trust region. Consequently, for each

iteration the obtained step λ must satisfy the following inequality:

$$\|\lambda\| \leq h \tag{3.90}$$

where h is the trust radius, a positive numerical parameter that defines the region in which the second-order surface is assumed to be a good approximation to the exact surface. The most appropriate value for the trust radius depends on the system under study: larger for harmonic surfaces, smaller for anharmonic ones. In practice, there is not a priori way of selecting h, and a update scheme based on the result gained in the previous iteration is adopted. Having chosen a value of h, the trust-region method starts by determining the Newton step. If it satisfies equation 3.90, then the optimization follows the original implementation of the Newton method. In the case in which the Newton step is not smaller than or equal to h, the next step is taken as a stationary point on the boundary of the thrust region (either a minimum or a saddle point depending if the optimization is performed for the ground or an excited state, respectively). Such a point is provided by the minimization with respect to the variable λ of the next Lagrangian:

$$L(\lambda, \mu) = E^{(0)} + \mathbf{E^{(1)^T}}\lambda + \frac{1}{2}\lambda^{\mathbf{T}}\mathbf{E^{(2)}}\lambda - \frac{1}{2}\mu(\lambda^{\mathbf{T}}\mathbf{P}\lambda - h^2) \tag{3.91}$$

from which the following equation defining the level-shifted Newton step λ is obtained:

$$(\mathbf{E^{(2)}} - \mu\mathbf{1})\mathbf{P}\lambda = -\mathbf{E^{(1)}} \tag{3.92}$$

where μ is called the level-shift parameter. Assuming that μ does not coincide with any of the eigenvalues of $\mathbf{E^{(2)}}$, it is possible to express λ

in the form:

$$\lambda(\mu) = -(\mathbf{E^{(2)}} - \mu\mathbf{1})^{-1}\mathbf{E^{(1)}} \tag{3.93}$$

As it is make apparent from equation 3.93, the level-shifted Newton step λ depends on the chosen value for the level-shift parameter μ. It is then fundamental to select μ so that the step has the correct length ($\|\lambda\| = h$) and so that the step has the appropriate structure: a minimum point for ground state optimization, a saddle point for excited states. In fact, according to the variational principle applied for a linear expansion of the wave function, the Hessian matrix of the K^{th} electronic state must have $K-1$ negative eigenvalues. Without entering into the details, it can be shown that such condition is in general satisfied selecting among the possible values of μ the one that fulfills certain inequalities with respect to the eigenvalues of the Hessian matrix [2,13]. Consequently, for each iteration the trust-region method must first determine an appropriate value of μ through a process that evaluates the eigenvalues of the Hessian matrix, and then obtain the level-shifted Newton step. In view of the large number of parameters in a CASSCF calculation, this two-step procedure is cumbersome. A better approach that replaces the two-step procedure by a single eigenvalue problem, is the Newton eigenvector method [2], where the parameters of the CASSCF state are written in the so-called intermediate normalization form:

$$\zeta = \zeta^{(\mathbf{0})} + \mathbf{P}\lambda \tag{3.94}$$

Furthermore, introducing the modified Hessian matrix $\mathbf{G}$ called augmented Hessian:

$$\mathbf{G} = \mathbf{E^{(2)}} + \zeta^{(\mathbf{0})}\mathbf{E}^{(\mathbf{1})^{\mathbf{T}}} + \mathbf{E}^{(\mathbf{1})}\zeta^{(\mathbf{0})^{\mathbf{T}}} \tag{3.95}$$

it is possible to recast the second-order expansion of the electronic energy as:

$$Q(\zeta) = E^{(0)} + \frac{1}{2}\zeta^{\mathbf{T}}\mathbf{G}\zeta \tag{3.96}$$

Such expression can be optimized subject to the two following constraints, ensuring that the step preserve the intermediate normalization (equation 3.94) and that it is on the boundary of the trust region, respectively:

$$\zeta^{\mathbf{T}}(\mathbf{O})\zeta = 1 \tag{3.97}$$

$$\zeta^{\mathbf{T}}\mathbf{P}\zeta = h^2 \tag{3.98}$$

where $\mathbf{O} = \mathbf{1} - \mathbf{P}$. Defining the Lagrangian:

$$L(\zeta, \mu, \nu) = \frac{1}{2}\zeta^{\mathbf{T}}\mathbf{G}\zeta - \frac{1}{2}\nu(\zeta^{\mathbf{T}}\mathbf{O}\zeta - 1) - \frac{1}{2}\mu(\zeta^{\mathbf{T}}\mathbf{P}\zeta - h^2) \tag{3.99}$$

and setting equal to zero the result of the differentiation of the latter with respect to ζ, the next equality is obtained:

$$\mathbf{G}\zeta = \nu\mathbf{O}\zeta + \mu\mathbf{P}\zeta \tag{3.100}$$

For a fixed value of μ, equation 3.100 can be recasted in the form of a generalized eigenvalue problem with eigenvector ζ and eigenvalue ν:

$$\mathbf{G}\zeta = \nu\mathbf{T}(\alpha)\zeta \tag{3.101}$$

where

$$\mathbf{T}(\alpha) = \mathbf{O} + \alpha^2 \mathbf{P} \tag{3.102}$$

It is worth noticing that the projection of equation 3.101 (whose resolution constitute the Newton eigenvalue method) from the left by $\mathbf{P}$ leads to the standard level-shifted Newton equation (see expression 3.92). It is possible to further express equation 3.101 as a standard symmetric eigenvalue problem:

$$\mathbf{G}(\alpha)\xi(\alpha) = \mu\xi(\alpha) \tag{3.103}$$

where

$$\xi(\alpha) = \mathbf{T^{1/2}}(\alpha)\zeta \tag{3.104}$$

and $\mathbf{G}(\alpha)$ is the so-called gradient-scaled augmented Hessian, defined as follows:

$$\begin{aligned} \mathbf{G}(\alpha) &= \alpha^2 \mathbf{T^{-1/2}}(\alpha)\mathbf{G}\mathbf{T^{-1/2}}(\alpha) \\ &= \mathbf{E^{(2)}} + \alpha\zeta^{(\mathbf{0})}\mathbf{E^{(1)^T}} + \alpha\mathbf{E^{(1)}}\zeta^{(\mathbf{0})^\mathbf{T}} \end{aligned} \tag{3.105}$$

Using equation 3.104 and 3.102, $\zeta(\alpha)$ can be written as a function of $\xi(\alpha)$:

$$\zeta(\alpha) = \zeta^{(\mathbf{0})} + \alpha^{-1}\mathbf{P}\xi(\alpha) \tag{3.106}$$

Consequently, in the Newton eigenvalue method the CASSCF step ζ is obtained first solving the eigenvalue problem 3.103, and then employing equation 3.106.

As mentioned above, the advantage of this strategy with respect to the trust-region method is that it allows to generate the correction to

the wave function in a single step. The reason is that the real Hessian matrix is a projection of the gradient-scaled augmented Hessian. Such a fact determines that the eigenvalues of the gradient-scaled augmented Hessian $\{\mu_i\}$ are related to the eigenvalues of the true Hessian $\{\epsilon_j\}$, through the following relationship:

$$\mu_1 \leq \epsilon_1 \leq \mu_2 \leq \cdots \leq \mu_n \leq \epsilon_n \leq \mu_{n+1} \tag{3.107}$$

where the zero eigenvalue of $\mathbf{E^{(2)}}$(associated with the reference vector) has been omitted from $\{\epsilon_j\}$.

Expression 3.107 implies that the correction to the K^{th} electronic state having the adequate structure ($K-1$ negative eigenvalues of the Hessian matrix) is obtained selecting the step ξ associated with the eigenvalue μ that satisfies the proper inequalities with the eigenvalues of the Hessian matrix, in a process that does not require the explicit evaluation of $\{\epsilon_j\}$. Thus, for ground-state calculations, the first eigenvector of the gradient-scaled augmented Hessian is chosen; for calculations of the lowest excited state, the second eigenvector is selected, and so on.

In the discussion of CASSCF theory, the wave function has been expressed using a redundant parametrization of the configuration space (see equation 3.78), that presents the advantage of simplicity. In some situations it is however better to remove such a redundancy and use a parametrization where the electronic states are described by a set of independent, nonredundant variables. Such situation arises in the so-called state-averaged MCSCF scheme, where several electronic states are generated in the same orbital basis [14]. The orbitals are in fact not optimized separately for each state but are instead determined to minimize an averaged energy of all the computed states. This is accomplished by introducing the following energy function where each state

contributes with a weight factor w_I.

$$E = \sum_{I}^{n} w_I E_I \tag{3.108}$$

where E_I is the electronic energy of the state I.

The description of each electronic state is thus performed employing orbitals that are not optimal for each state separately. The method provides, however, a set of orthonormal, noninteracting electronic states. The state-averaged approach is normally used in photochemical and photophysical studies (as the ones presented in this thesis) since it gives an equally good description of all the computed electronic states, which in turn allows a direct comparison among them.
An electronic state $|\tilde{I}>$ is here described as a function of a reference state $|I>$ using the following nonredundant parametrization, obtained employing an exponential unitary parametrization of the configuration space:

$$|\tilde{I}>= exp(-\hat{k})exp(-\hat{R})|I> \tag{3.109}$$

where $\hat{k}$ is the orbital rotation operator (see equation 3.81) and $\hat{R}$ is a linear combination of state-transfer operators, define as:

$$\hat{R} = \sum_{\substack{K>J,\\ J\leq n}} R_{KJ}\left(|K><J| - |J><K|\right) \tag{3.110}$$

where J refers to any of the computed n states for which the state-averaged energy function 3.108 is optimized, and K refers to these states and to the orthogonal complement. Substituting equation 3.109 into equation 3.108, the following energy function is obtained:

$$E(\mathbf{R},\mathbf{k}) = \sum_{I}^{n} w_I < I|exp(\hat{R})exp(\hat{k})\hat{H}exp(-\hat{k})exp(-\hat{R})|I > \quad (3.111)$$

which can then be optimized using a standard second-order procedure as either the trust-region method or the Newton eigenvector strategy.

3.1.4 The Complete Active Space Second-Order Perturbation Theory method

The CASSCF method is able to correctly describe the static electronic correlation of a multi-configuration system. In order to recover the remaining dynamic electronic correlation, one possibility will be the use of the Multi-Reference Singly and Doubly excited Configuration Interaction method (MRSDCI). It consists on performing a SDCI calculation employing a multi-reference space. Despite the effectiveness of such a strategy, it presents the important shortcoming of a high computational cost. A method based on non-degenerate perturbation theory, where the zeroth-order wave function is multiconfigurational, has been shown to be a more viable alternative. Among multi-reference perturbation algorithms, the CASPT2 method, in which the zeroth-order wave function is taken to be a CASSCF wave function and the correction to the energy is calculated up to second-order [15-19], has revealed itself especially efficient. This method will be described in the next section.

The main idea of all perturbation methods is to make a proper partition of the Hamiltonian operator $\hat{H}$ in two parts:

$$\hat{H} = \hat{H}_0 + \hat{U} \quad (3.112)$$

where $\hat{H}_0$ is the so-called zeroth-order Hamiltonian and $\hat{U}$ is the pertur-

bation.

$$\hat{U} = \hat{H} - \hat{H}_0 \tag{3.113}$$

The orthonormal eigenfunctions of the zeroth-order Hamiltonian

$$\hat{H}_0|i^{(0)}>= E_i^{(0)}|i^{(0)}> \tag{3.114}$$

are then used to expand the eigenfunction $|0>$ of the exact Hamiltonian

$$\hat{H}|0>= E|0> \tag{3.115}$$

The exact wave function and energy are approximated by $|0^{(0)}>$ and $E^{(0)}$ at zeroth-order level, while for higher accuracy they can be expanded in order of the perturbation $\hat{U}$ as:

$$|0>= \sum_{k=0}^{\infty} |0^{(k)}> \tag{3.116}$$

$$E = \sum_{k=0}^{\infty} E^{(k)} \tag{3.117}$$

where for $k \neq 0$ the $|0^{(k)}>$ and $E^{(k)}$ are the K^{th} correction to the wave function and energy, respectively. Substituting equations 3.116 and 3.117 into 3.115, and imposing the following intermediate normalization to $|0>$:

$$< 0^{(0)}|0>= \sum_{k=0}^{\infty} < 0^{(0)}|0^{(k)}>= 1 \tag{3.118}$$

it is possible to obtain the next expression that determines the n^{th}-order correction of the wave function in terms of the lower-order corrections of the wave function.

$$(\hat{H}_0 - E^{(0)})|0^{(n)}> = -\hat{U}|0^{(n-1)}> + \sum_{k=1}^{n} E^{(k)}|0^{(n-k)}> \qquad (3.119)$$

Introducing the projector $\hat{P}$:

$$\hat{P} = 1 - |0^{(0)}><0^{(0)}| \qquad (3.120)$$

equation 3.119 can be written as

$$|0^{(n)}> = -\hat{P}(\hat{H}_0 - E^{(0)})^{-1}\hat{P}\left(\hat{U}|0^{(n-1)}> - \sum_{k=1}^{n} E^{(k)}|0^{(n-k)}>\right)$$

(3.121)

Making use of equation 3.121, the n^{th}-order correction of the electronic energy can be expressed as:

$$E^{(n)} = <0^{(0)}|\hat{U}|0^{(n-1)}>\ ,\ n > 0 \qquad (3.122)$$

showing that the n^{th}-order correction of the energy can be obtained from the $(n-1)^{th}$-order correction of the wave function.

By the reformulation of the above presented perturbation theory using the variational Lagrangian technique, it can be proven that actually from the n^{th}-order correction of the wave function the $(2n+1)^{th}$-order correction of the energy can be obtained. Such a result is known as the Wigner's $2n+1$ rule [2], and is mathematically expressed by the following equation:

$$E^{(2n+i)} = \mathbf{C^{(n+i-1)^T} U C^{(n)}} - \sum_{k=1}^{2n+i-2} \sum_{m=max(1,n+i-k)}^{min(n+i-1,2n+i-k-1)} E^{(k)} \mathbf{C^{(m)^T} C^{(2n+i-m-k)}} \quad (3.123)$$

where $\mathbf{C^{(n)}}$ is the matrix representation of $|0^{(n)}>$ (see equation 3.121):

$$\mathbf{C^{(n)}} = -\mathbf{P}(\mathbf{H_0} - E^{(0)}\mathbf{1})^{-1}\mathbf{P}\left(\mathbf{U C^{(n-1)}} - \sum_{k=1}^{n-1} E^{(k)} \mathbf{C^{(n-k)}}\right) \quad (3.124)$$

According to the above equations, the first-order correction to the wave function, $\mathbf{C^{(1)}}$, and the second-order correction to the energy, $E^{(2)}$, are equal to:

$$\mathbf{C^{(1)}} = -\mathbf{P}(\mathbf{H_0} - E^{(0)}\mathbf{1})^{-1}\mathbf{P U C^{(0)}} \quad (3.125)$$

$$E^{(2)} = \mathbf{C^{(0)^T} U C^{(1)}} \quad (3.126)$$

It is important to remind that the success of perturbation theory depends critically on the ability to provide a suitable zeroth-order Hamiltonian $\hat{H}_0$, which means that it must incorporate the main feature of the exact Hamiltonian $\hat{H}$, and consequently implying that the corresponding perturbation operator $\hat{U}$ is in some sense significantly smaller the chosen zeroth-order operator $\hat{H}_0$. Moreover, its eigenvalues and eigenvectors must be available, since they are used to expand the exact wave function.

Having introduced the basic ideas and main results of perturbation theory (the previously derived equations are in fact valid for any choice of zeroth-order Hamiltonian and perturbation operator) let us

examine the CASPT2 method. As mentioned above, the main goal of the CASPT2 strategy is the ability to describe a multi-configuration system. For this purpose, the CASSCF wave function $|0>$ is used as reference in the CASPT2 method. Similar to Møller-Plesset theory where the zeroth-order Hamiltonian is the Fock operator in the canonical representation, in the CASPT2 method the next define CASSCF Fock operator $\hat{f}$ is used in order to build $\hat{H}_0$ [18,19]:

$$\hat{f} = \frac{1}{2} \sum_{\sigma} \sum_{pq} < 0| \left[a^{\dagger}_{q\sigma}, \left[a_{p\sigma}, \hat{H} \right] \right]_{+} |0 > E_{pq} \tag{3.127}$$

$$\hat{f} = \sum_{pq} f_{pq} E_{pq} \tag{3.128}$$

$$f_{pq} = \frac{1}{2} \sum_{\sigma} < 0| \left[a^{\dagger}_{q\sigma}, \left[a_{p\sigma}, \hat{H} \right] \right]_{+} |0 > \tag{3.129}$$

The previous expression can be obtained substituting in the definition of the Fock operator (see equation 3.28) the closed-shell state $|cs>$ with the CASSCF wave function $|0>$. The $\hat{f}$ operator can then be used to define the following zeroth-order Hamiltonian:

$$\hat{H}_0 = E^{(0)} |0 >< 0| + \hat{P} \hat{f} \hat{P} \tag{3.130}$$

where $\hat{P}$ is the projector:

$$\hat{P} = 1 - |0 >< 0| \tag{3.131}$$

and $E^{(0)}$ is the zeroth-order energy, equal to the expectation value of the CASSCF Fock operator:

$$E^{(0)} =< 0|\hat{f}|0 > \tag{3.132}$$

Equation 3.130 defines an operator having $|0>$ as eigenfunction but such a choice for $\hat{H}_0$ is not convenient since it can be shown that the corrections would then, already to first order, involve the full set of determinants belonging to the full CI expansion. To avoid such shortcoming, a diagonal block structure of the matrix representation of the zeroth-order Hamiltonian is imposed [17]. This is accomplished by defining $\hat{H}_0$ as follows:

$$\hat{H}_0 = E^{(0)}|0><0| + \hat{P}_K\hat{f}\hat{P}_K + \hat{P}_{SD}\hat{f}\hat{P}_{SD} + \hat{P}_{TQ}\hat{f}\hat{P}_{TQ} + \cdots \quad (3.133)$$

in terms of the orthogonal projectors:

$$1 = |0><0| + \hat{P}_K + \hat{P}_{SD} + \hat{P}_{TQ} + \cdots \quad (3.134)$$

where $\hat{P}_K$ projects onto the part of the CAS space that is orthogonal to $|0>$, $\hat{P}_{SD}$ projects onto the space spanned by the singly and doubly excited configurations from $|0>$ that are not contained in the CAS space, $\hat{P}_{TQ}$ onto the space spanned by the triply and quadruply excited configurations orthogonal to the CAS space, and so on.
The block-diagonal structure imposed by the projectors ensures that the corrections to the wave function truncate at a finite level of excitation. For example, the first-order correction $|0^{(1)}>$ contains at most double excitation. In fact, the latter can be written as a linear combination of all single and double excitation from $|0>$, according to the so-called internally contracted scheme [18,19]:

$$|0^{(1)}> = \sum_{pq} C^{(1)}_{pq} E_{pq}|0> + \sum_{pq \geq rs} C^{(1)}_{pqrs} e_{pqrs}|0> \quad (3.135)$$

where the indices q and s refer to either inactive or active orbitals, while

the indices p and r refer to either active or secondary orbitals.
The first-order correction $\mathbf{C^{(1)}}$ can be obtained using equation 3.135 and 3.125, modifying the latter according to the fact that the configurations appearing in equation 3.135 constitute a nonorthogonal basis.

$$\mathbf{C^{(1)}} = -\mathbf{P}(\mathbf{H_0} - E^{(0)}\mathbf{S})^{-1}\mathbf{PUC^{(0)}} \tag{3.136}$$

where

$$S_{ij} =< i|j > \tag{3.137}$$

and $|i >$ refers to one of the configurations $E_{pq}|0 >$ or $e_{pqrs}|0 >$. The second-order CASPT2 energy correction can then be calculated using equation 3.126.

The presented formulation of the CASPT2 method was described in two papers by Andersson et al. in 1990 and 1992 [18-19]. It was shown that the CASSCF Fock operator $\hat{f}$ defined in equation 3.127 can be divided in two terms, one whose matrix representation is diagonal,$\hat{f}_D$, and the other whose matrix representation is not diagonal, $\hat{f}_N$.

$$\hat{f} = \hat{f}_D + \hat{f}_N \tag{3.138}$$

In the first paper, [18] only the $\hat{f}_D$ term was used in the definition of the zeroth-order Hamiltonian (see equation 3.133). Despite the important decrease in the required computational effort, in the second paper [19] it was shown that such simplification leads to unsatisfactory results. For that reason, the method was reformulated taking into account the full CASSCF Fock operator $\hat{f}$ in the construction of the zeroth-order Hamiltonian. The later algorithm [19], as currently implemented in the MOLCAS software, has been used in the calculations performed in the

thesis.

3.1.5 Atomic natural orbitals basis sets

In all the above described methods, the many-electron wave function is written as a linear combination of one-electron functions called molecular orbitals, which in turn are expanded in a one-electron basis set. The features of the selected one-electron basis set will consequently strongly determine the accuracy of the wave function obtained and that of the results derived from the calculation.

In principle, the correct one-electron basis set should be a complete one, but since we are working in an infinite dimensional Hilbert space, that would mean an infinite basis set. Due to the practical impossibility to work with an infinite number of basis functions, all the basis set employed are consequently unable to span the entire space and will introduce an error to the evaluation of the electronic wave function. One of the ability of a good theoretical chemist is then the capacity of selecting an appropriate basis set in which the ab initio method employed will give the correct accuracy in order to describe the chemical process under study, without requiring a too high computational cost. In this respect, calibration calculations are mandatory.

As shown by many different studies, and as attested by the long experience of some theoretical groups (as the QCEXVAL group of the *Universitat de València*), a particular type of basis set has proven its capacity to correctly describe the properties of excited states: the atomic natural orbitals basis sets (ANOs) [20,21].

They have been built by using a general contraction scheme, what means that, unlike the segmented basis sets, each primitive contribute to all contracted functions. A key property of ANOs is that they have

been constructed from post HF ab initio calculations. In particular, they have been defined from the natural orbitals obtained from SDCI atomic calculations, using the natural occupation numbers as indicators of the relative importance of each function. This entails that part of the correlation energy is already taken into account using ANOs basis sets. Since a proper description of the correlation effects has been shown to be of primary importance in the study of excited states, their wide use in the field of photophysics and photochemistry research is then well understood.

3.2 Exploration of the potential energy hypersurfaces

Many different strategies have been formulated in order to find critical points on a PEH, such as minimum points, saddle points, minimum energy crossing points, etc. Since a correct description of all of such methodologies goes beyond the purpose of the thesis, we provide only a brief discussion on the main characteristics of the minimum energy path (MEP) technique, whose implementation has provided most of the results of the present work.

3.2.1 Minimum Energy Path calculation

The MEP technique is a powerful method able to describe, if present, a barrierless path. In order to perform such a task, a minimization of the energy on a hyperspherical cross section of the PEH centered on the initial geometry and characterized by a predefined radius is performed. A new constrained optimization is then carried out from the so-obtained minimized geometry, on which the hyperspherical cross section is now

centered. This process is repeated until an increase of the energy is found. Finally, the global method will provide a steepest descend path, whose amplitude of each step is determined by the chosen value for the hyperspherical radius. A pictorial representation of the method is given in Figure 3.1.

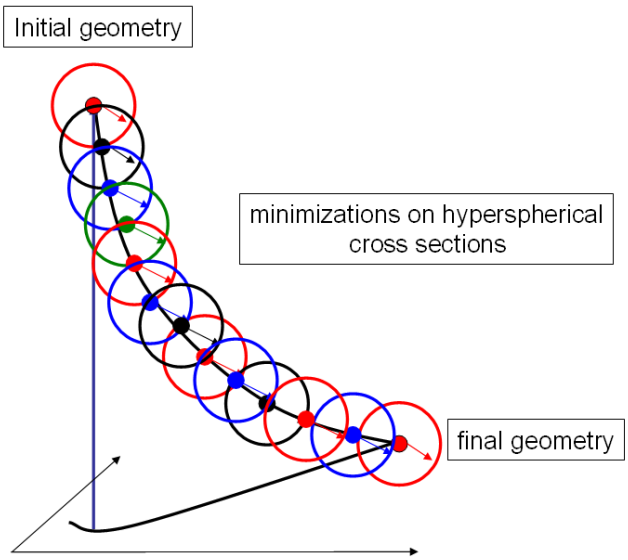

Figure 3.1: Pictorial representation of the MEP technique.

To perform a MEP calculation is then necessary to dispose of an efficient algorithm able to execute a constrained geometry optimization, as the location of a minimum on a PEHs hyperspherical cross section. In addition to projection methods and penalty functions based methods, constrained geometry optimizations are mainly divide in two classes: the ones based on a variation of the Lagrange multiplier method

and the so-called direct approaches. In 1997 the work of Anglada and Bofill [22] shown the relation between these two major types of methods, and suggested a new algorithm able to combine the advantage of space subdivision, as suggested by the direct approach, with a conventional minimization in combination with a Broyden- Fletcher-Goldfarb-Shanno Hessian update procedure (BFGS).

The constrained geometry optimization method employed nowadays to perform MEP calculation is a further modification of the strategy presented by Anglada and Bofill, in which their algorithm is used in combination with the restricted step Rational Function optimization. It was designed and implemented by De Vico, Olivucci and Lindh in 2005 [23], who illustrated its efficiency through for the 1,2-dioxetane system.

3.3 References

[1] Szabo, A.; Ostlund, N. S. *Modern Quantum Chemistry*; Dover Publications: Mineola, New York, USA, 1996.

[2] Helgaker, T.; Jørgensen, P.; Olsen, J. *Molecular Electronic-Structure Theory*; John Wiley & Sons: Chichester, UK, 2000.

[3] Roothaan, C.C.J. *Rev. Mod. Phys.* **1951**, *23*, 69.

[4] Hall, G.G. *Proc. Roy. Soc. Lond.* **1951**, *A205*, 541.

[5] Pulay, P. *Chem. Phys. Lett.* **1980**, *73*, 393.

[6] Almlöf, J.; Frægri, K.; Korsell, Jr; Korsell, K. *J. Comput. Chem.* **1982**, *3*, 385.

[7] Olsen, J.; Jørgensen, P.; Simons, *J. Chem. Phys. Lett.* **1990** *169*, 463.

[8] Roos, B. O. *Chem. Phys. Lett.* **1972**, *15*, 153.

[9] Knowles, P. J.; Handy, N. C. *Chem. Phys. Lett.* **1984**, *111*, 315.

[10] Duch, W. *GRMS or Graphical Representation of Model Spaces 1: Basics*, Lecture Notes in Chemistry Vol. 42; Springer-Verlag, 1986.

[11] Roos, B. O.; Taylor, P. R.; Siegbahn, P. E. M. *Chem. Phys.* **1980**, *48*, 157.

[12] Fletcher, R. *Practical Methods of Optimization*; Wiley, 1987.

[13] Simons, J.; Jørgensen, P.; Taylor, H.; Ozment, J. *J. Phys. Chem.* **1983**, *87*, 2745.

[14] Werner, H.-J.; Meyer, W. *J. Chem. Phys.* **1981**, *74*, 5794.

[15] Roos, B. O.; Linse, P.; Siegbahn, P. E.M.; Blomberg, M. R. A. *Chem. Phys.* **1982**, *66*, 197.

[16] Wolinski, K.; Sellers, H. L.; Pulay, P. *Chem. Phys. Lett.* **1987**, *140*, 225.

[17] Wolinski, K.; Pulay, P. *J. Chem. Phys.* **1989**, *90*, 3647.

[18] Andersson, K.; Malmqvist, P.-Å.; Roos, B. O.; Sadlej, A. J.; Wolinski, K. *J. Phys. Chem.* **1990**, *94*, 5483.

[19] Andersson, K.; Malmqvist, P.-Å.; Roos, B. O. *J. Chem. Phys.* **1992**, *96*, 1218.

[20] Widmark, P.-O.; Malmqvist, P.-Å.; Roos, B. O. *Theor. Chem. Acc.* **1990**, *77*, 291.

[21] Pierloot, K.; Dumez, B.; Widmark, P.-O.; Roos, B. O. *Theor. Chem. Acta* **1995**, *90*, 87.

[22] Anglada, J. M.; Bofill, J. M. *J. Comput. Chem.* **1997**, *18*, 992.

[23] De Vico, L.; Olivucci, M.; Lindh, R. *J. Chem. Theory Comput.* **2005**, *1*, 1029.

Chapter 4

Results

4.1 Basic aromatic biological chromophores

4.1.1 1-aminonaphthalene

Before the present research project was undertaken, different experimental data were available for the entitled molecule, briefly summarized in the following lines. As for other amino-substituted aromatic systems, red-shifted emission bands with respect to the original aromatic molecule have been reported for 1-aminonaphthalene (AMN). Its fluorescence spectrum is in fact composed by sharp transitions and an unstructured red-shifted background [1,2]. The presence of two different emission signals recorded for 1-aminonaphthalene made possible to conclude that the system has dual fluorescence [2]. Regarding the electronic transition properties, the lowest-energy excited states $^1(L_b\,\pi\pi^*)$ and $^1(L_a\,\pi\pi^*)$, present in both 1-aminonphatalene and naphthalene, seem to have a reversal energy ordering in the two molecules [1]. Fluorescence emission is not the only possible decay process operating in the system. An internal conversion process to the ground state was also

detected in different solvents, whose efficiency decreases as the polarity of the environment increases [3]. Comparing the internal conversion process rate for a series of 1-aminonaphthalene derivatives, a correlation was found between the efficiency of the IC process and the twist angle of the amino group relative to the naphthalene plane. It was observed that the molecules having larger twist angles in the minimum of the ground state are in general characterized by a more efficient internal conversion process [3].

The study has been performed by using the well-tested method CASPT2//CASSCF [4,6-12] as implemented in the MOLCAS 6 software [16-18]. Optimized structures and minimum energy paths (MEPs) have been then calculated at the multiconfigurational CASSCF level, and at the geometries so-obtained, the dynamic electron correlation effects have been taken into account by performing second-order multiconfigurational CASPT2 calculations. MEPs have been built as steepest descent paths in which each step requires the minimization of the energy on a hyperspherical cross section of the potential energy hypersurface (PEH) centered on the initial geometry and characterized by a predefined radius [5]. In some cases, at the computed CASSCF crossings, CASPT2 explorations at close geometries were performed in order to find minimum-energy CASPT2 crossing points (MECP), related to conical intersections (CIs), at the highest level of calculation [13-15]. All computations have been performed by imposing no restrictions to the symmetry of the molecule; out-of-plane geometry distortions were therefore allowed. The basis set of atomic natural orbital ANO-S contracted to C,N[3s,2p,1d]/H[2s1p] has been employed. The active space comprises twelve π active orbitals and eleven active electrons [CASSCF(12,11)]. For the CASPT2 calculations, an imaginary level-shift correction of 0.1 au has been used in order to avoid the pres-

ence of intruder states [8]. The CASPT2 standard zeroth-order Hamiltonian has been used as originally implemented [4]. The core orbitals have been frozen in the CASPT2 calculations. From the calculated CASSCF transition dipole moments (TDM) and the CASPT2 band origin energies, the radiative lifetimes have been estimated by the Strickler-Berg relationship [19,20].

Table 4.1: Computed spectroscopic properties of the low-lying singlet excited states of 1-aminonaphthalene.

	vertical absorption/eV		band origin/eV		vertical emission/eV				
state	CAS	PT2(*f*)[a]	CAS	PT2	CAS	PT2	μ/D[b]	Θ_{TDM}[c]	τ_{rad}/ns[d]
$^1(\pi\pi^*)$-L_b	4.15	3.80(0.0008)[e]	3.86	3.50	3.66	3.44	1.36	-15	2754
$^1(\pi\pi^*)$-L_a	5.78	4.35(0.0481)[e]	4.95	3.69[f]	4.27	3.20[g]	4.59	77	64[h]
$^3(\pi\pi^*)$-L_a	2.92	2.83	2.47	2.35	2.06	2.09	1.33		0.1 ms
$^3(\pi\pi^*)$-L_b	4.19	3.63					1.43		

[a] CAS, CASSCF level; PT2, CASPT2 level. Oscillator strengths within parentheses. [b] CASSCF dipole moment at the FC geometry. Ground-state μ is computed to be 1.20 D. [c] Transition dipole moment orientation (Θ_{TDM}), in degrees, referred to the inertial long axis (a) of the molecule, computed here at the optimized FC geometry. For definition see ref. 1. [d] Calculated radiative lifetime (Strickler-Berg relationship). [e] Experimental data (magnetic circular dichroism): band maxima, 3.90 and 4.17 eV (gap 2200 cm^{-1}), in hexane (ref. 3). [f] Laser-induced fluorescence (LIF) in a supersonic jet. Band origin (T_0): 3.73 eV (30045 cm^{-1}), short-axis polarized [1,2]. The computed result corresponds to T_e (ZPE, zero point energy, has not been included). The presence of an overlapping second absorption band with long-axis polarized components (L_b) is suggested [2]. [g] Fluorescence band maximum: 3.31, 2.93, and 2.73 eV in cyclohexane, acetonitrile, and water, respectively (refs. 34 and

35). [h] Estimated radiative lifetime: 13 ns (cyclohexane), 25 ns (butan-1-ol), and 43 ns (water) [35].

Table 4.2: CASPT2 relative energies (E/eV) at the different stationary points of the hypersurfaces referred to the ground state computed at the equilibrium geometry, dipole moments, and CASSCF computed transition dipole moment directions (Θ_{TDM}/deg)[a].

	$(S_0)_{min}$			$(S_1\text{-}L_b)_{min}$			$(S_1\text{-}L_a)_{min}$		
state	ΔE/ev	μ/D	Θ_{TDM}	ΔE/ev	μ/D	Θ_{TDM}	ΔE/ev	μ/D	Θ_{TDM}
S_0	0.00	1.20		0.06	1.21		0.49	1.48	
$^1(\pi\pi^*)$-L_b	3.80	1.36	-15	3.50(Te)	1.29	28	3.92	1.52	-1
$^1(\pi\pi^*)$-L_a	4.35	4.59	77	3.92	4.59	-84	3.69(Te)	5.54	73[b]
$^3(\pi\pi^*)$-L_a	2.83	1.33		2.54	1.33		2.51	1.72	
$^3(\pi\pi^*)$-L_b	3.63	1.43		3.40	1.40		3.88	1.82	

[a] Θ_{TDM} referred as positive toward the amino group from the inertial long axis (a) of the molecule (ref. 1). [b] Transition dipole moment orientation (Θ_{TDM}) of the T_0 band of 1-aminonaphthalene in a supersonic jet: 72°, short (b) axis polarized, that is, L_a type [1].

Tables 4.1 and 4.2 and Figures 4.1 and 4.2 summarize the most relevant theoretical results of the low-lying singlet and triplet electronic states of 1-aminonaphthalene. Two singlet and two triplet excited states (labeled L_a and L_b in Platt's nomenclature) with $\pi\pi^*$ nature have been found as the low-lying excited electronic states, that is, those having photophysical relevance in the excitation region studied. As discussed below, states of pure $n\pi^*$-type character (involving the nitrogen lone-pair electrons) are found energetically too high, although charge transfer from the amino group toward the rings will be shown to play an important role. Tables 4.1 and 4.2 contain results for the computed vertical absorptions, band origins, and vertical emissions for the different states, together with other properties such as transition oscillator strengths, dipole moments, transition dipole moment directions, and radiative lifetimes. Those results are complemented with values of the relative posi-

tion of the states and the transition dipole moments orientation, θ_{TDM}, at the singlet states minima. Together with these properties, Figure 4.1 displays a MEP computed at the CASPT2//CASSCF level on the ^1L_a hypersurface starting at the FC ground-state optimized geometry, which freely leads to the ^1L_a minimum in a barrierless pathway. Along the relaxation process, a crossing between the ^1L_a and the ^1L_b states takes place, the latter state becoming the lowest in energy. Such crossing can be related to the presence of a CI $(^1L_a/^1L_b)_{CI}$, which may, in principle, control the population transfer occurring along the state switch. As discussed below, the theoretical results are complemented with the calculation of the $(^1L_a/S_0)_{CI}$ CI, obtained as the crossing between the two PEHs. Figure 4.2 displays the structures of the singular points optimized in the present work.

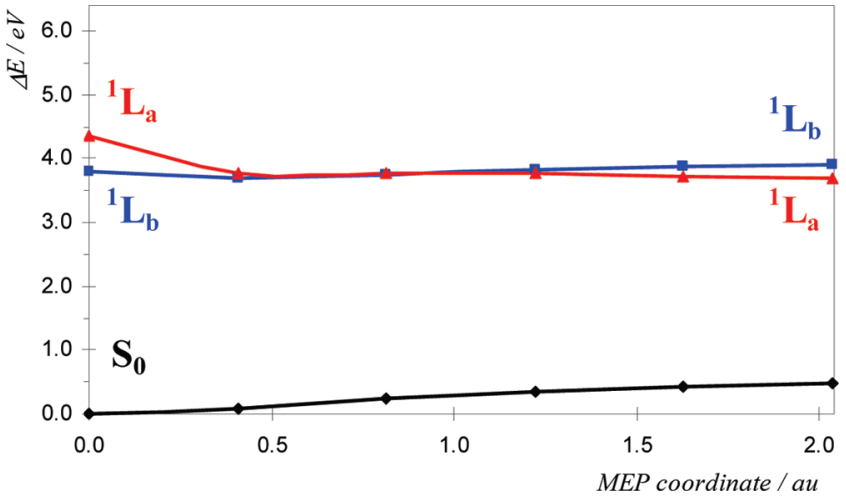

Figure 4.1: Computed CASPT2//CASSCF MEP along the hypersurface starting at the FC geometry (S_0 minimum) and freely leading to the ^1L_a state minimum. A crossing between ^1L_a and ^1L_b hypersurfaces is noticed.

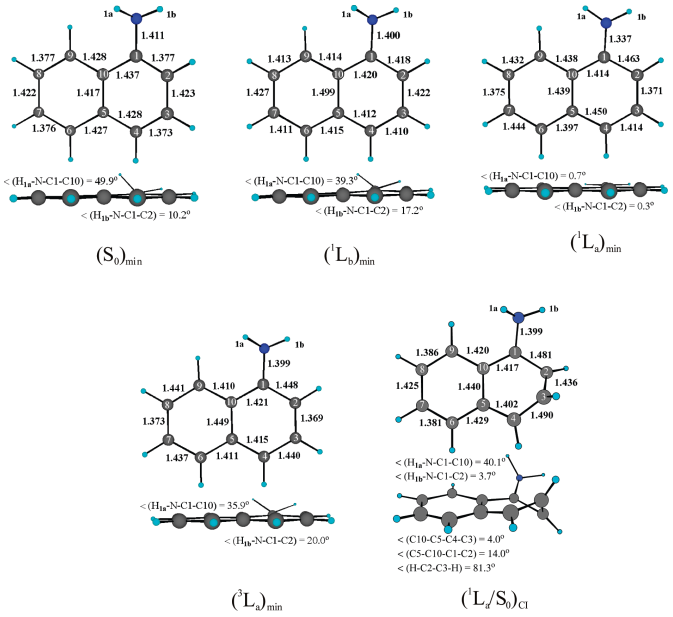

Figure 4.2: Main geometrical parameters of several optimized structures of AMN.

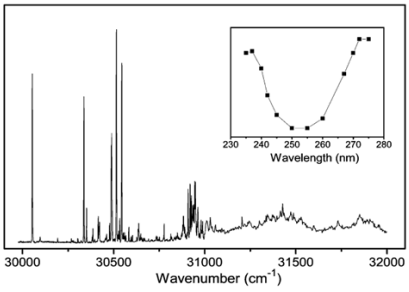

Figure 4.3: Fluorescence excitation spectrum of jet-cooled AMN. The inset shows the total ion signal intensity corrected as a function of the broad-band excitation wavelength.

Several theoretical predictions and experimental evidences point to ^1L_a as the state populated upon excitation in the range of the employed energies, 330-267 nm. Firstly, the results compiled in Table 4.1 predict a substantially higher oscillator strength for the transition to ^1L_a than for that to ^1L_b. Secondly, the transition at 333.8 nm (3.71 eV) of the jet-cooled spectrum has been unambiguously assigned as the $^1L_a \leftarrow S_0$ band origin, having short-axis (b) polarization with a Θ_{TDM} angle of 72°,[1] in perfect accordance with our computed value at the ^1L_a state minimum, 73°. In addition, individual vibronic features of the fluorescent excitation spectrum (Figure 4.3) show lifetimes compatible with the allowed $^1L_a \leftarrow S_0$ transition [21]. Therefore, the remaining question is whether it is possible or not to excite the ^1L_b state from S_0 and what is the spectroscopic signature of this state. Although substitution on naphthalene position 1 by an amino group was thought to cause a state order reversal [1,2,22-24], our findings compiled in Tables 4.1 and 4.2 clearly indicate that the ^1L_b band origin should lie below that of ^1L_a in AMN (3.50 and 3.69 eV, respectively). Since no other spectroscopic feature was found to the red of the ^1L_a state origin, we believe that, although probably the vibrationless ^1L_b transition is too weak to be noticed, some vibronic features of this state may gain intensity from Herzberg-Teller coupling with ^1L_a and appear mixed in the latter state spectrum. A similar situation has been recently found for the $^1L_a/^1L_b$ state mixing in tryptamine [25]. Therefore, below the $^1L_a/^1L_b$ CI calculated to be 0.08 eV over the ^1L_a surface minimum, the spectrum would be composed mainly of $^1L_a \leftarrow S_0$ vibronic bands. Some weak absorption lines of the ^1L_b state owing their intensity to Herzberg-Teller coupling with the ^1L_a state could also appear in this region. About 800 cm^{-1} to the blue of the $^1L_a \leftarrow S_0$ band origin, where the calculations predict the CI to be placed, the spectrum starts to show symptoms of congestion,

reflecting the stronger mixing of both states. At the ground-state optimized FC geometry, the molecule has been shown to be almost planar, with a pyramidalized and partially twisted NH_2 group and out-of-plane dihedral angles of 49.9° and 10.2° (with respect to the carbon in cis position) for the hydrogen atoms 1a and 1b , respectively (cf. Figure 4.2). The nonequivalence of the amino hydrogen atoms, known as peri effect, is caused by a difference in the steric interactions with the adjacent hydrogen atoms of the naphthalene ring [1]. Relaxing the populated ^1L_a state along the computed MEP leads to a crossing between the PEHs of the ^1L_a and ^1L_b states, in which they exchange order, finally reaching the ^1L_a state minima. Such structure belongs to the S_1 PEH and has a totally planar conformation, with a shortened (0.074 Å) C-N bond length and changed bond alternation in the rings with respect to the ground-state minimum, in agreement with the experimental results [1]. Therefore, those deformations will be correlated with the modes responsible for the evolution along the lowest-energy path. The PEH crossing found along the ^1L_a state relaxation path may be related here to the presence of a CI $(^1L_a/^1L_b)_{CI}$ connecting both states. Calculations at the CASPT2 level predict this surface crossing to be at 3.77 (30405 cm^{-1}), 0.27, and 0.08 eV above the ^1L_b and ^1L_a states origin bands, respectively. The ^1L_b state is known as a locally excited (LE) state and has an optimized structure similar to the ground state and also a twisted and pyramidalized amino group with dihedral angles of 39.9° and 8.8°. Regarding the dipole moments of the ^1L_b and ^1L_a states, they are computed to be 1.36 and 4.59 D, respectively. The latter value is 3.8 times that of the ground state (1.20 D), confirming the partial charge-transfer character of the ^1L_a state. Figure 4.4 displays a scheme of the photophysics of AMN based on the combined theoretical and experimental research carried out.

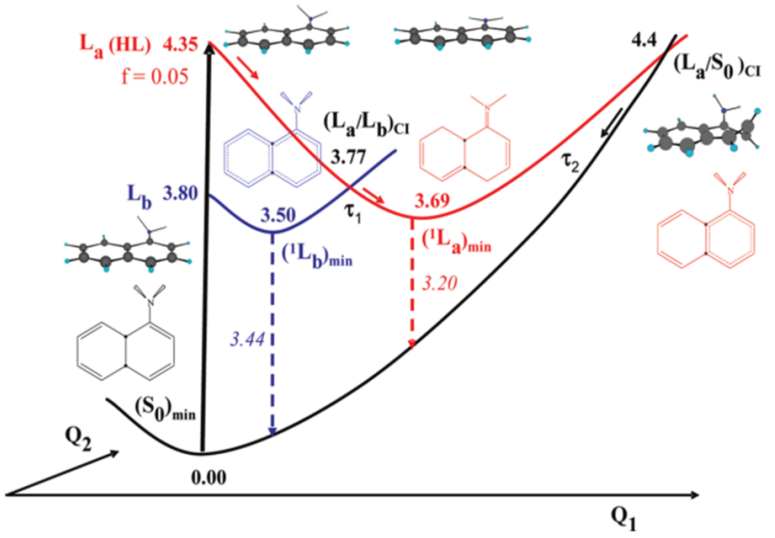

Figure 4.4: 1-aminonaphthalene photophysics scheme based on the corresponding theoretical and experimental findings. Energies are given in electronvolts with respect to the ground-state minimum.

Time-dependent measurements after excitation in the 330-267 nm range (Figure 4.5) were performed aiming to gain information on the $^1L_a/^1L_b$ coupling predicted by the calculations. The only time constant extracted from those measurements is τ_0 = 0-10 fs. This constant appears in the transients collected in the whole interval of excitation energies. Below 31000 cm^{-1} (322.6 nm), the spectral width of the individual vibronic features observed in the LIF (laser-induced fluorescence) excitation spectrum is not compatible with lifetimes shorter than 2 ps, precluding the assignation of τ_0 to an electronic dephasing event. Therefore, τ_0 could have two alternative origins: motion of the wavepacket out of the FC region favored by a resonance that occurs in the absorption

of the probe or a nonresonant ionization contribution.

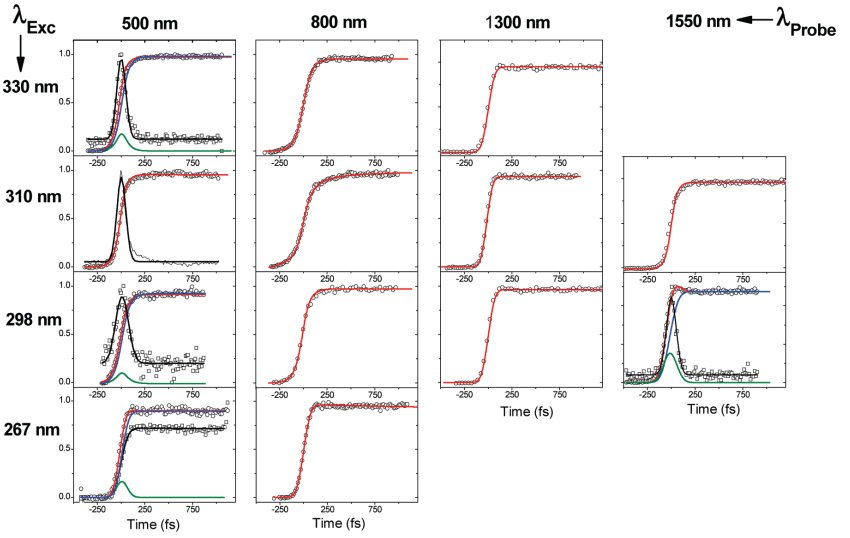

Figure 4.5: Short-range decays of AMN collected at the indicated pump (rows) and probe (columns) wavelengths. Experimental data are shown as circles and decay fits by lines. In those cases where more than a $\tau = \infty$ constant was required in the fitting, the individual components are plotted. The nonresonant ionization signal of ethylene is shown for the sake of comparison except for the 267 nm excitation wavelength. In this case, due to the weak ethylene signal obtained, aniline resonant ionization through a nanoseconds lifetime intermediate state was employed to determine $t = 0$.

A key question requiring further discussion is the absence of the predicted $^1L_a/^1L_b$ coupling signature from the recorded decays. Taking the theoretical calculations as a benchmark, several scenarios could be invoked to explain this fact. (i) An obvious interpretation is the insensitivity of the experiment to the $^1L_a/^1L_b$ surface crossing dynamics. Nu-

merous examples can be found in the literature supporting the ability of the transient ionization technique to reflect the conversion of electronic to vibrational energy. 1-aminonaphthalene represents a complicated situation due to the small energy gap predicted between the band origins of the involved electronic states, merely 1532 cm^{-1} (cf. Tables 4.1 and 4.2). However, the use of a resonant probe and anisotropy measurements aid to overcome this difficulty. It is unlikely that in the event of a $^1L_a/^1L_b$ surface crossing the transition probability to the resonant intermediate state remains constant. Furthermore, the anisotropy decays should reflect the change in the transition dipole moment associated to an eventual surface hoping, as observed in naphthalene [39].(ii) An alternative explanation could be that the excitation populates both states with a ratio close to the one that the system will reach at the CI branching. Although, in principle, the ^1L_a has much higher oscillator strength, some ^1L_b vibronic transitions can gain intensity through Herzberg-Teller coupling, as pointed above. (iii) Finally, the absence of surface crossing signs can also be attributed to the properties of the wavepacket dynamics at the CI. The branching ratio, determined along the coupling coordinate by the wavepacket momentum and the PEH slopes, could favor that the system stays mainly on the initially prepared ^1L_a surface. Calculations able to model the CI topology are required in order to elucidate the plausibility of this scenario.

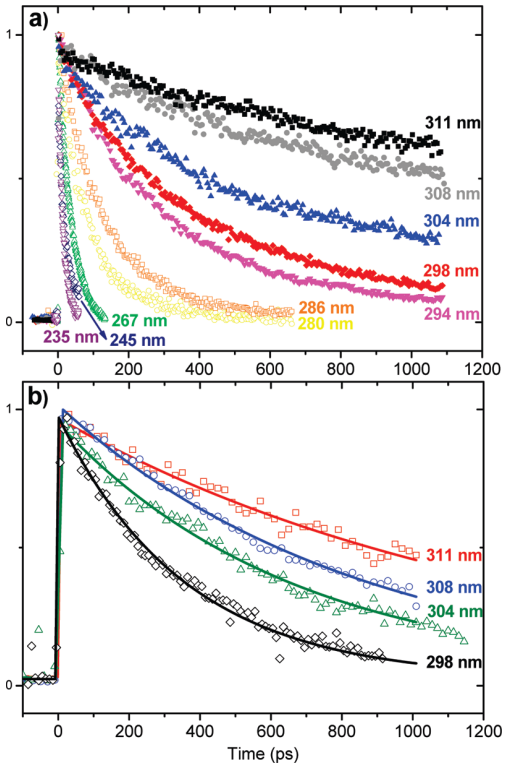

Figure 4.6: (a) AMN long-range decays recorded by exciting at the indicated wavelengths and probing with 800 (a) and 500 nm (b) wavelengths. For the former only the experimental data are shown, whereas for the latter the exponential fittings are also included. The time constants extracted for both probe wavelengths are collected in Table 4.3.

Table 4.3: Lifetimes extracted from the fittings of the long-range AMN transients shown in Figure 4.6[a].

	τ_2 (ps)	
excitation (nm)	probe 800 nm	probe 500 nm
311	940 ± 138	1300 ± 200
308	710 ± 100	772 ± 105
304	513 ± 70	657 ± 60
298	348 ± 30	365 ± 25
294	290 ± 35	
286	120 ± 10	
280	84 ± 6	
267	35 ± 5	
245	16 ± 2	
235	14 ± 2	

[a] The τ_2 constants are the sum of internal conversion and intersystem crossing lifetimes.

The slow component τ_2 observed in the time evolution of the AMN ion is attributed to the system relaxation to the ground-state through the $(^1L_a/S_0)_{CI}$ CI, mixed at low excitation energies with an ISC process. As mentioned above, probing with 500 nm light (Figure 4.6b) does not ionize the triplet state, and thus, the constant background observed in the transients of Figure 4.6a disappears. Assuming an equal ionization probability at 800 nm for the initially populated singlet ^1L_a state and the triplet state, we can relate in our kinetic model the offset to the observed time constant and then separate the contributions of IC and ISC to τ_2. These results are collected in Table 4.3. The lifetimes are in agreement with those reported by Rückert et al. for 1-aminonaphthalene in n-hexane [3]. The data of Table 4.3 show a significant increment in the IC rate with the excitation energy from 0.85 ns at 311 nm (3.99

eV) to 14 ps at 235 nm (5.28 eV). The steep raise is interpreted as the opening of the relaxation channel through the $^1L_a/S_0$ intersection when the excitation energy is enough to overcome the barrier toward $(^1L_a/S_0)_{CI}$, leading to an enhanced IC that competes with the ^1L_a fluorescent emission. The CASPT2 calculations place this intersection 0.7 eV above the ^1L_a state minimum and 4.4 eV above S_0. According to its structure, this crossing is characterized as a typical ethene-like CI, [26-28] in which a twisting of the carbon-carbon double bond leads to an out-of-plane deformation placing one hydrogen above and other below the plane of the ring (cf. Figure 4.2) forming a dihedral angle of 81.3° combined with a slight pyramidalization of the amino group.

The existence of the internal conversion pathway related to a CI $(^1L_a/S_0)_{CI}$ was predicted by Rückert et al. [3] from the study of AMN radiative rates in solution. They determined for 1-aminonaphthalene in n-hexane an IC activation energy of 38 ± 8 kJ/mol (3176 cm^{-1}, 0.39 eV). Although our experimental measurements do not seem to anticipate a clear barrier, the CASPT2 calculations yield an upper bound of 0.7 eV for the crossing of the two surfaces in the isolated AMN with respect to the initially populated ^1L_a minimum. A full CASPT2 optimization of the CI would probably decrease the energy required to reach the PEH crossing closer to the experimental estimations.

The relaxation of AMN was also investigated following excitation to a higher-lying singlet state at 235 nm (5.28 eV). Two states are computed higher than ^1L_b and ^1L_a at the FC geometry, namely, S_3 and S_4, with 4.98 and 5.18 eV energies, 1.79 and 2.28 D dipole moments, and 0.0052 and 0.0528 $S_0 \leftarrow S_{3,4}$ oscillator strengths, respectively. The higher oscillator strength of S_4 permits us to assign it as the responsible of the absorption at 235 nm observed in the inset of Figure 4.3. The transients recorded following excitation of this band (Figure 4.7)

show a biexponential behavior with the components: $\tau_1 = 80 \pm 10$ fs and $\tau_2 = 14 \pm 2$ ps. The electronic relaxation pathway is understood in a sequential way, where the prepared S_4 state relaxes to the lower $S_3/^1L_a/^1L_b$ manifold (mediated by CIs), proceeding from there to the ground state through the calculated $(^1L_a/S_0)_{CI}$.

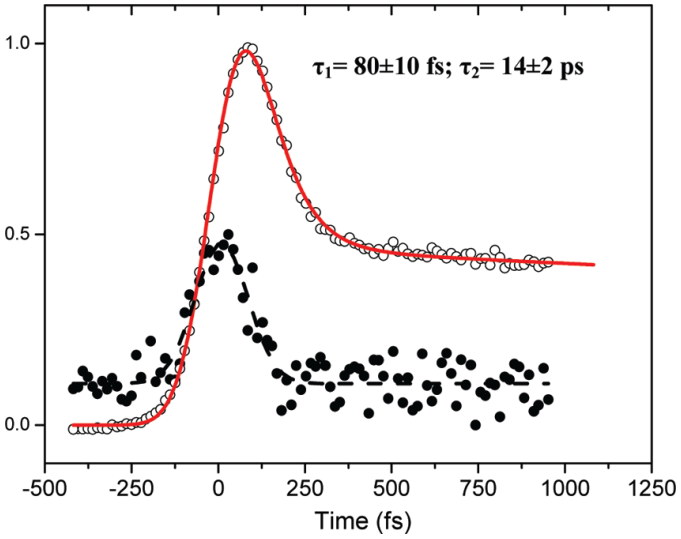

Figure 4.7: Short time scale transient of AMN collected with 235 nm excitation and 800 nm probe wavelengths. The dashed line corresponds to the 1 + 4 nonresonant ionization signal of ethylene. Experimental data are shown as circles and decay fittings by lines.

On the light of the experimental and theoretical results presented, we may try to interpret previous results on the photophysics of AMN. The lack of experimental evidence of the $^1L_a/^1L_b$ surface crossing does not allow us to validate the dual-fluorescence model proposed for AMN

[2]. Within this model, the red-shifted emission, which is observed in addition to the sharp features when the zero-point level is excited, is interpreted as the emission of a charge-transfer character state (^1L_a in this case) different from the locally excited ^1L_b. In our picture, ^1L_a would be the initially prepared state and the broad red-shifted emission a consequence of its geometry change with respect to the ground state.

Concerning the photophysics of the system in solvated environments, the increase of solvent polarity is related to the raise of fluorescence quantum yields (θ_f) and lifetimes (τ_f): $\theta_f = 0.47$, $\tau_f = 6.63$ ns (hexane), $\theta_f = 0.66$, $\tau_f = 12.4$ ns (diethylether), and $\theta_f = 0.86$, $\tau_f = 18.3$ ns (acetonitrile) and a decrease of the IC quantum yields from 0.13 (hexane) to 0.04 (acetonitrile) [3]. This behavior was previously explained by the reduction of the $S_2 - S_1$ gap in nonpolar solvents that rules the vibronic coupling between the excited states [3]. A stronger coupling between both states was then expected to favor the decay to the ground state, decreasing in that case the barrier for the IC from the S_1 to the S_0 state. As recently emphasized, [13] the use of the energy gap between excited states as a measure of the strength of the vibronic coupling controlling the efficiency of the IC to the ground state may not be a valid argument related to the classical and frequently used Lim's proximity effect model [13,29]. The model is not applicable in many cases, and AMN is a good example of its failure. In fact, its initial hypothesis is erroneous. Contrary to previous proposals, which suspected a state reversal with respect to naphthalene, [3] the highly polar ^1L_a state is S_2 at the FC geometry, and as shown in Table 4.2, in polar solvents a large stabilization of the ^1L_a (S_2) state with respect to the ^1L_b (S_1) and the ground state can then be expected, diminishing the $S_2 - S_1$ and $S_2 - S_0$ energy gap and, thus, invalidating the initial hypothesis and the model. The analysis of the dipole moments of the states compiled

in Table 4.2 provides valuable insight into the expected trends in polar media. Similarly, for the ground and the ^1L_b states low dipole moments have been computed at the FC geometry, 1.20 and 1.36 D, respectively, close to the experimental determination for the ground state, 1.55 D [3]. On the contrary, the ^1L_a state dipole moment is computed to be 4.57 D, a somehow small value if compared with the 7.2 D estimated using Onsager's solvatochromic shift procedure, [3] although this is a strategy with limited accuracy that tends to overestimate the excited-state dipole moments [30,31]. In any case the partial charge-transfer character of the ^1L_a state is confirmed. Figure 4.8 displays a density difference plot between the ground and the exited ^1L_a state at the ^1L_a minimum structure, in which the charge-transfer character of the excited state is enhanced. Excitation to the ^1L_a state is accompanied by a shift of the amino nitrogen and the substituted benzene charge toward the neighbor ring, resulting in a large, mainly long-axis polarized, dipole moment. The corresponding charge transfer is largely favored by the coplanarity of the amino group. The alternative model we highlight here points out that the efficiency of any IC is related to the location and properties of the nearby CIs $(^1L_a/S_0)_{CI}$ and with the barriers required to access the seam of the CI, and not to the gaps between higher excited states, S_1-S_2 $(^1L_b - ^1L_a)$, the location of the corresponding CI, $(^1L_a/^1L_b)_{CI}$, or the vibronic coupling between these two states. As a matter of fact, the S_2 state lies in AMN higher than 2 eV at the $(^1L_a/S_0)_{CI}$ structure, and it can hardly have any influence in the position or shape of the CI. Therefore, we may state that the IC process related to the nanosecond-range lifetime of AMN in solvated phases is modulated only by the location and the barrier to access the $(^1L_a/S_0)_{CI}$, which is the actual funnel controlling the decay. The increase of the barrier in polar solvents, and thus the loss of the efficiency of the IC to the ground state, correlates

with the relative difference of polarity of the ^1L_a state at its minimum, with a computed dipole moment of 5.54 D, and at the $(^1L_a/S_0)_{CI}$ structure, 1.20 D. The barrier to access the CI will be larger in polar solvents, due to the stabilization of the ^1L_a minimum with respect to the CI. The theoretical prediction can be compared with the experiment: the AMN fluorescence maxima originated at the ^1L_a minimum varies from 3.29 (hexane) to 2.96 eV (acetonitrile), [3] pointing to a stabilization of the $(^1L_a)_{min}$ minimum when the solvent polarity is increased.

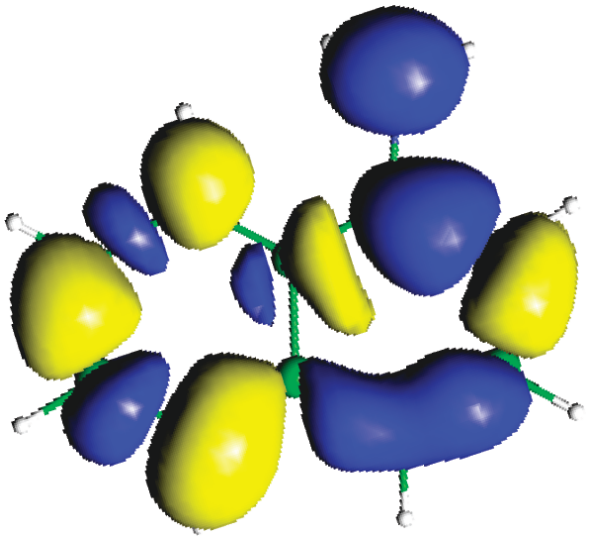

Figure 4.8: Density difference plot of the ^1L_a state of AMN with respect to the ground state at the ^1L_a minimum structure (isovalue 0.001). In the excitation the charge leaves the blue (dark) zones toward the yellow (light) areas, explaining the short-axis polarization of the corresponding transition, the long-axis polarized and large dipole moment of the excited state, and its partial charge-transfer character (from the amino group to the rings).

As showed above, the theoretical results and the experimental data available in the literature and produced in the present work determine a harmonious picture of different photophysical processes characterizing 1-aminonaphthalene, while others features (as the plausible internal conversion process between the ^1L_a and ^1L_b states) are uncoupled. It remains to clarify if such a fact is due to the failure of the theoretical description or of the experimental detections.

Finally, it is significant to compare the obtained results regarding 1-aminonaphthalene with the known data on naphthalene [32-39]. In both cases the lowest singlet excited states are the ^1L_b and ^1L_a. These states in 1-aminonaphthalene appear at lower energy, although the energy gap between them at the Franck-Condon (FC) region is similar in both molecules (around 0.5 eV). The break of the D_{2h} symmetry due to the introduction of the amino group determines a non-zero value of the dipole moments. Such a fact in turn causes that the bright state of 1-aminonaphthalene is much more influenced by solvent polarity, since its dipole moment is much higher than the ones characterizing the ^1L_b and ground states. In the two molecules the ^1L_a state is the bright state. Interestingly, an internal conversion process from the bright ^1L_a to the ^1L_b state has been experimentally detected for naphthalene, while the same transfer, although here theoretically predicted, has not been experimentally observed for 1-aminonaphthalene. As pointed out above, the fluorescent spectrum of 1-aminonaphthalne presents red-shifted bands with respect to naphthalene.

4.1.2 Indole, the main emissive source of proteins

At the beginning of the research project many different theoretical and experimental works were available, [1-24] rationalizing various photo-

physical properties of indole. The main findings and conclusions obtained in those works are introduced in the following. As in many other polycyclic aromatic systems, the $^1(L_a\,\pi\pi^*)$ and $^1(L_b\,\pi\pi^*)$ states were identified to be the main responsible for its photophysics. The corresponding absorption peaks and band origins were experimentally determined, and the related theoretical values obtained. Particularly challenging was the experimental determination of the $^1(L_a\,\pi\pi^*)$ band origin, since it is hampered by the extensive vibronic structure that characterized the $^1(L_b\,\pi\pi^*)$ transition. The environment dependent Stokes shift in the fluorescence spectrum that characterizes indole and that makes possible the analysis of its fluorescence response in order to determine the conformation of tryptophan-containing proteins (see the Introduction chapter), was explained on the basis of an environment dependent inversion in the energy order of the $^1(L_a\,\pi\pi^*)$ and $^1(L_b\,\pi\pi^*)$ states [21,22]. The phenomenon was shown to be due to both the little energy separation between such states, and the higher dipole moment inherent to the $^1(L_a\,\pi\pi^*)$ state with respect to the $^1(L_b\,\pi\pi^*)$. The abruptly decrease of the fluorescence quantum yield with the increase of the excitation energy [11] was justified by a mechanism involving a Rydberg state localized on the NH bond, which can decay to the original ground state through a CI. It was shown that such state can be populated from both lowest-lying excited $\pi\pi^*$ states overcoming an energy barrier, and consequently it accounts for the excitation energy dependence of the fluorescence quantum yield [20,23,24]. Finally, a CI between the $^1(L_a\,\pi\pi^*)$ and $^1(L_b\,\pi\pi^*)$ states was recently reported, which can mediate a population transfer between these states [17,18].

Despite the large amount of studies on indole photophysics and the quite complete photophysical view that emerges from them, an unconstrained exploration of the PEH of indole following the principles of the

photochemical reaction path approach was not performed. As has been described in the second chapter of the thesis, such strategy constitutes the most appropriate way to describe the photophysics and photochemistry of a molecular system. In most of the past theoretical works the geometry of indole was in fact constrained to planarity [21,22]. Moreover, standard optimization procedures were used, which are unable to determine the presence or absence of energy barriers from the starting to the optimized geometry, and are consequently unsuited to map the MEP followed by excited indole [20,23,24]. With the present research we have undertaken a totally unconstrained state-of-the-art study of the main photophysical processes that take place in indole after excitation in the low-energy UV range.

The study has been performed by using the well-tested methodology CASPT2//CASSCF [30-33] as implemented in the MOLCAS 7.4 software [34]. Optimized structures and MEPs have been then calculated at the multiconfigurational CASSCF level, and at the geometries so obtained the dynamic correlation effects have been taken into account in the energies by performing second-order multiconfigurational CASPT2 calculations. All computations have been performed by imposing no restrictions to the symmetry of the molecule; out-of-plane geometry distortions were therefore allowed. Two basis sets of atomic natural orbital (ANO) of S- and L-type contracted to C,N [4s,3p,1d]/H[2s1p] and C,N [4s,3p,1d]/H[2s1p], respectively, have been employed leading to similar conclusions. The results reported here correspond to the higher level of theory, that is, employing the ANO-L basis set. The whole π system of the molecule has been considered in the active space. Thus, it comprises six π orbitals of the benzene ring plus two π orbitals of the pyrrole ring and the π orbital of the nitrogen atom, together with the corresponding ten electrons [CASSCF(10,9)]. For the CASPT2 calculations, an imag-

inary level-shift correction of 0.2 au has been used in order to avoid the presence of intruder states. The CASPT2 standard zeroth-order Hamiltonian has been used as originally implemented [31]. The core orbitals have been frozen in the CASPT2 calculations. Such CASPT2 approach has been validated during the last decades in many different studies on organic molecules providing a correct description and interpretation of the photophysical experimental data [35,36]. The research of the evolution of the valence excited states has been performed by means of MEP calculations.[26,27] Mass-weighted coordinates have been used. This technique provides (if present) a steepest descent path, in which each step is built by the minimization of the energy on a hyperspherical cross section of the PEH centered on the initial geometry within a predefined radius. The importance and reliability of results obtained using such a computational tool have been proven in many different studies which confirm MEP calculations as a valuable procedure for the description of the photophysics and photochemistry of a molecule [37,38]. CIs not obtained along MEPs calculations have been computed by using the restricted Lagrange multipliers technique, as included in the MOLCAS 7.4 package, in which the lowest-energy point is obtained under the restriction of degeneracy between the two considered states [34].

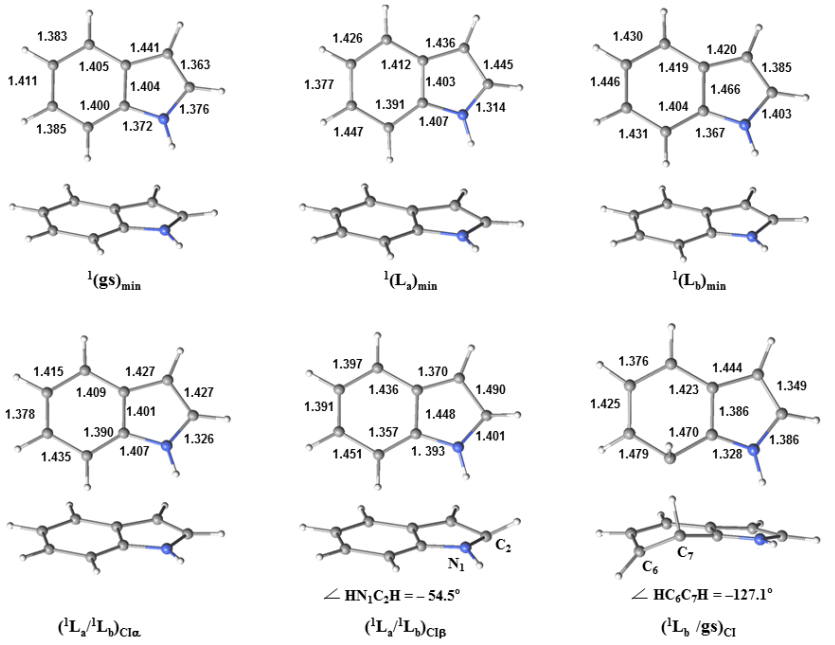

Figure 4.9: Frontal and side views of the CASSCF optimized structures of indole. CC and CN bond lengths (in Å) are also shown.

Optimization of the ground state of indole with a totally unconstrained approach leads to a planar geometry, labeled $^1(gs)_{min}$. The frontal and side views of this structure are depicted in Figure 4.9. At the geometry of this minimum, $^1(gs)_{min}$, a vertical CASPT2//CASSCF calculation of the low-lying six singlet excited states has been undertaken in order to study the absorption properties of the molecule in the FC region. For the sake of completeness, the lowest triplet excited states have also been computed. Only valence excited states have been considered since the present study is focused on the photophysics of indole, which is mainly determined by the valence electronic structure of

the molecule. Analysis of non-pure valence excited states has been provided elsewhere [19,20,23,24]. The two lowest excited states, which will be those studied in the present work, have been determined to be valence states. Analysis of the orbitals involved in the excitations related to these low-lying valence excited states has been carried out here to establish their nature. According to the Platt's nomenclature, [25] the valence states of interest can be described in terms of the Natural Orbitals (NOs) topologically equivalent to the Highest Occupied Molecular Orbital (HOMO) and Lowest Unoccupied Molecular Orbital (LUMO). Thus, the CASSCF wave function basically described by the minus linear combination of the HOMO (H) $\rightarrow$ LUMO (L) +1 (25%) and H -1 $\rightarrow$ L (47%) configurations is identified as the $^1(L_b\,\pi\pi^*)$ state, while the CASSCF wave function mainly composed by the H $\rightarrow$ L (56%) one-electron promotion is recognized as the $^1(L_a\,\pi\pi^*)$ state. The computed CASPT2 energies show that the $^1(L_b\,\pi\pi^*)$ and $^1(L_a\,\pi\pi^*)$ states are the lowest $\pi\pi^*$ valence singlet excited states, placed vertically (E_{VA}) at 4.36 eV and 4.79 eV, respectively (see Table 4.4). The results are in agreement with the available experimental data [1,2,4,6]. Table 4.5 compiles in addition the computed oscillator strengths (f) and dipole moments (μ) for the $^1(L_b\,\pi\pi^*)$ and $^1(L_a\,\pi\pi^*)$ states. According to the results, the latter is predicted to be the bright state upon UV irradiation. The calculated dipole moment, μ, at the FC region is also consistent with the experimental findings [8-10]. The $^1(L_b\,\pi\pi^*)$ state has a low μ (1.55 D), similar to the value obtained for the ground state (1.81 D), while $^1(L_a\,\pi\pi^*)$ is characterized by a high μ (6.07 D), which is more than three times larger with respect to the former.

Table 4.4: Calculated and experimental energy (in eV) for the low-lying excited valence states of the isolated indole molecule.

	theory			experiments		
state	E_{VA}[a]	T_e[a]	E_{VE}[a]	A_{max}[b]	T_0[b]	R.emib
$^1(L_b\ \pi\pi^*)$	4.36	4.11	4.01	4.37	4.37	4.12[e]/4.36
$^1(L_a\ \pi\pi^*)$	4.79	4.40	4.07	4.77	4.54	
$^3(L_a\ \pi\pi^*)$	3.42	3.01	2.68	3.3[f]	3.07[f]	2.87[f]
$^3(L_b\ \pi\pi^*)$	4.05	3.83	3.66			

[a] ANO-L type basis set C,N [4s,3p,1d]/H[2s1p], CASPT2//CASSCF-(10,9) vertical excitation energy (E_{VA}), electronic band origin (T_e), and vertical emission energy (E_{VE}). [b] Measured absorption band maximum (A_{max}), band origin (T_0), and relaxed emission from the excited-state relaxed geometry (R. emi). [c] Experimental data from refs. 1, 2, 4, and 6. [d] Estimated excitation energy from the ground state minimum (see ref. 19). [e] Experiments from ref. 14. [f] Experimental spectra from refs. 15 and 16.

Table 4.5: Calculated vertical excitation energies at the FC geometry (E_{VA}, eV) for the lowest valence singlet and spin forbidden triplet excited states[a].

root	state	E_{VA}	f	μ
S_0	gs			1.81
T_1	$^3(L_a\,\pi\pi^*)$	3.42		1.41
T_2	$^3(L_b\,\pi\pi^*)$	4.05		1.76
S_1	$^1(L_b\,\pi\pi^*)$	4.36	0.018	1.55
T_3	$^3(B_a\,\pi\pi^*)$	4.50		1.83
T_4	$^3(\pi\pi^*)$	4.74		1.46
T_5	$^3(B_b\,\pi\pi^*)$	4.76		5.08
S_2	$^1(L_a\,\pi\pi^*)$	4.79	0.078	6.07

[a] The computed dipole moments (μ, D) and the oscillator strengths (f) for the singlet-singlet transitions are also included.

Rydberg states are not described here, and for this reason, the basis set employed in our calculations does not include the required Rydberg-type functions to treat properly such states. Some calibration computations have been performed by locating at the center of mass Rydberg basis functions, which have been built specifically for the indole molecule. The results obtained ensure an accurate description of the $^1(L_b\,\pi\pi^*)$ and $^1(L_a\,\pi\pi^*)$ states by means of the basis set without diffuse functions. In addition, the work carried out by Serrano-Andrés and Roos [19] on the theoretical study of the absorption spectrum of indole proved that the lowest Rydberg state appears vertically at 4.85 eV with respect to the

ground state energy, and our calculations show that the $^1(L_b\,\pi\pi^*)$ and $^1(L_a\,\pi\pi^*)$ singlet excited states have vertical electronic transitions lower than 5.00 eV. Consequently, only the evolution of these two low-lying singlet valence excited states is next analyzed.

Regarding triplet excited states, five low-lying computed roots present E_{VA} values lower than 5.00 eV, and therefore these states have been taken into account in the photochemical description of the system. As for the singlet excited states, the nature of the triplet states has been identified by inspection of the respective CASSCF wave functions and each of them has been labeled by using Platt's nomenclature [25]. The overall results for the triplet states, together with those related to the singlet $^1(L_b\,\pi\pi^*)$ and $^1(L_a\,\pi\pi^*)$ states, are summarized in Table 4.5. In contrast to the singlet states, the $^3(L_a\,\pi\pi^*)$ has a lower E_{VA} than $^3(L_b\,\pi\pi^*)$ and both of them have dipole moment similar to that of the value obtained for the ground state.

By analyzing the oscillator strengths it is possible to assert that most of the molecules reach the $^1(L_a\,\pi\pi^*)$ state after UV irradiation [the calculated f of the $^1(L_b\,\pi\pi^*)$ and $^1(L_a\,\pi\pi^*)$ states are 0.018 and 0.078, respectively]. From the FC geometry, evolution of the initially populated $^1(L_a\,\pi\pi^*)$ state has been characterized by means of the MEP approach with no spatial symmetry constrains. The computational result is a barrierless path leading directly from the FC region to a CI involving the $^1(L_b\,\pi\pi^*)$ and $^1(L_a\,\pi\pi^*)$ states, placed at 4.42 eV with respect to the ground-state minimum, denoted hereafter as $(^1L_a/^1L_b)_{CI\alpha}$ (see Figure 4.10). Such degenerate region is a converged point on the obtained MEP and it is not the lowest-energy point of the crossing seam but the first funnel that can be reached by the excited molecule and consequently the most photophysical relevant crossing point [40]. This CI has been characterized recently by Brand et al. [17,18] with an upper

bound of around 4.6 eV at the DFT/MRCI level. An efficient internal conversion (IC) process mediated by this CI consequently causes energy transfer from $^1(L_a\,\pi\pi^*)$ to $^1(L_b\,\pi\pi^*)$ state. Actually, almost all the MEP points are characterized by a quite pronounced energy degeneracy between the $^1(L_b\,\pi\pi^*)$ and $^1(L_a\,\pi\pi^*)$ states, which suggests that along the decay pathway from the FC region, the probability of populating the $^1(L_b\,\pi\pi^*)$ state is high. The equilibrium structure itself of the $^1(L_a\,\pi\pi^*)$ state, obtained as the last point of the MEP calculation, hereafter $^1(L_a)_{min}$, is placed at only 0.12 eV below the $^1(L_b\,\pi\pi^*)$ state and it is almost degenerate with the $(^1L_a/^1L_b)_{CI\alpha}$ point, which mediates the ultrafast relaxation to the $^1(L_b\,\pi\pi^*)$ state. According to these findings, the $^1(L_a)_{min}$ structure, with a computed vertical emission ($E_{\rm VE}$) of 4.07 eV (see Table 4.4), is not expected to contribute significantly to the fluorescence phenomenon in the indole molecule. This is in contrast with the initial evidence of dual fluorescence in both polar and nonpolar solvents, based on measurements of the polarization of the fluorescence bands, [41] and supports further experimental findings suggesting that while two different states seem to contribute in the lowest-energy absorption band, only one of them is responsible for the emission [42]. Figure 4.11 displays the results obtained for the MEP from $(^1L_a/^1L_b)_{CI\alpha}$. As can be seen in the picture, the $^1(L_b\,\pi\pi^*)$ state evolves through a steepest descent path to the equilibrium geometry, $^1(L_b)_{min}$. Similar results are obtained by carrying out a MEP from the $^1(L_a)_{min}$ structure. At the $^1(L_b)_{min}$ geometry, the singlet excited state $^1(L_b\,\pi\pi^*)$ is the lowest on the S_1 hypersurface, and since the system cannot further evolve in a radiationless manner, we conclude that it is from this region that the emission takes place. For the S_1 state, the computed $E_{\rm VA}$, the electronic band origin (T_e), and $E_{\rm VE}$ are 4.36, 4.11, and 4.01 eV, respectively (see Table 4.4). The present results agree within 0.26 eV with those ob-

tained by Serrano-Andrés and Roos [19], being particularly closer to the experimental data reported by Borisevich et al. [14] than to other initial observations [4]. In general, all the theoretical and experimental studies yield lower E_{VA}, T_e, and E_{VE} values for $^1(L_b\,\pi\pi^*)$ with respect to the $^1(L_a\,\pi\pi^*)$ state.

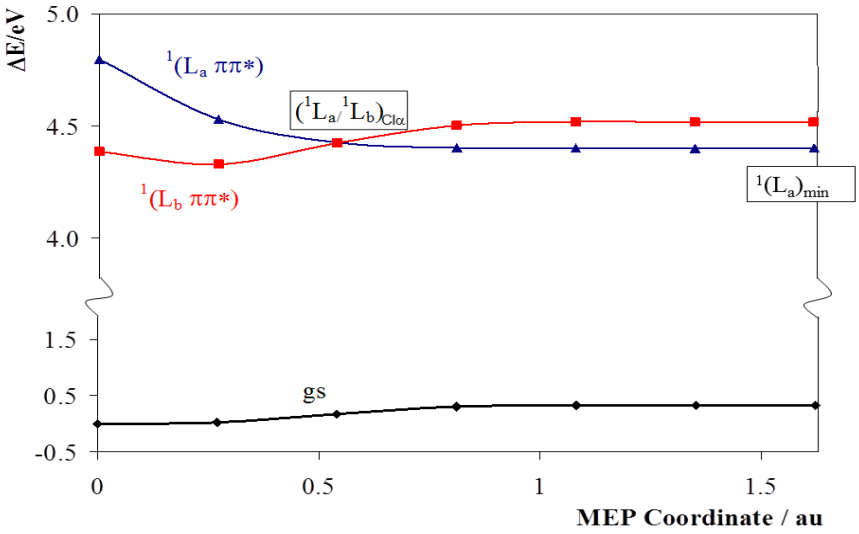

Figure 4.10: Evolution of the ground and two lowest singlet excited states for indole from the FC geometry along the $^1(L_a\,\pi\pi^*)$ MEP computed at the CASPT2//CASSCF(10,9)/ANO-L C,N [4s,3p,1d]/H[2s1p] level.

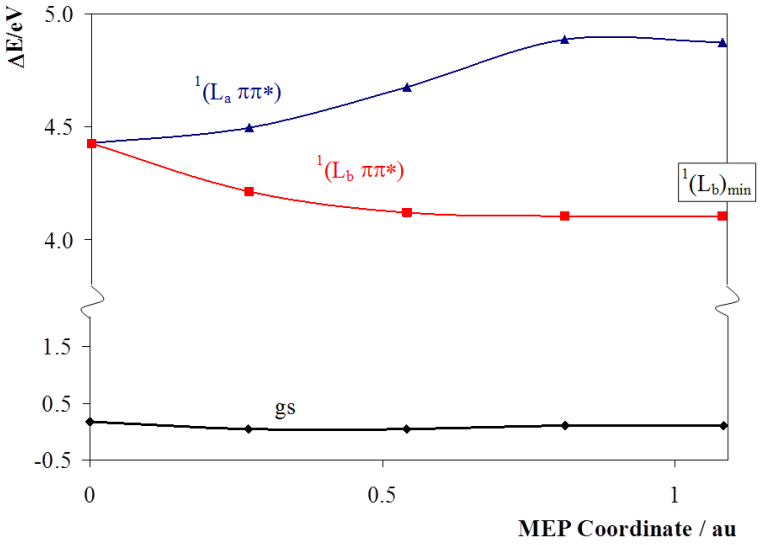

Figure 4.11: Evolution of the ground and two lowest singlet excited states for indole from the $(^1L_a/^1L_b)_{CI\alpha}$ conical intersection along the $^1(L_b\,\pi\pi^*)$ MEP computed at the CASPT2//CASSCF(10,9)/ ANO-L C,N [4s,3p,1d]/H[2s1p] level.

In the previous section the main decay path on the photophysics of indole has been characterized, i.e., the primary process that follows the population of the brightest excited state upon light irradiation. To improve the description, two other relevant deactivation paths have been studied, and are next analyzed. The first one is based on the fact that the $^1(L_b\,\pi\pi^*)$ singlet state can also be initially populated by UV absorption, since the computed f for the electronic transition is not negligible. In order to study such possibility, the MEP on the $^1(L_b\,\pi\pi^*)$ singlet state has been built starting from the FC structure (see Figures 4.12a). The final point of the MEP corresponds to the same region previously found

along the main decay path: the $^1(L_b)_{min}$ structure. This new evidence confirms the relevant participation of the equilibrium structure of the $^1(L_b\,\pi\pi^*)$ state, $^1(L_b)_{min}$, in the fluorescence phenomenon of indole.

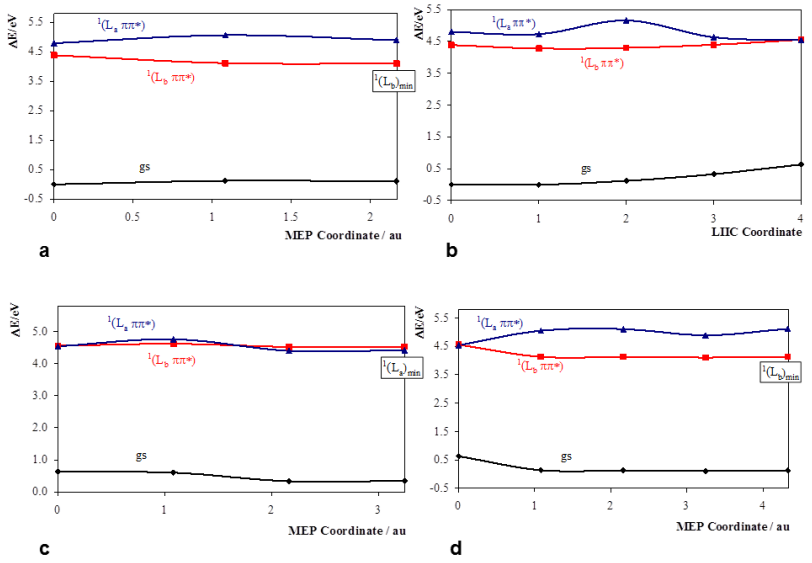

Figure 4.12: Energy profiles of the ground and two lowest singlet excited states for indole along the additional decay paths computed at the CASPT2//CASSCF(10,9)/ANO-L C,N [4s,3p,1d]/H[2s1p] level. (a) $^1(L_b\,\pi\pi^*)$ MEP from the FC geometry, $^1(gs)_{min}$, (b) LIIC between $^1(gs)_{min}$ and $(^1L_a/^1L_b)_{CI\beta}$, (c) $^1(L_a\,\pi\pi^*)$ MEP from $(^1L_a/^1L_b)_{CI\beta}$, and (d) $^1(L_b\,\pi\pi^*)$ MEP from $(^1L_a/^1L_b)_{CI\beta}$.

The second possible deactivation path studied involves an alternative CI between the $^1(L_a\,\pi\pi^*)$ and $^1(L_b\,\pi\pi^*)$ states, which will be denoted as $(^1L_a/^1L_b)_{CI\beta}$. This CI region might be important in the photophysics of indole since its energy with respect to the ground-state minimum is

equal to 4.54 eV, which is only 0.12 eV above the CI, $(^1L_a/^1L_b)_{CI\alpha}$. The new structure, $(^1L_a/^1L_b)_{CI\beta}$, is therefore placed in a region of the PEH energetically close to the main decay path that the system is expected to undertake upon absorption of UV light. As shown in Figure 4.9, $(^1L_a/^1L_b)_{CI\beta}$, in contrast to $(^1L_a/^1L_b)_{CI\alpha}$, is characterized by a pronounced out-of-plane distortion mainly localized on the HN_1 and C_2H groups; the dihedral angle related to the corresponding planes is equal to -54.5°. In order to establish the accessibility of this region, which would give us a hint on the relevance of the CI for the photophysics of the system, a linear interpolation of internal coordinates (LIIC) calculation has been performed on both the $^1(L_a\,\pi\pi^*)$ and the $^1(L_b\,\pi\pi^*)$ states between the FC and $(^1L_a/^1L_b)_{CI\beta}$ structures (see Figure 4.12b). Such type of calculation is able to provide a connected path between two regions of the PEH, along with the corresponding (if present) barrier, which constitutes an upper bound to the energy required to reach the final geometry from the starting one. The so-computed energy barriers along the $^1(L_a\,\pi\pi^*)$ and$^1(L_b\,\pi\pi^*)$ manifolds from the FC region to the $(^1L_a/^1L_b)_{CI\beta}$ geometry are 0.43 eV and 0.26 eV, respectively. These values show that the $(^1L_a/^1L_b)_{CI\beta}$ region might be accessible after UV-irradiation at least from the $^1(L_b\,\pi\pi^*)$ state. An energy barrier of 0.1–0.2 eV is in fact normally considered a small barrier to be easily overcome, although only dynamics studies of the system can actually provide such conclusion. According to the suggested plausible accessibility of the $(^1L_a/^1L_b)_{CI\beta}$ region upon UV irradiation, the evolution of the system from this CI has been also studied to give a complete description of the photophysics of bare indole. A MEP calculation shows that the $^1(L_a\,\pi\pi^*)$ state will evolve from the $(^1L_a/^1L_b)_{CI\beta}$ region to the previously characterized $^1(L_a)_{min}$ structure (see Figure 4.12c). Although the path on the $^1(L_a\,\pi\pi^*)$ PEH connecting the structures has been ob-

tained through the use of the MEP technique at the CASSCF level, the correction introduced in energies by means of the CASPT2 computations yields a small barrier of 0.22 eV. This result further points out to the importance of taking into account the correlation effects associated with the instantaneous short-range electron-electron interaction in order to give a correct description of excited state PEHs. Due to the low value of the barrier obtained at the CASPT2 level, we conclude that the $^1(L_a\,\pi\pi^*)$ state will decay to the $^1(L_a)_{min}$ structure, from which, as previously stated, the system might evolve to the $^1(L_b)_{min}$ equilibrium geometry. For the sake of completeness, from the $(^1L_a/^1L_b)_{CI\beta}$, point the behavior of the $^1(L_b\,\pi\pi^*)$ state has also been studied by means of computing the corresponding MEP (Figure 4.12d). The evolution of the $^1(L_b\,\pi\pi^*)$ state from the $(^1L_a/^1L_b)_{CI\beta}$ region leads to an equilibrium geometry which belongs again to the region on the PEH of S_1 previously identified as the responsible for the fluorescence produced by the system: the $^1(L_b)_{min}$ emissive structure. In summary, all the secondary photophysical events analyzed, derived from the population of the $^1(L_b\,\pi\pi^*)$ state at the FC region or from the $(^1L_a/^1L_b)_{CI\beta}$ structure, drive the system toward the equilibrium region on the S_1 PEH, $^1(L_b)_{min}$, which is assigned to the fluorescent feature observed in bare indole.

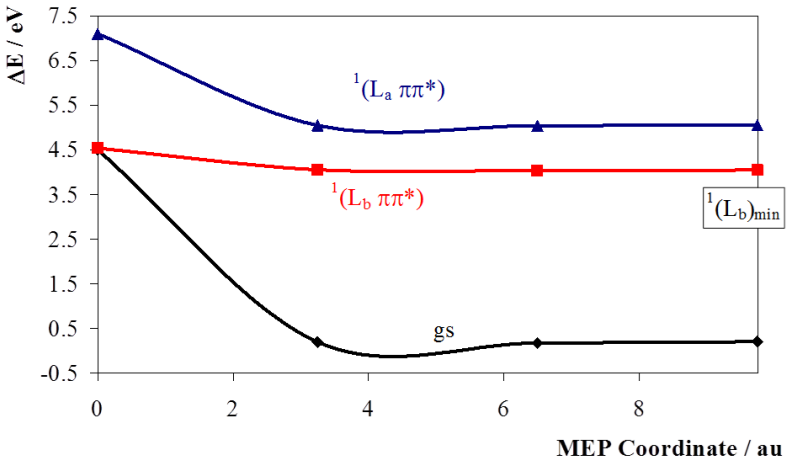

Figure 4.13: Evolution of the ground and the two lowest singlet excited states for indole from the $(^1L_b/gs)_{CI}$ conical intersection along the $^1(L_b\,\pi\pi^*)$ MEP computed at the CASPT2//CASSCF(10,9)/ANO-L C,N [4s,3p,1d]/H[2s1p] level.

We have shown that the photophysics of indole is characterized by different decay paths leading to the $^1(L_b)_{min}$ equilibrium structure, from which the molecule is predicted to emit light. Nevertheless, the intensity of the fluorescence band has been observed in several experiments to be sensitive to the excitation energy and the experimental conditions. In particular, the fluorescence quantum yield of bare indole drastically decreases as the excitation energy provided to the system increases [11]. The loss of fluorescence emission in bare indole was previously explained by Sobolewski, Domcke, and co-workers [20,23,24] who showed that the presence of a dark $\pi\sigma^*$ state could be the responsible of a non-radiative

decay mechanism. According to their results, in order to activate such radiationless process, the initially populated $^1(L_a\,\pi\pi^*)$ state has to reach a CI with the $\pi\sigma^*$ state which is placed above 5.00 eV with respect to the ground-state minimum. The authors then concluded that such barrier could explain the decrease of the fluorescence quantum yield of the system as the excitation energy is increased, and predicted a threshold for this photophysical process to be located at about 5 eV for excitation from the minimum of the ground state. This mechanism is consistent with the increase of the non-radiative decay rate measured for indole with respect to N-methylindole [11]. However, it does not account for other experimental observations. The emission quantum yield of indole after excitation to the $^1(L_a\,\pi\pi^*)$ state at 257.2 nm (4.81 eV) is equal to 0.103, [11] which is too low in comparison to the band intensity observed when excitation energies corresponding to the $^1(L_b\,\pi\pi^*)$ band origin are employed or to the present computation results [4]. In fact, Ilich concluded in the experimental work on the low-lying singlet states of indole that the system has remarkable emission features only for energies around the $^1(L_b\,\pi\pi^*)$ band origin (measured at 4.37 eV), whereas a 22-fold decrease is observed when the molecule is provided with an extra energy of 4200 cm^{-1} (0.52 eV) [4]. Such experimental observations seem to point out to the presence of a non-radiative decay path accessible for excitation energies lower that 5.00 eV related to the $^1(L_b\,\pi\pi^*)$ state, apart from the radiationless route characterized by Sobolewski, Domcke, and co-workers [20,23,24]. Consistent with these experimental findings, we have found a CI between $^1(L_b\,\pi\pi^*)$ and the ground state, denoted hereafter as $(^1L_b/gs)_{CI}$. This degenerate region is placed at 4.50 eV with respect to $^1(gs)_{min}$ and is characterized by a strong out-of-plane distortion, mainly localized on the C_6H and C_7H group of atoms (see Figure 4.9). It can be in fact better classified as a typical ethene-

like CI [28,29,36], in which a twist of the double bond between the C_6 and C_7 atoms leads to an out-of-plane deformation with a HC_6C_7H dihedral angle of -127.1^o and a pyramidalization of the C_7 atom. In order to determine the relevance of this CI on the photophysics of indole, a MEP on the S_1 state has been computed from the $(^1L_b/gs)_{CI}$ region (see Figure 4.13). This calculation shows the presence of a barrierless path leading to the $^1(L_b)_{min}$ region, which proves that $(^1L_b/gs)_{CI}$ can be reached from the equilibrium geometry of the $^1(L_b\,\pi\pi^*)$ state by overcoming a barrier of 0.39 eV. Such process consequently constitutes a non-radiative decay path specific for the $^1(L_b\,\pi\pi^*)$ state, whose accessibility depends on the energy provided to the system and can be activated at excitation energies lower than 5.00 eV. Figure 4.14 displays a scheme of the main decay paths after population of the $^1(L_a\,\pi\pi^*)$ and $^1(L_b\,\pi\pi^*)$ states at the FC region, together with the radiationless path mediated by $(^1L_b/gs)_{CI}$. The relative position of the latter CI with respect to the other singular points depicted in the figure supports the decrease of the measured fluorescence quantum yield with the increase of the excitation energy. After population of the bright $^1(L_a\,\pi\pi^*)$ state at the FC structure, the system has enough energy ($\sim$0.3 eV) to activate the non-radiative process via $(^1L_b/gs)_{CI}$, which is in agreement with the relatively low fluorescence quantum yield observed by Glasser and Lami [14]. If the indole molecule is irradiated with a light energy similar to the $^1(L_b\,\pi\pi^*)$ band origin, the $^1(L_b)_{min}$ region may be directly populated and the system will need an extra energy of 0.40 eV to access the $(^1L_b/gs)_{CI}$ funnel to the ground state. Therefore, the fluorescence from the $^1(L_b)_{min}$ will be the predominant process taking place. The non-radiative energy decay to the ground state will begin to compete with the emission of light as the irradiation energy approaches the $^1(L_a\,\pi\pi^*)$ vertical excitation energy, which is located 0.29 eV above the $(^1L_b/gs)_{CI}$

structure. On the basis of our results, we associate therefore the non-radiative process observed at energies below 5.00 eV to be determined mainly by the above described path from the $^1(L_b)_{min}$ minimum structure to the ground state via the $(^1L_b/gs)_{CI}$, which implies a threshold for the photophysical process around 0.5 eV lower with respect to the mechanism proposed by Sobolewski, Domcke, and co-workers [20,23,24] and does not involve a dissociative $\pi\sigma^*$ state. It is worth mentioning however that the last energy-decay route is still present in some extent, as it has been shown in some experiments in which the NH bond dissociation is observed, [12,13] and it might also contribute at excitation energies lower that 5.00 eV via tunneling effects. In order to determine to what extent this dissociative deactivation path competes with the new mechanism obtained, and, in particular, to ultimately understand the respective contribution of both energy-decay paths to the photophysics of the system depending on the excited state populated and on the exceeding energy provided, a dynamics study on bare indole would be necessary. Up to now only on-the-fly semiclassical dynamics simulations based on time-dependent density functional theory (TDDFT) starting on the S_2 state have been performed [45]. In such work, some trajectories computed using the PBE functional actually decay through the $\pi\sigma^*$ state, giving a low quantum yield for the dissociation along the NH coordinate. Nevertheless, according to the authors results and comments, the PBE functional is not able to provide the correct ordering of the $^1(L_a\,\pi\pi^*)$ and $^1(L_b\,\pi\pi^*)$ states, and the use of the CAM-B3LYP functional, which on the contrary gives the correct ordering of the low-lying excited states, providing a larger energy gap between the $\pi\pi^*$ and $\pi\sigma^*$ states, decreases the probability of energy decay via the mechanism involving the NH bond stretch.

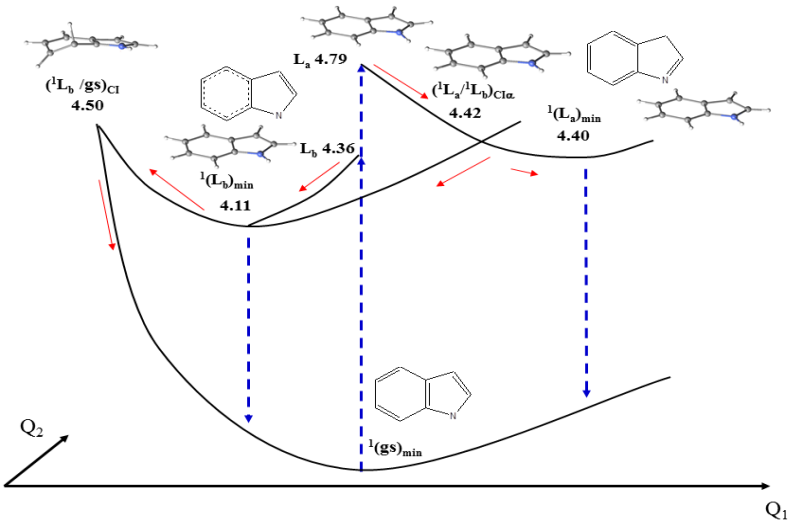

Figure 4.14: Scheme of the photophysics of indole along the singlet manifold. Energies (in eV) relative to the ground-state minimum structure are given. The Q_1 reaction coordinate is mainly related to the single/double-bond rearrangements keeping the planarity of the molecule. Meanwhile, Q_2 is associated to out-of-plane distortions.

Along the evolution of the initially populated $^1(L_a\,\pi\pi^*)$ singlet state, and through the subsequent $^1(L_b\,\pi\pi^*)$ steepest descent path leading to the $^1(L_b)_{min}$ structure, no strongly efficient intersystem crossing regions have been identified. The same result has been obtained from the inspection of the two characterized secondary decay paths. In order to search for the phosphorescent structures related to the low-lying triplet

excited states, $^3(L_a\,\pi\pi^*)$ and $^3(L_b\,\pi\pi^*)$, geometry optimizations of these states have been carried out starting from the FC region. The minima obtained, namely $^3(L_a)_{min}$ and $^3(L_b)_{min}$, respectively, have an almost planar geometry. The computed results, vertical excitation energies, band origins, and vertical emission energies are compiled in Table 4.4, together with the relevant experimental data. The $^3(L_a\,\pi\pi^*)$ state corresponds at the CASPT2 level to the lowest triplet excited state at both the optimized CASSCF $^3(L_a)_{min}$ and $^3(L_b)_{min}$ structures, and consequently the phosphorescence of the system is expected to take place from the $^3(L_a\,\pi\pi^*)$ state. In fact, a single phosphorescence band has been reported starting at 3.07 eV with a maximum at 2.87 eV, [15,16] which is in agreement with previous [19] and present theoretical findings for the $^3(L_a\,\pi\pi^*)$ state (see Table 4.4).

The original contribution of the work has been the unconstrained state-of-the-art description of the photophysics of bare indole on the basis of the principles of the photochemical reaction path approach. Moreover, it has been determined a new non-radiative decay channel that allows to rationalize further the photophysical response of bare indole and adds indole to the group of organic aromatic chromophores in which an ethene-like CI plays a crucial role in the photophysics.

4.2 DNA related chromophores

4.2.1 Thymine-Thymine (6-4) adduct, a DNA photolesion

Previously to our work, different experimental and theoretical studies on pyrimidine photoproducts were published [1-18]. Most of them deal with cyclobutane pyrimidine dimers, [4-11] while only a few debate on

pyrimidine-pyrimidone (6-4) adducts [12-15]. Among the works related to the (6-4) adducts, the main research was aimed to determine the photoactivated repair process, and to the best of our knowledge only four articles debate the formation mechanism of such photolesions [12-15]. In the case of thymine-thymine (6-4) adduct, its mechanism of formation is assumed to take place through a photoactivated step leading to an oxetane structure, and a subsequently thermal process causing the opening and rearrangement of the oxetane cycle into the final product (see Figure 4.15) [1]. The general photoprocess through which a carbonyl and an alkene group form an oxetane structure is called Paternò-Büchi reaction [19]. It is usually considered to take place via the reaction of an excited carbonyl group in its singlet or triplet $n\pi^*$ excited state with a ground state carbon-carbon double bond [20].

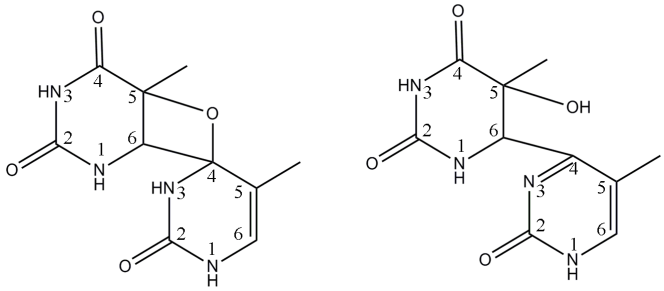

Figure 4.15: Structure of the thymine-thymine (6-4) adduct and its oxetane precursor.

Determination of the photoinduced formation mechanism leading to pyrimidine-pyrimidone (6-4) adducts, and the particular case of two

thymine molecules, is an open field of research. Such a study undoubtedly constitutes a considerable challenge for both experimental and theoretical scientists. Despite its biological importance as DNA photolesion, the thymine-thymine (6-4) adduct is in fact fortunately produced in a very little amount. Consequently, its study entails the determination of what can be regarded as a quite unlikely process. This is in contrast to the main goal pursued in the other works presented in the thesis, which has been the determination of the most probable decay. The photochemical reaction path approach is consequently here of little help, and the main tool for the determination of the present photochemical mechanism has been the assessment through accurate high-level quantum chemical calculations of different plausible hypothesis. It is worth to remark that such situation is not so uncommon in the study of non-adiabatic excited state reactions. It is in fact frequent that the mechanism of reaction passes through characteristic geometries of the PEHs that are not minimum neither saddle points, as for example an accessible CI. In that situations the determination of the most probable path that connect the important regions is a challenging task, since the way to obtain the MEP connecting two general points of a PEH is not well defined. The main guidelines of the research project have been our experience in organic photochemistry, and the available experimental and theoretical results on the studied mechanism, on the Paternò-Büchi reaction, and on the thymine system.

The study has been performed by using the well-tested methodology [21-24] CASPT2//CASSCF as implemented in the MOLCAS 7.4 software [25]. Optimized structures and MEPs have been then calculated at the multiconfigurational CASSCF level, and at the geometries so obtained, dynamic correlation effects have been taken into account by performing second-order multiconfigurational CASPT2 calculations.

All computations have been carried out by imposing no restrictions on the symmetry of the molecule. Basis sets of the atomic natural orbital (ANO) of S-type contracted to C,N,O[3s,2p,1d]/H[2s1p] have been employed [26]. The active space in the CASSCF and CASPT2 calculations is composed of 6 electrons and 6 orbitals for one thymine nucleobase and 12 electrons and 12 orbitals for the dimer system formed by two thymine molecules. For the CASPT2 calculations, an imaginary level-shift correction of 0.2 au has been used in order to avoid the presence of intruder states. The CASPT2 standard zeroth-order Hamiltonian has been employed as originally implemented [22]. The core orbitals have been frozen in the CASPT2 calculations. Such a CASPT2 approach has been validated during the last decades in many different studies on organic molecules, providing a correct prediction, description, and interpretation of the photophysical and photochemical experimental data [27-29]. CIs have been computed by using the restricted Lagrange multipliers technique as included in the MOLCAS 7.4 package in which the lowest-energy point is obtained under the restriction of degeneracy between the two considered states [25]. The basis set superposition error (BSSE) has been taken into account using the counterpoise correction (CP) [30].

It is well recognized that DNA is a very flexible structure. Its conformation at the time of light irradiation has been proven to be of primary importance in determining the way in which the absorbed energy can be released by the system [4,8]. In particular, the degree of stacking and the distance between the nucleobases strongly influence whether the excitation will be localized on a single nucleobase or delocalized among them. In the former, the first process that follows UV irradiation is related to the photophysics of a single nucleobase. According to the present results, it is predicted that (6-4) adduct formation from the stacked

thymine-thymine (TT) system is triggered by a local geometry that allows localization of the excitation on a single thymine molecule, whose photoresponse represents the initial step of the global photoreaction. The minimum reaction path of thymine starting at the ground-state optimized geometry on the brightest $^1(\pi\pi^*)$ singlet excited state, hereafter $(gs)_{mim-thy}$, is barrierless, leading to an ethene-like CI with the ground-state, determining the photostability of thymine [31,32]. Along this main decay path, a singlet-triplet intersystem crossing region has been found, which in the present work is coincident with the $(gs)_{min-thy}$ geometry, hereafter denoted also as $(^1\pi\pi^*/^3n\pi^*)_{STC-thy}$. Thus, part of the population of the bright $^1(\pi\pi^*)$ state might be transferred to the $^3(n\pi^*)$ state, owning also at the significant spin-orbit coupling (SOC) computed at this point (14.5 cm^{-1}). Once the $^3(n\pi^*)$ state is populated, it evolves to a minimum structure, denoted as $^3(n\pi^*)_{min-thy}$ (see Figure 4.16), characterized by an elongated $C_4 = O$ bond (1.354 Å). Such structural condition is a key driver for the global photoreaction, since it causes a partial loss of the double bond character of the $C_4 = O$ bond, and consequently favors the reaction of the carbonyl group with an adjacent carbon-carbon double bond. From the $^3(n\pi^*)_{min-thy}$ region, the presence of a nearby CI between the $^3(n\pi^*)$ and $^3(\pi\pi^*)$ states allows the relaxation of the thymine system to a minimum of the $^3(\pi\pi^*)$ state, which might finally decay to the ground-state by surmounting a small barrier that leads to an intersystem crossing region [32,33]. For a non-highly-stacked TT system, the photophysical response of the bright excited state $^1(\pi\pi^*)$ localized on a single nucleobase is expected to be the same as the one described above for the isolated thymine molecule. Consequently, the TT system should decay via a radiationless process to the ground-state and, in less extent, population of the $^3(n\pi^*)$ state should take place. In order to validate such hypothesis, we have studied the

PEH between the TT system at its B-DNA conformation [$(gs)_{B-DNA}$ hereafter] and the same structure in which one thymine (denoted as T') has been replaced with the excited $^3(n\pi^*)_{min-thy}$ geometry and the other monomer (denoted as T) has been left as in its ground-state conformation (see Figure 4.16). The last geometry will be denoted as $^3(n\pi^*)_{min-TT}$. At the $(gs)_{B-DNA}$ structure, the brightest singlet excited states are indeed localized on the T' and on the T moieties, respectively. As for one thymine, the $(gs)_{min-B-DNA}$ structure constitutes a singlet-triplet crossing region (STC) between the localized $^1(\pi\pi^*)$ and the $^3(n\pi^*)$ states, so it will be also labeled as $(^1\pi\pi^*/^3n\pi^*)_{STC-B-DNA}$. The plausibility of our hypothesis is confirmed by the presence of a barrierless path between the $(gs)_{B-DNA} - (^1\pi\pi^*/^3n\pi^*)_{STC-B-DNA}$ and $^3(n\pi^*)_{min-TT}$ structures and since their energies are comparable to the values for $(gs)_{min-thy}$ and $^3(n\pi^*)_{min-thy}$, respectively (see Table 4.6 and 4.7). The $^3(n\pi^*)_{min-TT}$ is almost degenerate with a CI between the localized $^3(n\pi^*)$ and $^3(\pi\pi^*)$ states, hereafter $(^3n\pi^*/^3\pi\pi^*)_{CI-TT}$ (see Figure 4.16), responsible for the decay to the $^3(\pi\pi^*)$ state. Once in the $(^3n\pi^*/^3\pi\pi^*)_{CI-TT}$ region, the $^1(\pi\pi^*)$ state is clearly far in energy (see Table 4.7), which discard a further evolution of the system on the singlet manifold. The $(^3n\pi^*/^3\pi\pi^*)_{CI-TT}$ structure is connected with an intersystem crossing region $(^3\pi\pi^*/gs)_{STC-TT}$ on the PEH of the $^3(\pi\pi^*)$ state by surmounting a small barrier of 0.20 eV. Along this path, the originally localized excitation that characterizes the $^3(\pi\pi^*)$ state at the $(^3n\pi^*/^3\pi\pi^*)_{CI-TT}$ geometry becomes increasingly delocalized on the adjacent thymine and finally describes a charge-transfer state from the T to the T' nucleobase at the $(^3\pi\pi^*/gs)_{STC-TT}$ structure. The very same excitation characterizing the T_1 state at this intersystem crossing region also describes the $S_1 - ^1(\pi\pi^*)$ state, which is now degenerated with both the ground and the $^3(\pi\pi^*)$ state (see Table 4.7). The $(^3\pi\pi^*/gs)_{STC-TT}$

can be consequently considered a region of triple crossing, involving the S_0, S_1, and T_1 surfaces. A similar CI between the ground and the lowest singlet excited state was previously described by Blancafort and Migani, although a connected path from the absorbed excited state to such CI was not identified [12]. The $(^3\pi\pi^*/gs)_{STC-TT}$ geometry is of paramount importance in the formation mechanism of the thymine-thymine (6-4) adduct, since it is connected through an almost barrierless path with the ground-state of the oxetane (Ox) intermediate, and consequently can funnel the system from the excited state reactant to the ground-state photoproduct. Once the system reaches the $(^3\pi\pi^*/gs)_{STC-TT}$ region, it would finally decay to the oxetane Ox geometry, concluding the photoactivated part of the mechanism that gives rise to the thymine-thymine (6-4) adduct. The highly unstable oxetane intermediate is subsequently converted into the thymine-thymine (6-4) adduct through thermal migration of the 4-exocyclic keto group of T' nucleobase to the C_5 position of T moiety [1]. In the $(^3\pi\pi^*/gs)_{STC-TT}$ structure, the $C_{4'} = O$ bond distance of the T' fragment is equal to 1.345 Å, the $C_5 = C_6$ bond of T is elongated, reaching a bond length of 1.462 Å, and the $O - C_5$ bond present in the oxetane intermediate is almost formed (1.657 Å). The $(^3\pi\pi^*/gs)_{STC-TT}$ has a biradical character with the unpaired electrons located on the C_6, $C_{4'}$ and $C_{6'}$ atoms, similar to the intermediate intersystem crossing regions for the formation of cyclobutane pyrimidine dimers along the triplet manifold [6].

Table 4.6: Energies (eV) of the thymine system at different geometries. They have been calculated at the CASPT2//CASSCF(6,6)/ANO-S C,N,O [3s,2p,1d]/H[2s1p] level with respect to one isolated ground-state thymine.

Geometry	**State**				
	gs	$^1(\pi\pi^*)$	$^1(n\pi^*)$	$^3(\pi\pi^*)$	$^3(n\pi^*)$
$^1(gs)_{min}$	0.00	4.77	4.92	3.75	4.77
$^3(n\pi^*)_{min\ thy}$				3.60	3.93

Table 4.7: Energies (eV) of the thymine-thymine system at different geometries. They have been calculated at the CASPT2+CP-BSSE//CASSCF(12,12)/ANO-S C,N,O [3s,2p,1d]/H[2s1p] level with respect to two isolated ground-state thymine molecules.

Geometry	**State**				
	gs	$^1(\pi\pi^*)$	$^1(n\pi^*)$	$^3(\pi\pi^*)$	$^3(n\pi^*)$
$(gs)_{min\ B\text{-}DNA}$		4.61	4.93		4.71
1 LIIC point		4.83	4.61		4.67
2 LIIC point			4.21		4.26
3 LIIC point			3.89		4.00
$^3(n\pi^*)_{min\ TT}$			3.90		3.91
$(^3n\pi^*/^3\pi\pi^*)_{CI\ TT}$		5.53	3.96	3.96	3.91
1 LIIC point		5.04		3.84	
2 LIIC point		5.15		4.04	
3 LIIC point		4.38		3.94	
$(^3\pi\pi^*/gs)_{STC\ TT}$	3.53	3.56		3.53	
1 LIIC point	3.69				
2 LIIC point	3.22				
3 LIIC point	2.35				
Ox	1.46				

Population of the $^3(n\pi^*)$ state through the $(^1\pi\pi^*/^3n\pi^*)_{STC-B-DNA}$ intersystem crossing region constitutes the starting point of the above description. According to previous studies, an internal conversion process toward the localized $^1(n\pi^*)$ state can also be expected, since for the isolated thymine system an accessible CI between the $^1(\pi\pi^*)$ and $^1(n\pi^*)$ states has been actually described and because the PEHs of singlet and triplet $n\pi^*$ states have been proven to run parallel [32]. In the present study, the energies of the $^1(n\pi^*)$ state along the path connecting the FC and $(^3n\pi^*/^3\pi\pi^*)_{CI-TT}$ regions have been determined. The results show that also for the TT system, the PEHs of the singlet and triplet $n\pi^*$ states are almost coincident (see Table 4.7). On the basis of these results, and for the mentioned reasons, it seems reasonable to expect that the $^1(n\pi^*)$ state might be populated from the $^1(\pi\pi^*)$ state and subsequently evolve to the $^3(n\pi^*)_{min-TT}$ structure. Furthermore, the $(^3n\pi^*/^3\pi\pi^*)_{CI-TT}$ CI represents also a STC between the $^1(n\pi^*)$ and the $^3(\pi\pi^*)$ states (ΔE = 0.02 eV, SOC = 5.2 cm^{-1}), which consequently allows the system in the $^1(n\pi^*)$ state at the $^3(n\pi^*)_{min-thy}$ structure to decay to the $^3(\pi\pi^*)$ state and evolve to the $(^3\pi\pi^*/gs)_{STC-TT}$ geometry. As previously pointed out, the $(^3\pi\pi^*/gs)_{STC-TT}$ singlet-triplet crossing structure from which the system decays to the oxetane geometry represents also a CI between the lowest singlet states. At this point, both the S_1 and T_1 states have a charge-transfer character, mainly described by an excitation from the T to the T' nucleobase. It would consequently be interesting to study the possibility of populating the $(^3\pi\pi^*/gs)_{STC-TT}$ region along the singlet manifold and to analyze the role of the charge-transfer states in the overall photoprocess. According to the above outcomes, through the bright $^1(\pi\pi^*)$ and then the $^1(n\pi^*)$ states it could be possible to reach the $^3(n\pi^*)_{min-thy}$ reactive structure, which constitutes the starting point of the reaction between the two thymine molecules.

From such region, the $^1(n\pi^*)$ state cannot further decay along the singlet manifold, since all other singlet states are far above in energy. We then conclude that the presented mechanism cannot take place entirely along the singlet states. The existence of a different connected path along the singlet manifold that from the brightest states leads to the $(^3\pi\pi^*/gs)_{STC-TT}$ structure has not been computationally found. Blancafort and Migani, who have previously described a similar CI, have correlated such region with a high-lying charge-transfer state described in the B-DNA geometry as the S_5 state [12]. Even if the hypothesis may be considered plausible, still a connected path to the conical region has not been provided. Another point regarding the importance of charge-transfer states in the global photoreaction, also highlighted in ref. 12, is that at the B-DNA geometry they are far above in energy with respect to the brightest states. Consequently, although a connected path along the charge-transfer state could exist, it would remain to clarify how it can be populated from the brightest states.

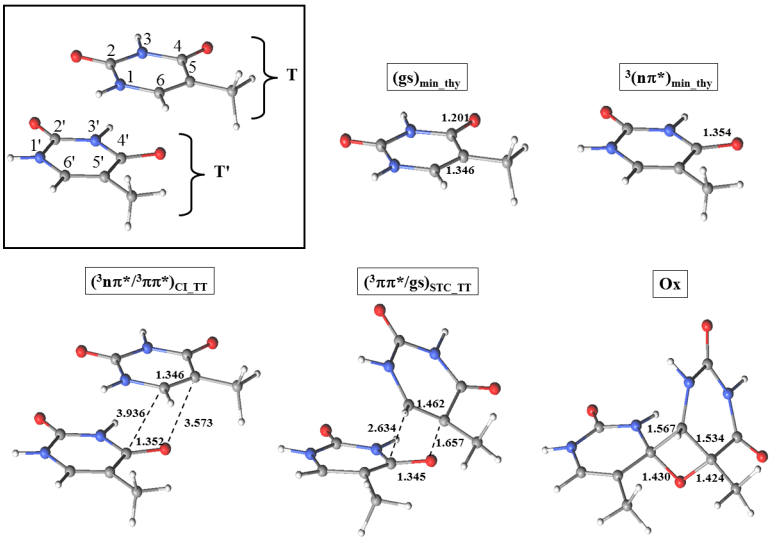

Figure 4.16: Main structures involved in the mechanism for the photoproduction of the oxetane intermediate. Bond lengths are reported in Ångstrom. In the inset, atom and nucleobase labeling are shown.

On the basis of the current results, we can depict the following scheme for the formation mechanism of the oxetane precursor, which can be divided in two main steps (see Figure 4.17). To activate the reaction between the carbonyl group of T' and the carbon-carbon double bond of T, the T' must be in a favorable molecular form. According to our outcomes, this structure is $^3(n\pi^*)_{min-thy}$, which is in fact characterized by a considerable elongation of the carbonyl double bond. In the first step of the global mechanism, the excitation would be localized on just one thymine, corresponding to the population of the $^3(n\pi^*)_{min-thy}$ geometry for the T' nucleobase, which depends on the actual geometry of the system at the time of light irradiation and on the efficiency of the

intersystem crossing process through the $(^1\pi\pi^*/^3n\pi^*)_{STC-thy}$. If the TT system absorbs UV radiation in a conformation characterized by a relatively large separation between the two nucleobases, the excitation could remain localized on a single thymine. Once the $^1(\pi\pi^*)$ state of T' is populated, the efficiency of the global process would be modulated by the effectiveness of the intersystem mechanism to the $^3(n\pi^*)$ state. The second step of the global mechanism is the reaction of the excited T' with T along the suggested pathway from the $^3(n\pi^*)_{min-TT}$ geometry to the oxetane (Ox) structure mediated by the presence of the $(^3n\pi^*/^3\pi\pi^*)_{CI-TT}$ triplet-triplet and the $(^3\pi\pi^*/gs)_{STC-TT}$ singlet-triplet crossings. The efficiency of the second step is determined by the effectiveness of an intersystem crossing mechanism with the ground-state, competing with relaxation processes characterizing the photophysics of a single thymine triplet state [32]. The decay through the intersystem crossing region is consequently an additional limiting factor of the global photoreaction. As previously pointed out, the first described step of the global photoreaction might be mediated by the $^1(n\pi^*)$ state, because the $^3(n\pi^*)_{min-TT}$ reactive structure is expected to be populated also along such state. From this situation, the system can subsequently decay through the second step of the described mechanism since the accessible $(^3n\pi^*/^3\pi\pi^*)_{CI-TT}$ geometry constitutes also a STC between the $^1(n\pi^*)$ and the $^3(\pi\pi^*)$ states. These non-adiabatic relaxation processes toward the $n\pi^*$ states are less efficient than the main decay of the thymine driven by the $^1(\pi\pi^*)$ state. Hence, the population of the $^{1,3}(n\pi^*)$ states required in the mechanism of (6-4) adduct formation can be considered as a limiting factor of the photoreaction.

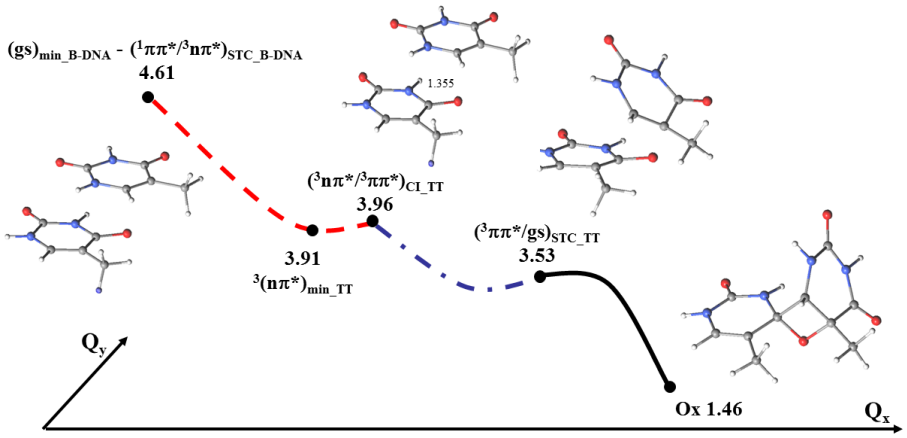

Figure 4.17: Proposed scheme for the photoinduced formation mechanism of the Ox precursor of the thymine-thymine (6-4) adduct. The reported energies (eV) have been calculated at the CASPT2+CP-BSSE //CASSCF(12,12)/ANO-S C,N,O [3s,2p,1d]/H[2s1p] level with respect to two isolated ground-state thymine molecules. Dashed red, dash-dot-dash blue, and solid dark lines indicate the evolution of the system on the $^3(n\pi^*)$, $^3(\pi\pi^*)$, and ground state, respectively. The Q_x coordinate is related mainly to the $C_{4'} = O$ bond stretching, coupled with the variation of the main intermolecular distance. Q_y represents the remaining degrees of freedom.

Finally, combining the present results on the formation of the 6-4 adduct and our previous findings on the cyclobutane thymine dimer (CBT) photoproduction [5,6] and the energy decay paths found in the isolated T nucleobase, [31,32] we are in the position of providing a global view for the photophysical response of the TT system under direct UV absorption for our model system in vacuo (see Figure 4.18). From the bright $^1(\pi\pi^*)$ excited state, the system might undergo three main decay paths, repopulation of the ground state, CBT formation, and thymine-

thymine (6-4) adduct production. The deactivation process followed by the system is initially and primarily controlled by the conformation at the time of light irradiation, which determines if the excitation will delocalize over the two nucleobases via excimer-type interactions or remain localized on a single moiety. In the former, the system might decay along the previously described mechanism to CBT formation on the singlet manifold, although part of the population might also repopulate the ground state. In the second case, most of the population will decay back to the initial ground state through an intra-base mechanism involving an ethene-like CI, and a small percentage might populate the $n\pi^*$ states and consequently activate both the above reported mechanism for the thymine-thymine (6-4) adduct production and the previously studied mechanism for CBT formation on the triplet manifold. It is important to note that all of the mechanisms displayed in Figure 4.18 are barrierless or almost barrierless, which allows us to predict certain effectiveness for the implied processes. Whereas the CBT formation on the singlet manifold requires an initial geometry condition (high degree of π stacking and small value of the dihedral angle between the two carbon-carbon double bonds) that will almost ensure the production of the dimer, the TT orientation needed to activate the mechanism for (6-4) adduct formation will mainly lead to the radiationless repopulation of the ground state. Such a difference, and the fact that on the triplet manifold the two photolessions are competitive, can be related to the experimentally observed lower yield of formation of thymine-thymine (6-4) adduct with respect to CBT in cellular DNA.

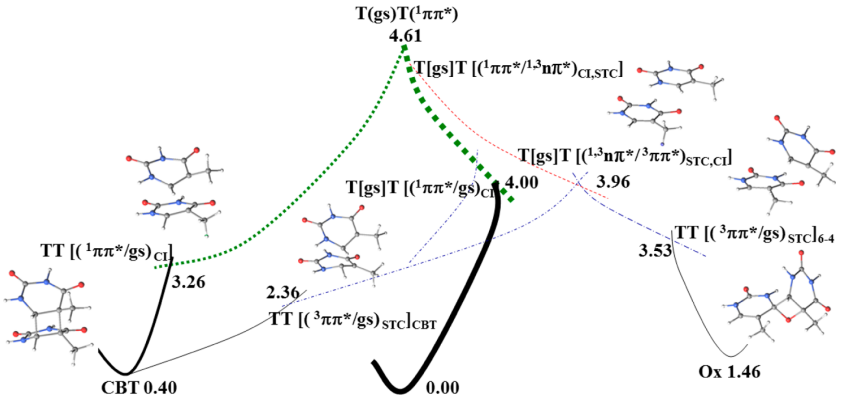

Figure 4.18: Global view for the photoresponse of the TT system under direct UV absorption based on the present and previous studies.[5,6,31,32] The reported energies (eV) have been calculated at the CASPT2+CP-BSSE//CASSCF(12,12)/ANO-S C,N,O[3s,2p,1d]/H[2s1p] level with respect to two isolated ground-state thymine molecules. Dotted green, dash-dot blue, and solid dark lines indicate the evolution of the system on the $^1(\pi\pi^*)$, $^3(\pi\pi^*)$, and ground state, respectively. Dashed red lines indicate the evolution along both the $^3(n\pi^*)$ and $^1(n\pi^*)$ states. The thickness of the lines is an indicator of the probability of the path.

The totally original contribution of the present work has been the determination of a plausible and complete photoinduced mechanism of formation for the thymine-thymine (6-4) adduct. For the first time a connected path from the FC region to the oxetane intermediate has been provided. The obtained photoreaction path constitutes only a possible way for the formation of the considered photolesion, although different facts highlight its plausibility. The study provides an explanation of the low quantum yield of formation for the thymine-thymine (6-4)

adduct; it seems reasonable on the light of the known Paternò-Büchi photoreaction; it points out to the already noticed intrinsic photostability that characterizes the genetic material; and the last but not the least, the conclusions have been obtained on the basis of high-level quantum-chemical calculations, using a well-known methodology which has been proven to be suited for the study of photochemical reactions.

4.2.2 Cytosine, a DNA building block chromophore

It is well accepted that the bright excited state of cytosine is the lowest singlet excited state at the FC region, and it describes a $\pi\pi^*$ excitation localized mainly on the carbon-carbon double bound [1-6]. Since 2002, three main decay channels have been characterized using different methods of electronic structure theory and various strategies in order to explore the more relevant regions of the involved PEHs. All of them are mediated by an easily accessible CI between the lowest singlet excited state and the ground state. In this respect, three main CIs have been described in cytosine (see Figure 4.19). The first one is characterized by single-double bond inversion with respect to the equilibrium geometry of the ground state, and a slight pyramidalization of the C_6 atom. It is normally referred as bond-inversion CI. The second one has a localized distortion on the carbon-carbon double bond similar to the one found in the CI described in the ethene molecule, and is accordingly called ethene-like CI. The main feature of the third one is a strong bending of the amino group out of the plane of the ring, and is named amino-puckered CI. Actually more CIs have been obtained in the cytosine system, but only the above reported intersections have been proposed to be relevant from a photochemical standpoint. The primary difference between the three main decay paths characterized in cytosine

is the considered most important CIs. Other differences are the nature of the excited state at the intersection region, which consequently entails a change or not of the nature of the lowest singlet state along the decay path, and the presence or not of an energy barrier in order to reach the CI. Although this last point is still under debate, it is important to notice that all the computed energy barriers are sufficiently low to determine an ultrafast and efficient passage from the bright excited state to the original ground state.

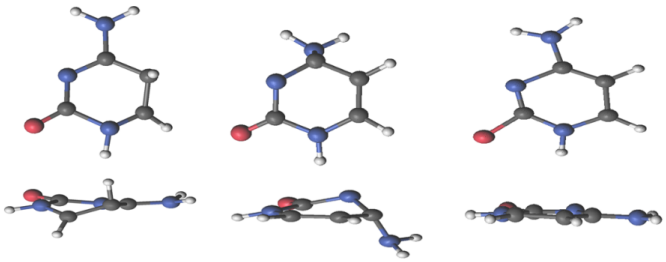

Figure 4.19: Frontal and side views of the structures for the distinct CIs characterized among the lowest-lying excited states and the ground state of cytosine.

The first decay path is mediated by a bond-inversion CI. Such possibility has been described as the most relevant using both the CASSCF method and the CASPT2//CASSCF protocol [7-9]. The second obtained relaxation path is characterized by an easily accessible ethene-like CI. Such reaction path is supported by studies performed with different electronic structure theory methods, as CASPT2//CASSCF, MS-CASPT2//MS-CASPT2, TDDFT, MRCI, CR-EOM-CCSD(T)/CIS, and

DFT/MRCI [12,14-18,30]. Finally, the last possibility involves an amino-puckered CI and it has been found many times to be an accessible way of deactivation competing with the two described decay paths, although in only one paper based on MRCI computations is claimed to be of primary importance [19,20]. As shown above, quite different decay mechanisms have been obtained since the beginning of its study. This undoubtedly reflects the difficult case that cytosine constitutes, and also highlights different remarkable facts. Firstly, the cytosine problem clearly illustrates the importance of a correct use of the theoretical methodologies. In particular, the results obtained with the powerful CASPT2//CASSCF and related MS-CASPT2 methods have turned out to be particularly sensitive to the chosen computational details. Secondly, it points out to the limitation of a static approach in order to unambiguously determine the photophysical response of even a small molecule as cytosine. This last point should be regarded when the photophysics of much more complicated systems would be unveiled.

Having summarized in the above lines the main results obtained up to date on the deactivation paths of cytosine, it is now interesting to present a detailed chronological inspection of the published works on the subject, describing the strategies employed (the adopted electronic structure method and the way in which the PEHs have been explored) and the derived main conclusions.

The first multiconfigurational ab initio quantum chemical study on the deactivation processes undertaken by cytosine after absorption to the lowest singlet $^1(\pi\pi^*)$ excited state was reported in 2002 by Ismail et al. [7]. At the CASSCF/6-31G* level, the authors concluded on the basis of intrinsic reaction coordinate (IRC) calculations that the most probable decay of the $^1(\pi\pi^*)$ state was described by a barrierless path in which an adiabatic switch to the $^1(n_O\pi^*)$ state occurs, reaching subsequently a

minimum region. From the equilibrium region, the system might reach a CI with the ground state by surmounting a barrier height of 3.6 kcal/mol (0.16 eV), and consequently decay back to the original ground state structure. An alternative decay path was also obtained, involving a population transfer from the $^1(n_O\pi^*)$ to the $^1(n_N\pi^*)$ state through a CI placed 9.8 kcal/mol (0.42 eV) above the minimum of the $^1(n_O\pi^*)$ state. The system may further decay toward a CI involving the $^1(n_N\pi^*)$ and the ground states.

Just one year later (in 2003), Merchán and Serrano-Andrés [8] showed that in order to provide a correct description of the PEHs of the excited states of cytosine, an adequate treatment of dynamic electron correlation (not considered previously) is mandatory. The authors in fact performed CASPT2 calculations on top of optimized CASSCF structures, demonstrating that the excited $^1(\pi\pi^*)$ state was directly connected through a CI with the ground state, and consequently the system might decay back through a mechanism that does not involve the $^1(n_O\pi^*)$ state. From the FC region, the $^1(\pi\pi^*)$ state was described to evolve to a minimum structure and then to a CI with the ground state by surmounting a barrier height of 2.5 kcal/mol (0.11 eV). The path involving the $^1(n_N\pi^*)$ state described by Ismail et al. [7] was also studied at the CASPT2 level. A similar CI was identified, accessible from the minimum of the $^1(\pi\pi^*)$ state by surmounting a 12.0 kcal/mol (0.52 eV) barrier height. Such description was obtained by using the LIIC strategy and the CASPT2//CASSCF approach. The 6-31G** basis set was used throughout. In both papers [7,8], the CI mainly responsible for the radiationless deactivation of excited cytosine was characterized by the interchange of the single-double bond character with respect to the ground state minimum geometry and a slight pyramidalization of the C_6 atom, the bond-inversion CI (see Figure 4.19). In the CI involving the

$^1(n_N\pi^*)$ and the ground state, the amino group suffers a pronounced out-of-plane distortion from the ring and it will consequently be denoted as amino-puckered CI (see Figure 4.19).

In 2004, Blancafort and Robb [9] (see also [10]) proposed a decay mechanism based on CASPT2//CASSCF/6-31G* results in which the bright state would first decay to a minimum structure, then pass to a S_1/S_2 CI, and finally decay back to the ground state through a gs/S_1 crossing region by surmounting a small energy barrier. The central idea presented in the paper is that the $^1(\pi\pi^*)$ state decay is mediated by a three-state CI which involves the excited $^1(\pi\pi^*)$ and $^1(n_O\pi^*)$ states and the ground state. Due to the strong mixing related with such a three-fold degenerate situation, the state in that particular region is defined as a mixed $^1(n_O\pi^*)/^1(\pi\pi^*)$ state. This work showed the intrinsic difficulty to unambiguously characterize the nature of the states of cytosine at the crossing region, a problem that will frequently emerge in future studies. IRC calculations were carried out at the CASPT2//CASSCF level.

Besides the description of the non-radiative decay mechanism responsible for the intrinsic photostability of the nucleobase, the processes leading to a possible population of the triplet states started also to be studied, due also to their likely involvement in the photochemistry of cytosine. With the joint efforts of different groups, in 2005 appeared a MEP CASPT2//CASSCF/6-31G** work regarding the subject [11]. By connecting the $^1(\pi\pi^*)$ minimum to the bond-inversion CI, the system might pass through a STC region with the $^3(\pi\pi^*)$ state. In the same year, Tomic et al. [12] studied the relaxation process of the $^1(\pi\pi^*)$ state of cytosine using the DFT/MRCI//TDDFT/TZVP approach. A minimum structure was obtained by computing an unconstrained geometry optimization from the FC region. It was subsequently connected with a CI involving the ground state by a constrained MEP calculation. The

decay path so estimated is characterized by an energy barrier height of around 0.2 eV, and it was assigned as the main radiationless response of the bright state. A similar CI was firslty obtained in 2004 by Sobolewski and Domcke [13] by geometry optimization of a localized excited state of the guanine-cytosine base pair system employing the CIS method. The crossing region, featuring a large elongation and twisting of the C_5= C_6 double bond, is usually identified in the literature as ethene-like $(gs/\pi\pi^*)_{CI}$ crossing (see Figure 4.19). A few months later, the importance of the $(gs/\pi\pi^*)_{CI}$ in cytosine was further highlighted by Zgierski et al. [14] (see also [15,16]). On the basis of CR-EOM-CCSD(T) energy calculations at CIS/cc-pVDZ geometries, the authors showed that the initially excited $^1(\pi\pi^*)$ state might decay to $(gs/\pi\pi^*)_{CI}$, along a path involving a negligible energy barrier. The authors considered that the bright $^1(\pi\pi^*)$ state switches along such decay path to an out-of-plane deformed excited single state of biradical character, which is the one that actually cross with the ground state. As previously pointed out by Merchán and Serrano-Andrés [8], the authors concluded that the $^1(n\pi^*)$ state will not play an important role in the ultrafast non-radiative decay mechanism of cytosine.

In 2006, Merchán et al. [17] (see also [18]) offered a unified study on the ultrafast decay of the canonical pyrimidine nucleobases by computing CASPT2//CASSCF MEP calculations of the related bright states, testing different active spaces and basis sets. The authors showed that both thymine and uracil can decay along a barrierless path to an ethene-like CI with the ground state. Meanwhile, the cytosine system seemed to decay to a minimum structure. Nevertheless, since the path obtained by a LIIC calculation in cytosine at the CASPT2(14,10)/ANO-S C,N,O [3s,2p,1d]/H[2s1p] level of theory between the FC region and an ethene-like $(gs/\pi\pi^*)_{CI}$ crossing has a barrier height of only 2.5 kcal/mol (0.11

eV), it was suggested that the described minimum might be a spurious result probably due to the limited correlation employed in the geometry optimization approach, which was performed at the CASSCF level.

At the beginning of 2007, a new paper exploring the PEHs of cytosine appeared, this time using the MRCI method in conjunction with three different types of expansions [19] (see also [20]) and the cc-pVDZ basis set. Kistler and Matsika concluded that the $^1(\pi\pi^*)$ state decays to a minimum region from which it may evolve along two different paths characterized by similar energy barrier heights of around 0.14 eV. One of them would lead the system to the ethene-like CI, $(gs/\pi\pi^*)_{CI}$. The other, to a crossing point characterized by an out-of-plane distortion of the N_3 atom, whose geometry actually corresponds to the one characterizing the amino-puckered CI. The latter crossing was claimed to involve the $^1(\pi\pi^*)$ and ground state, and not the $^1(n_N\pi^*)$ state as it was previously found [7,8]. The paths described in the paper were obtained by a combination of mass-weighted gradient-directed and LIIC computations. In the same year (2007), Blancafort [21] further studied the system on the basis of IRC calculations at the CASPT2//CASSCF/6-31G* level, leading to the conclusion that from a minimum of the $^1(\pi\pi^*)$ state, the system might decay to the ethene-like $(gs/\pi\pi^*)_{CI}$ by surmounting a barrier height of 0.11 eV or decay first to the $^1(n_N\pi^*)$ state and subsequently to the ground state along a path characterized by an energy barrier height of 0.21 eV. The CI involving the $^1(n_N\pi^*)$ state and the path connecting the FC region to such crossing point closely resemble the one previously described [7,8]. Because of the relatively small barrier found, it was suggested that the $^1(n_N\pi^*)$ state can contribute to the ultrafast decay of the system. On the other hand, Blancafort did disclaim the importance of the bond-inversion CI since according to his new outcomes it entails much higher energies [21].

In 2008, Kistler and Matsika [22] characterized three different three-state CIs and showed their connection with the previously described two-state CIs [19], which according to the authors still remain the main funnels back to the ground state. A computational strategy based on the MRCI method was employed, implemented in a similar fashion as it was already done by the same group in 2007 [19]. The paper did not present a new main deactivation mechanism of the system with respect to that reported in 2007, but provided some useful knowledge about the PEHs and the possible involvement and importance of three-state CIs. Since 2008, different excited-state dynamics studies on cytosine have been performed [23-27]. One of the earlier dynamics studies was performed by Hudock and Martínez [24]. The energies of the populated regions of the PEHs during the dynamics simulation were determined at the CASSCF/6-31G* level. The three different CIs with the ground state depicted in Figure 4.19, i.e., ethene-like CI, bond-inversion CI, and amino-puckered CI, were obtained. Such relevant regions were reoptimized with the MS-CASPT2//MS-CASPT2 approach, and the interpolated paths connecting them with the FC structure were computed. At the higher level of theory employed, the ethene-like and bond-inversion CIs were described to be reached by surmounting an energy barrier. Meanwhile, the path connecting the FC region and the $(gs/n_N\pi^*)_{CI}$ structure was found to be barrierless.

In 2009, Lan et al. [28] studied the photoinduced relaxation dynamics of cytosine using the semiempirical OM2/MRCI method. The optimization of the bright $^1(\pi\pi^*)$ state from the FC region led to the characterization of a minimum structure. Two CIs between the bright excited $^1(\pi\pi^*)$ state and the ground state were obtained. The first can be classified as an ethene-like CI, and is here considered the most relevant since it is placed at lower energies. The second is an amino-

puckered CI, and its role in the deactivation process is believed to be less important due to its higher energy.

In 2010, a paper on the population of triplet states in canonical nucleobases was published [29]. It was shown at the CASPT2//CASSCF/ANO-S C,N,O [3s,2p,1d]/H[2s1p] level that an accessible STC region was located near the ethene-like CI described in 2006 [17], which connects the singlet $^1(\pi\pi^*)$ and triplet $^3(\pi\pi^*)$ states. Once populated, the $^3(\pi\pi^*)$ might relax to a minimum structure, from where it might further decay to a STC region with the ground state.

In 2011, Barbatti et al. [26] (see also [23]) performed dynamics simulations computing the energy gradients with the CASSCF and MR-CISD methods, employing the 6-31G* basis set. One minimum on the S_1 PEH and four different CIs with the ground state were obtained along the trajectories. The low-lying CIs are related to the ethene-like type, bond-inversion, and amino-puckered CIs. LIIC calculations were computed between the FC region and those CIs. The paths obtained both at the MR-CISD and CASSCF levels were found to be barrierless, with the exception of the CASSCF one related to the bond-inversion CI.

A study of cytosine and its imino and enol tautomers has been recently reported by Nakayama et al. [30]. The obtained MEP computation at the MS-CASPT2//MS-CASPT2/Sapporo-DZP level leads to a minimum structure.

In the context of the present thesis, the following CASPT2//CASPT2 MEP on the bright $^1(\pi\pi^*)$ excited state starting from a previously published FC geometry [8] has been obtained (see Figure 4.20). The whole π system of the molecule has been considered in the active space, the ANO-L basis set contracted to O,C,N [4s,3p,1d]/ H[2s1p] has been used, and state averaging has been performed over two states. A MEP cal-

culation using the standard formulation of the CASPT2 method (and not the more recent MS-CASPT2 version) is probably the best computational strategy that can nowadays be applied for the study of cytosine photophysics. The CASPT2 method is in fact able to provide a correct description of both static and dynamic correlation energy in the characterization of photophysical processes in organic chromophores. The use of the MS-CASPT2 method for cytosine, although presents the advantage of producing orthogonal states, can provide misleading outcomes since the technique requires the use of very large active spaces that can be computational handle only for very small molecular systems.

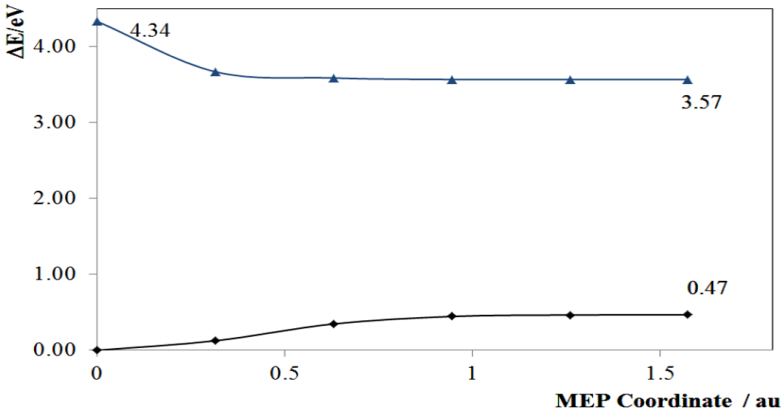

Figure 4.20: Minimum energy path of the bright singlet excited state for cytosine from a previously published FC geometry [8], computed at the CASPT2//CASPT2 level employing the CASSCF(10,8)/ANO-L C,N [4s,3p,1d]/H[2s1p] wave function.

According to the current outcomes, the MEP that characterizes the bright excited state of cytosine leads to a minimum geometry. It is worth noticing that in contrast to the others canonical pyrimidine nucleobases (thymine and uracil), it seems that cytosine does not decay through a barrierless path to an ethene-like CI. The intrinsic reason for such a unique behavior could be related to the presence of the N_3C_4 double bound.

4.3 Chromophores introduced by humans

4.3.1 Asulam, a widely used pesticide

At the time in which the research project started, very little information was available on the photophysics of asulam [1-5]. The almost complete lack of experimental and theoretical results in the literature represented initially certain difficulties, which were successfully overcome by taken into account that the CASPT2//CASSCF protocol has been repeatedly proven to be able to actually predict photophysical and photochemical properties. The performed contribution can consequently be regarded as one of the first theoretical ab initio study on the subject.

The present calculations include CASSCF geometry optimizations, MEPs, and CI and singlet-triplet crossing searches, followed by multi-configurational perturbation theory (CASPT2) calculations at the optimized geometries, using a standard zeroth-order Hamiltonian [6,7]. An imaginary level shift of 0.1 au has been employed to prevent the presence of intruder states. SOC terms and transition dipole moments have also been computed. The final results involve an active space of 6 electrons distributed in 6 orbitals, CASPT2(6,6)//CASSCF. The one-electron basis set of ANO-S type contracted to S[4s3p1d]/C,N,O[3s2p1d]/H[2s] has

been used throughout. The ground state, however, used a geometry optimized at the DFT/B3LYP/6-31G(d) level of calculation. MEPs have been built as steepest-descent paths in which each step required the minimization of the energy on a hyperspherical cross-section of the PEH centered on the initial geometry and characterized by a predefined radius. CIs and singlet-triplet crossings have been computed as minimum energy crossing points (MECP) on the PEH [8,9]. No spatial symmetry restrictions were imposed. The calculations reported used the quantum-chemical methods implemented in the MOLCAS 7.2 package [10] and the Gaussian 09 suite of programs [11].

The photophysics of asulam starts with absorption of near-UV radiation at the FC ground-state geometry of the molecule. Two low-lying singlet excited states, labeled as S_1 ($^1L_b\,\pi\pi^*$) and S_2 ($^1L_a\,\pi\pi^*$) using Platt's nomenclature[12], have been computed at the CASPT2 level at 4.36 (284 nm) and 5.02 eV (247 nm), respectively. The labeling derives from the composition of the CASSCF wave function as displayed in Table 4.8. The transition to the $S_1(^1L_b\,\pi\pi^*)$ state, mainly described as the antisymmetric combination of the HOMO (H) $\rightarrow$ LUMO (L) + 1 (34%) and H - 1 $\rightarrow$ L (27%) one-electron promotions, has a corresponding oscillator strength lower than 10^{-3}. On the contrary, the S_2 ($^1L_a\,\pi\pi^*$) state, with a CASSCF wave function basically composed by the H $\rightarrow$ L (56%) configuration, has a related oscillator strength of 0.15, and consequently, it will be the bright state initially populated in this range of energies and from which the photochemical events will take place; this is also supported by the lack of mirror symmetry between the absorption and emission spectra (Figure 4.21).

Table 4.8: Calculated vertical excitation energies at the FC geometry (E_{VA}) for the lowest valence singlet and spin forbidden triplet states; the related experimental values are also included.

State	Theoretical				Exp.
	E_{VA}/eV (nm)	*f*	μ/D	*Main configurations*	A_{max}/eV (nm)
S_0	–	–	5.51	–	–
T_1 (^3L_a ππ*)	3.64 (340)	–	5.20	H→L(53%); H-1→L+1(22%)	–
T_2 (^3L_b ππ*)	4.19 (296)	–	5.45	H→L+1(47%); H-1→L(31%)	–
T_3 (^3B_a ππ*)	4.27 (290)	–	5.74	H-1→L+1(57%); H→L(22%)	–
S_1 (^1L_b ππ*)	4.36 (284)	$<10^{-3}$	5.26	H→L+1(34%); H-1→L(27%)	–
T_4 (^3B_b ππ*)	5.01 (247)	–	7.71	H→L+1(29%); H-1→L(39%)	–
S_2 (^1L_a ππ*)	5.02 (247)	0.15	8.70	H→L (56%); H→L+1(15%)	4.64(265)[a]
S_3 (^1B_b ππ*)	6.51 (190)	0.17	5.89	H→L+1(21%); H-1→L(20%)	–

[a] Absorption band maximum in chloroform. Estimated oscillator strength: 0.43.

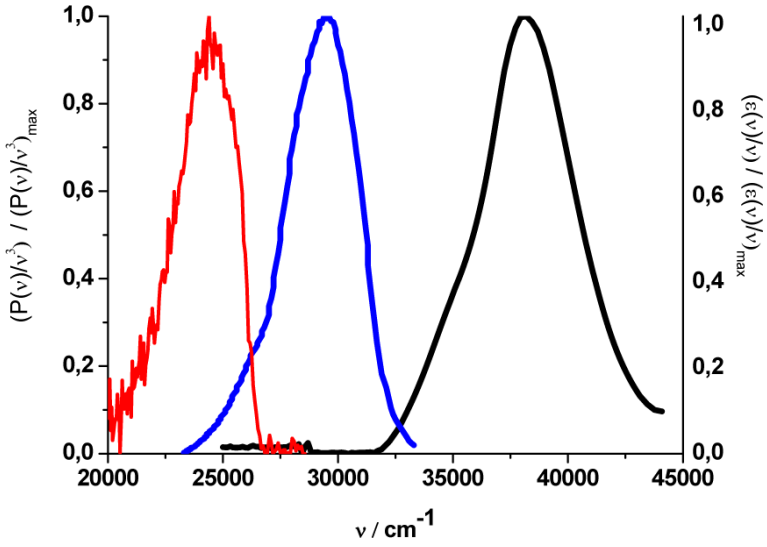

Figure 4.21: Steady-state spectra of ethanolic 16 M asulam in its molecular form. From the left to the right: phosphorescence (ca. 77 K), fluorescence, and UV-vis absorption (ca. 298 K).

The absorption band maximum observed in chloroform at 4.68 eV (265 nm) is therefore clearly assigned to the S_2 ($^1L_a\,\pi\pi^*$) state. The vertical excitation energy, 5.02 eV (247 nm), computed in vacuo is, as usual, placed slightly higher than the band maximum. A third singlet excited state S_3 ($^1B_b\,\pi\pi^*$), formed by the symmetric combination of the H $\rightarrow$ L + 1 and H - 1 $\rightarrow$ L configurations, is computed much higher in energy, 6.51 eV (190 nm) with also a large related oscillator strength of 0.17. Regarding the triplet states, and as it is typical in π conjugated organic molecules, a low-lying vertical excitation is computed for the T_1 ($^3L_a\,\pi\pi^*$) at 3.64 eV, well below the other states. Two other triplet states follow in energy, T_2 ($^3L_b\,\pi\pi^*$) and T_3 ($^3B_a\,\pi\pi^*$), at 4.19 (296 nm) and 4.27 eV (290 nm), respectively. A fourth triplet state is computed

higher than the two lowest singlet states, at 5.01 eV (247 nm). The energy gap between the initially populated S_2 state (in the low-energy region of the spectrum) and the triplet states is large (>0.65 eV) except for T_4. As expected from the qualitative El Sayed rules, all SOC terms are, however, too low in the FC region (<0.30 cm^{-1}) to promote efficient ISC processes, which should take place instead along the deactivation path of S_2. Certainly, all the states found at low energies have a $\pi\pi^*$ character, and therefore SOC interaction is small, whereas $n\pi^*$ or $\pi\sigma^*$ states have been estimated much higher in energy.

The computed dipole moments of the different excited states are similar to that of the ground state, 5.51 D. Exceptions are the S_2 ($^1L_a\,\pi\pi^*$) and T_4 ($^3B_b\,\pi\pi^*$) states, which exhibit large dipole moments of 8.70 and 7.71 D, respectively.

In order to study the photophysical events, the main reaction decay pathway of the spectroscopic S_2 ($^1L_a\,\pi\pi^*$) state has to be determined. Figure 4.22 displays the CASPT2 energies of the low-lying singlet and triplet states of asulam obtained along the CASSCF MEP on the S_2 ($^1L_a\,\pi\pi^*$) state computed from the FC region. Although a small energy barrier can be observed along the path of the state, this feature has a minor significance because it is probably caused by unbalances between the initial S_0 DFT geometry, the computed CASSCF steepest-descent MEP, and the CASPT2 point energies.

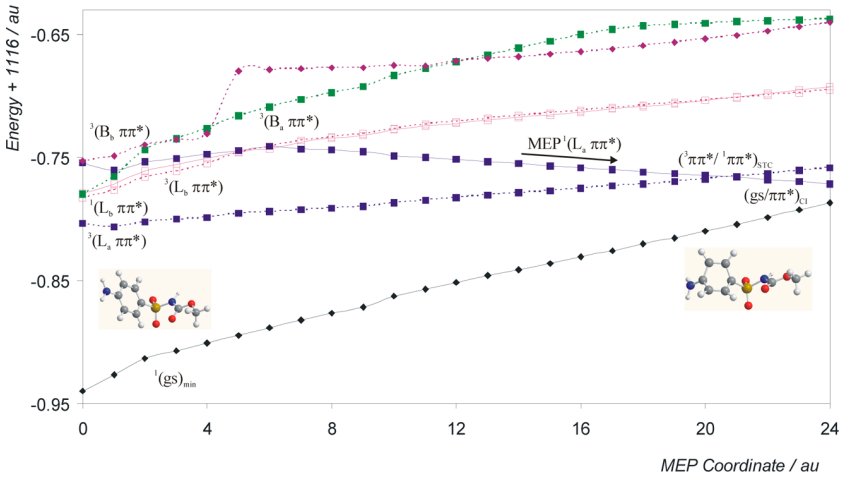

Figure 4.22: CASPT2 low-lying singlet and triplet states of asulam along the MEP computed from the FC geometry on the ($^1L_a\,\pi\pi^*$) state of asulam: singlet states, solid lines, and triplet states, dotted lines.

The path can be considered essentially barrierless from the FC structure toward the region of the CI between the ground and the lowest singlet excited state, named $(gs/\pi\pi^*)_{CI}$ or $(S_0/S_1)_{CI}$ (S_1 now being the vertical S_2 state). Figure 4.23 displays the geometries for asulam at the ground state minimum and at the $(gs/\pi\pi^*)_{CI}$. The latter has been computed independently as a MECP between the S_0 and S_1 states and it is located at 4.12 eV (adiabatically from the ground state minimum) with a structure close to that of the molecule at the end of the MEP. The main distortion undergone by the system along the path has taken place on the benzene ring, which has adopted a boat-like $^{1,4}B$ conformation, [13] a diradicaloid-type structure known in the photochemistry of benzene to be a funnel for the radiationless decay to the ground state [14].

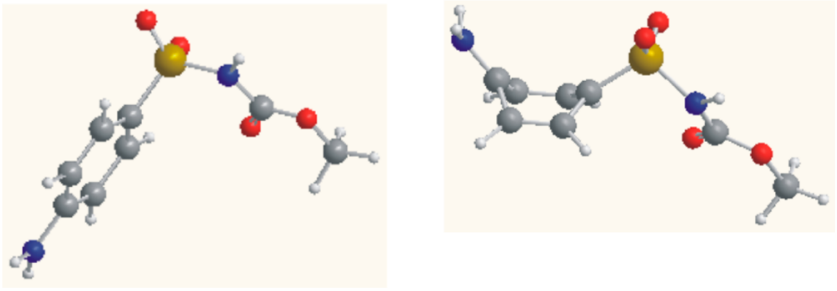

Figure 4.23: Optimized structures of asulam at the ground state minimum, $(gs)_{min}$ (left), and at the CI, $(gs/\pi\pi^*)_{CI}$ (right).

The singlet-state relaxation along a barrierless path leading to CIs with two low-lying singlet states can be expected to be very efficient and, correspondingly, the nonadiabatic decay effects in the CI region. Several singlet and triplet states are crossed during the evolution of the system, and in particular an efficient population transfer can take place (see Figure 4.22) near the crossing regions. Close to point five of the MEP, a degeneracy region between the S_2 ($^1L_a\,\pi\pi^*$) and S_1 ($^1L_b\,\pi\pi^*$) states occurs. From this point, a MEP computed on the S_1 ($^1L_b\,\pi\pi^*$) state hypersurface (see Figure 4.24) leads directly to the minimum of the state, computed adiabatically at 4.39 eV (T_e, 282 nm) with a vertical emission of 4.07 eV (304 nm). Such values can be successfully compared with the fluorescence data obtained in chloroform, yielding band origins and emission maximum of 4.13 (T_0, 300 nm) and 3.83 eV (324 nm), respectively (see Tables 4.9 and 4.10). As the agreement is good enough and no low-lying energy minimum has been located for the S_2 ($^1L_a\,\pi\pi^*$) state, it can be safely assumed that the S_1 ($^1L_b\,\pi\pi^*$) state is the protagonist of the fluorescence. The state minimum displays a dipole moment similar to that of the ground state (4.91 D), and therefore, the emission band should not be strongly affected by the polarity of the solvent. In-

deed, the fluorescence maximum shifts by less than 0.1 eV in different environments. Fluorescence in asulam is, however, weak. The emission quantum yield ϕ_f has been measured to increase with the polarity of the solvent: 0.032 in acetonitrile, 0.099 in ether, and 0.155 in water.

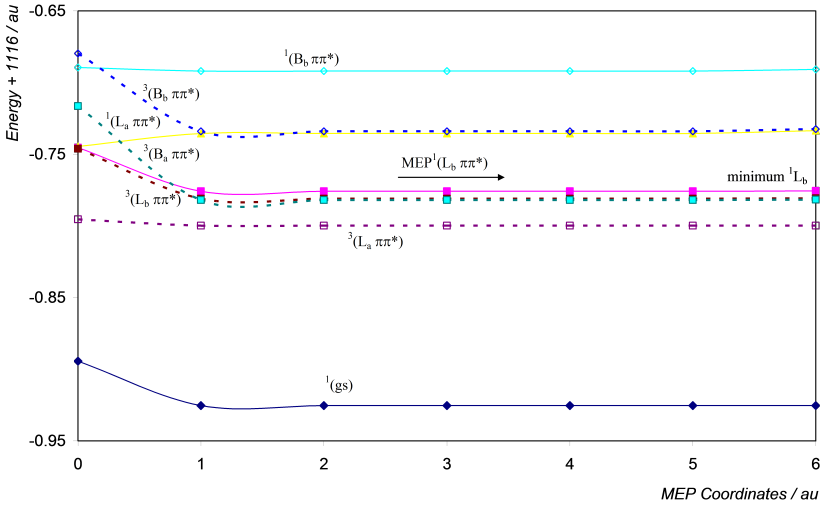

Figure 4.24: Evolution of the lowest singlet and triplet states of asulam from the $(^1L_a/^1L_b)_{CI}$ structure along the $(^1L_b\,\pi\pi^*)$ MEP. It ends at the $(^1L_b\,\pi\pi^*)$ state minimum. Singlet states (solid lines) and triplet states (dotted lines).

Considering the low sensitivity of the S_1 $(^1L_b\,\pi\pi^*)$ emission band on the solvent polarity, the increase on the quantum yield should be related to the stabilization of the highly polar S_2 $(^1L_a\,\pi\pi^*)$ state and, accordingly, of the CI $(S_1/S_2)_{CI}$ triggering the population switch from S_2 to S_1 along the decay of the higher singlet state. The low fluorescence quantum yield also points to the presence of efficient nonradiative decay channels. The theoretical fluorescence radiative lifetime, computed by

means of the Strickler-Berg approximation, corresponds to 3858 ns (as a logical consequence of the low transition dipole moment relating S_0 and S_1), whereas the estimated value in water is 6.25 ns. Theoretical prediction is considerably larger than the available experimental datum that has been also found previously in systems characterized by the presence of important nonradiative paths [15-17]. Nevertheless, it is also worth pointing out that, since different states are involved in absorption and emission, it is difficult to deconvolute these in the extinction coefficient used in the Strickler-Berg approximation.

Table 4.9: Calculated vertical excitation energies at the FC geometry (E_{VA}), electronic band origins (T_e), and vertical emission energies (E_{VE}) for the lowest valence singlet and spin forbidden triplet states; the related experimental values are also included.

	Theoretical /eV (nm)			Experimental /eV (nm)		
State	E_{VA}	T_e	E_{VE}	A_{max}[a]	T_0[a]	E_{max}[a]
$T_1(^3L_a\ \pi\pi^*)$	3.64 (340)	3.61 (343)	2.78 (445)	–	3.44 (360)[b,c]	2.82 (439)[b,c]
$T_2(^3L_b\ \pi\pi^*)$	4.19 (296)	4.23 (292)	3.92 (316)	–	–	–
$T_3(^3B_a\ \pi\pi^*)$	4.27 (290)	–	–	–	–	–
$S_1(^1L_b\ \pi\pi^*)$	4.36 (284)	4.39 (282)	4.07 (304)	–	4.13 (300)[b,d]	3.83 (324)[b,d]
$S_2(^1L_a\ \pi\pi^*)$	5.01 (247)	–[e]	–[e]	4.68 (264)[b]	–	–
$T_4(^3B_b\ \pi\pi^*)$	5.02 (247)	–	–	–	–	–
$S_3(^1B_b\ \pi\pi^*)$	6.51 (190)	–	–	–	–	–

[a] Measured absorption band maximum (Amax), band origin (T_0), and fluorescence maximum (E_{max}). [b] In water (T_1) and chloroform (S_1 and S_2). [c] Computed (83.4 s) and experimental (2.58 s) phosphorescence radiative lifetimes (τ_{Prad}). [d] Computed (3858 ns) and experimental (6.25 ns) fluorescence radiative lifetime (τ_{Frad}). The Strickler-Berg model is not applicable here due to the high nonradiative rates. [e] For the isolated molecule, the MEP on S_2 ($^1L_a\ \pi\pi^*$), after crossing with all other excited states, leads directly to a CI with the ground state, $(S_0/S_1)_{CI}$, placed adiabatically at 4.12 eV.

Table 4.10: Solvent effects on the electronic absorption and fluorescence spectral data of the molecular form of asulam, at T $\simeq$ 298 K.

solvent	$\bar{\nu}_{a,max}$ cm^{-1}(nm)	$\bar{\nu}_{f,max}$ cm^{-1}(nm)	$\bar{\nu}_{a,max} - \bar{\nu}_{f,max}$ cm^{-1}
dichloromethane	37594 (266)	30864 (324)	6730
trichloromethane	27736 (265)	30864 (324)	6872
propan-1-ol	37313 (268)	29761 (336)	7552
acetonitrile	37313 (268)	30030 (333)	7283
metanol	37453 (267)	29673 (337)	7780
etanol	38197 (262)	29762 (336)	8435
ethylene glicol	36900 (271)	29661 (336)	7139
1,4-dioxane	37594 (266)	30211 (331)	7383
diethyl ether	37453 (267)	30487 (328)	6966
water	37313 (268)	29412 (340)	7901

Along the evolution through the S_2 ($^1L_a\,\pi\pi^*$) state decay, four triplet states are crossed, one at the beginning (5.0 eV), T_4 ($^3B_b\,\pi\pi^*$), then T_3 ($^3B_a\,\pi\pi^*$) and T_2 ($^3L_b\,\pi\pi^*$), and finally the T_1 ($^3L_a\,\pi\pi^*$) state close to the end of the path (4.5 eV), that is, near the CI $(gs/\pi\pi^*)_{CI}$ and displaying, therefore, a similar structure. The computed electronic SOC terms between the S_2 ($^1L_a\,\pi\pi^*$) and the different triplet states at the corresponding STC regions are somewhat low ($<$0.3 cm^{-1}), although such values are probably underestimated because the relative small number of states included in the coupling (four singlet and four triplet states, all of $\pi\pi^*$ type). In any case, the computed overall ISC rate at each of the STC regions is expected to become large enough to guarantee efficient processes once the vibrational effects and density of states are taken into account in the SOC coupling, as it has been established in a number of systems [18]. We have followed the respective MEPs from the STC crossings between S_2 ($^1L_a\,\pi\pi^*$) and T_2 and T_1, which display the largest SOC values in the crossing regions ($\sim$0.3 cm^{-1} in both cases). The T_2 state evolves toward its minimum, as shown by

computing the corresponding MEPs (see Figure 4.25), and finally, it decays to the lowest T_1 triplet state through an efficient triplet-triplet IC processes because the corresponding $(T_2/T_1)_{CI}$ lies close by the T_2 minimum (see Figure 4.26). The second MEP computed leads the T_1 ($^3L_a\,\pi\pi^*$) from the $(S_2/T_1)_{STC}$ toward the triplet state minimum (see Figure 4.27). In either case, IC from T_2 or ISC from S_2, the T_1 ($^3L_a\,\pi\pi^*$) will decay to its own minimum and become phosphorescent (see Figure 4.28).

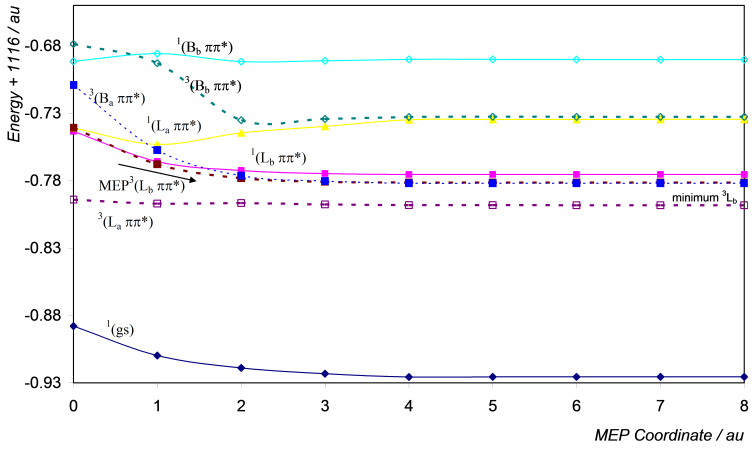

Figure 4.25: Evolution of the lowest singlet and triplet states of asulam from the $(^3L_b/^1L_a)_{STC}$ structure along the ($^3L_b\,\pi\pi^*$) MEP. It ends at the ($^3L_b\,\pi\pi^*$) state minimum. Singlet states (solid lines) and triplet states (dotted lines).

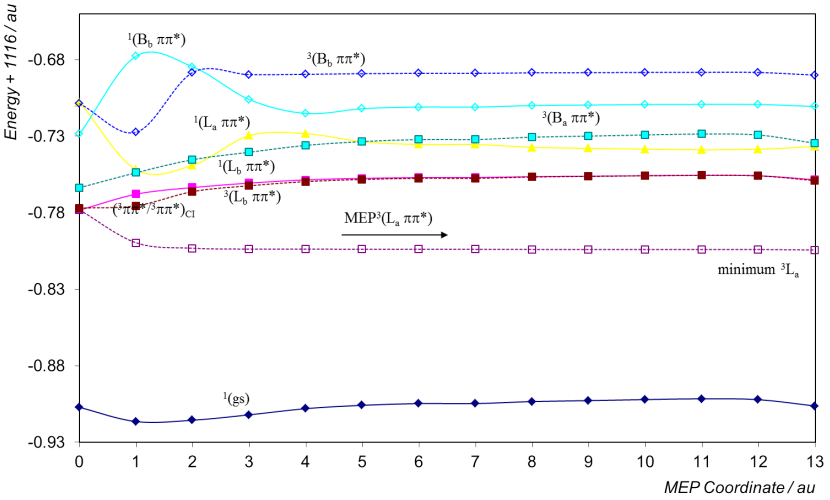

Figure 4.26: Evolution of the lowest singlet and triplet states of asulam from the $(^3L_b/^3L_a)_{CI}$ structure along the $(^3L_a\,\pi\pi^*)$ MEP. It ends at the $(^3L_a\,\pi\pi^*)$ state minimum. Singlet states (solid lines) and triplet states (dotted lines).

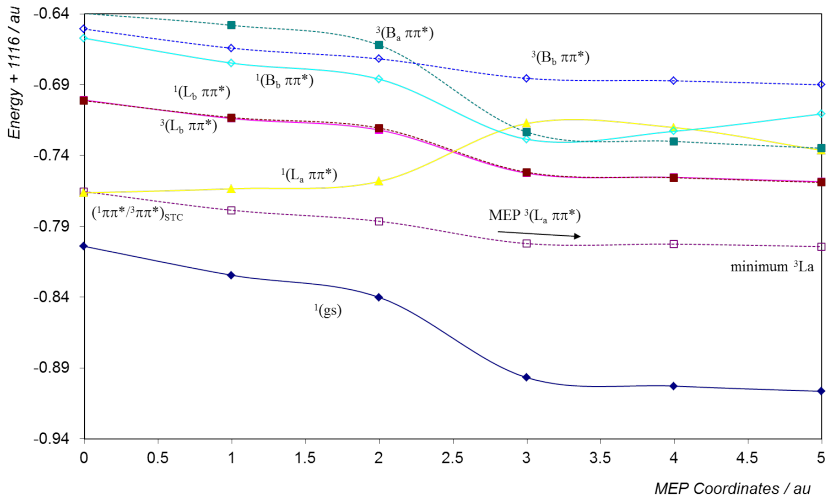

Figure 4.27: Evolution of the lowest singlet and triplet states of asulam from the $(^3L_a/^1L_a)_{STC}$ structure along the $(^3L_a\,\pi\pi^*)$ MEP. It ends at the $(^3L_a\,\pi\pi^*)$ state minimum. Singlet states (solid lines) and triplet states (dotted lines).

Considering the different energy ranges in which the STC regions are located, the triplet quantum yield is expected to be wavelength dependent, an effect and a mechanism present in molecules such as thymine, uracil, or adenine [19,20]. Regarding the parameters computed for the phosphorescence, the band origin, 3.61 eV (T_e, 343 nm), and vertical emission, 2.78 eV (445 nm), are in good correspondence with the experimental values in water, 3.44 (360 nm) and 2.82 eV (439 nm), respectively.

Part of the population of the triplet states may also decay back to the original ground state through a nonradiative process. In fact, the T_1 minimum might reach an intersystem crossing region between the T_1 and the ground state, $(gs/^3L_a\,\pi\pi^*)_{STC}$, surmounting a small barrier of

0.41 eV (10 $kcal\,mol^{-1}$). The ISC funnel in which the electronic SOC has been computed to be 0.86 cm^{-1}, favoring then the energy transfer, is easily accessible with the available excess energy and, consequently, contributes to the large ratio of radiationless decay experimentally determined (0.48). The presented photoprocesses that the system may undergo are summarized in Figure 4.28, which displays a scheme of the photophysics of asulam based on CASPT2 results.

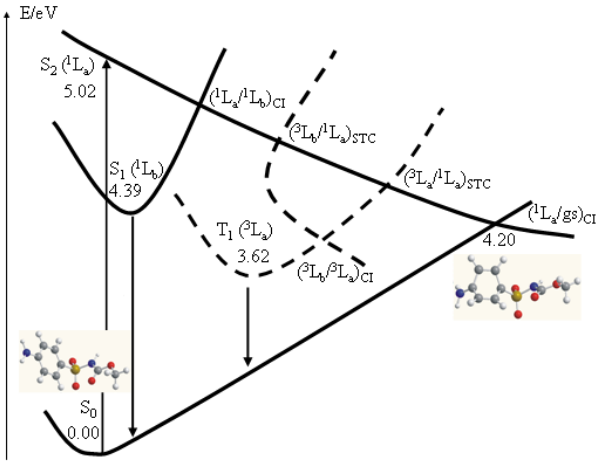

Figure 4.28: Summary of the photophysics of asulam based on the CASPT2 results.

Having performed a theoretical study of the system, it is now interesting to compare the computational results with the experimentally registered data. As highlighted above, the lower values of the fluorescence and phosphorescence quantum yield obtained experimentally

can be ascribed to the easily accessible CI between the bright and the ground state and the attainable STC between the lowest triplet and the ground state. The experimental registration of phosphorescence radiation agrees with the presence of the accessible STCs found theoretically. The computed vertical and emission energies and electronic band origins are in agreement with the related experimental data (see Table 4.9). For the sake of comparison, the results obtained in chloroform have been used, since the low value of the dipole moment more closely resembles the in-vacuo situation of the calculations. It is worth recalling that actually the strictly comparable quantity that can be directly related to the experimental value is the band origin, calculated from the adiabatic electronic transition energy by including the zero-point vibrational energy in both the initial and final states. The experimental data show little solvent effects on the position and shape of the absorption and fluorescence band. Taking the value obtained in trichloromethane as reference, except for ethanol, the absorption band displays a small red-shift as the polarity of the solvent increases (around 0.04 eV), while the fluorescence band has larger red-shifts (around 0.11 eV). Since the theoretical value obtained for the dipole moment of the bright ($^1L_a\,\pi\pi^*$) state is considerably larger that the corresponding value for the ground and the fluorescence ($^1L_b\,\pi\pi^*$) states (8.70, 5.26, and 5.51 D, respectively), the reported experimental trend is not explained solely on the basis of the presumable higher stabilization undergone by the ($^1L_a\,\pi\pi^*$) state with respect to the ($^1L_b\,\pi\pi^*$) state in more polar solvents.

The performed theoretical work elucidates part of the intrinsic photophysical properties of asulam under UVA and UVB exposure. According to the obtained results, a photodegradation process of the system catalyzed by solar radiation seems not to be probable, since the system has shown to be actually photostable due to its ability to efficiently

dissipate the absorbed energy.

4.4 References

1-aminonaphthalene

[1] Berden, G.; Meerts, W. L.; Plusquellic, D. F.; Fujita, I.; Pratt, D. W. *J. Chem. Phys.* **1996**, *104*, 3935.

[2] Jiang, S.; Levy, D. H. *J. Phys. Chem. A* **2002**, *106*, 8590.

[3] Rückert, I.; Demeter, A.; Morawski, O.; Kühnle, W.; Tauer, E.; Zachariasse, K. A. *J. Phys. Chem. A* **1999**, *103*, 1958.

[4] Andersson, K.; Malmqvist, P. Å.; Roos, B. O. *J. Chem. Phys.* **1992**, *96*, 1218.

[5] De Vico, L.; Olivucci, M.; Lindh, R. *J. Chem. Theory Comput.* **2005**, *1*, 1029.

[6] Serrano-Andrés, L.; Merchán, M.; Nebot-Gil, I.; Lindh, R.; Roos, B. O. *J. Chem. Phys.* **1993**, *98*, 3151.

[7] Roos, B. O.; Andersson, K.; Fülscher, M. P.; Malmqvist, P.-Å.; Serrano-Andrés, L.; Pierloot, K.; Merchán, M. *Adv. Chem. Phys.* **1996**, *93*, 219.

[8] Merchán, M.; Serrano-Andrés, L. In *Computational Photochemistry*; Olivucci, M., Ed.; Elsevier: Amsterdam, The Netherlands, 2005.

[9] Borin, A. C.; Serrano-Andrés, L. *Chem. Phys.* **2000**, *262*, 253.

[10] Serrano-Andrés, L.; Merchán, M. In *Encyclopedia of Computational Chemistry*; Schleyer, P. v. R., Schreiner, P. R., Schaefer, H. F., III, Jorgensen, W. L., Thiel, W., Glen, R. C., Eds.; Wiley: Chichester, U.K., 2004.

[11] Serrano-Andrés, L.; Merchán, M. *J. Mol. Struct. (THEOCHEM)* **2005**, *729*, 109.

[12] Olaso-González, G.; Merchán, M.; Serrano-Andrés, L. *J. Phys. Chem. B* **2006**, *110*, 24734.

[13] Serrano-Andrés, L.; Merchán, M.; Borin, A. C. *Proc. Natl. Acad. Sci. U.S.A.* **2006**, *103*, 8691.

[14] Serrano-Andrés, L.; Merchán, M.; Borin, A. C. *Chem. Eur. J.* **2006**, *12*, 6559.

[15] Serrano-Andrés, L.; Merchán, M.; Lindh, R. *J. Chem. Phys.* **2005**, *122*, 104107.

[16] Andersson, K.; et al. *MOLCAS*, version 6.4; Department of Theoretical Chemistry, Chemical Centre, University of Lund: Lund, Sweden, 2006.

[17] Karlström, G.; Lindh, R.; Malmqvist, P.-Å.; Roos, B. O.; Ryde, U.; Veryazov, V.; Widmark, P.-O.; Cossi, M.; Schimmelpfennig, B.; Neogrady, P.; Seijo, L. *Comput. Mater. Sci.* **2003**, *28*, 222.

[18] Veryazov, V.; Widmark, P.-O.; Serrano-Andrés, L.; Lindh, R.; Roos, B. O. *Int. J. Quantum Chem.* **2004**, *100*, 626.

[19] Strickler, S. J.; Berg, R. A. *J. Chem. Phys.* **1962**, *37*, 814.

[20] Rubio-Pons, O.; Serrano-Andrés, L.; Merchán, M. *J. Phys. Chem. A* **2001**, *105*, 9664.

[21] Lahmani, F.; Zehnacker-Rentien, A.; Coudert, L. H.; Zachariasse, K. A. *J. Phys. Chem. A* **2003**, *107*, 7364.

[22] Souto, M. A.; Michl, J. *J. Am. Chem. Soc.* **1978**, *100*, 6853.

[23] Majewski, W. A.; Meerts, W. L. *J. Mol. Spectrosc.* **1984**, *104*, 271.

[24] Johnson, J. R.; Jordan, K. D.; Plusquellic, D. F.; Pratt, D. W. *J. Chem. Phys.* **1990**, *93*, 2258.

[25] Böhm, M.; Tatchen, J.; Krugler, D.; Kleinermanns, K.; Nix, M. G. D.; LeGreve, T. A.; Zwier, T. S.; Schmitt, M. *J. Phys. Chem. A* **2009**, *113*, 2458.

[26] Merchán, M.; González-Luque, R.; Climent, T.; Serrano-Andrés, L.; Rodríguez, E.; Reguero, M.; Peláez, D. *J. Phys. Chem. B* **2006**,

110, 26471.

[27] Serrano-Andrés, L.; Merchán, M.; Borin, A. C. *J. Am. Chem. Soc.* **2008**, *130*, 2473.

[28] Serrano-Andrés, L.; Merchán, M. In *Radiation Induced Molecular Phenomena in Nucleic Acids;* Eds. M. K. Shukla and J. Leszczynski, Springer, The Netherlands, 2008, pp 435-472.

[29] Wassam, W. A.; Lim, E. C. *J. Chem. Phys.* **1978**, *68*, 433.

[30] Mulder, W. H.; Párkányi, C. *J. Phys. Chem. A* **2002**, *106*, 11932.

[31] Serrano-Andrés, L.; Roos, B. O. *J. Am. Chem. Soc.* **1996**, *118*, 185.

[32] Platt, J. R. *J. Chem. Phys.* **1949**, *17*, 484.

[33] Rubio, M.; Merchán, M.; Ortí, E.; Roos, B. O. *Chem. Phys.* **1994**, *179*, 395.

[34] Suzuki, K.; Demeter, A.; Kühnle, W.; Tauer, E.; Zachariasse, K. A.; Tobita, S.; Shizuka, H. *Phys. Chem. Chem. Phys.* **2000**, *2*, 981.

[35] Meech, S. R.; O'Connor, D. V.; Phillips, D.; Lee, A. G. *J. Chem. Soc., Faraday Trans. 2* **1983**, *79*, 1563.

[36] Beck, S. M.; Hopkins, J. B.; Powers, D. E.; Smalley, R. E. *J. Chem. Phys.* **1981**, *74*, 43.

[37] Behlen, F. M.; Rice, S. A. *J. Chem. Phys.* **1981**, *75*, 5672.

[38] Stockburger, S.; Gattermann, H.; Klusmann, W. *J. Chem. Phys.* **1975**, *63*, 4519.

[39] Montero, R.; Longarte, A.; Martínez, R.; Sánchez Rayo, M. N.; Castaño, F. *Chem. Phys. Lett.* **2009**, *468*, 134.

Indole, the main emissive source of proteins

[1] Hollas, J. M. *Spectrochim. Acta* **1963**, *19*, 753.

[2] Lami, H. *J. Chem. Phys.* **1977**, *67*, 3274.

[3] Lami, H. *Chem. Phys. Lett.* **1977**, *48*, 447.

[4] Ilich, P. *Can. J. Spectrosc.* **1987**, *67*, 3274.

[5] Bartis, T. L. O.; Grace, L. I.; Dunn, T. M.; Lubman, D. M. *J. Phys. Chem.* **1993**, *97*, 5820.

[6] Strickland, E. H.; Horwitz, J.; Billups, C. *Biochemistry* **1970**, *25*, 4914.

[7] Fender, B. J.; Sammeth, D. M.; Callis, P. R. *Chem. Phys. Lett.* **1995**, *239*, 31.

[8] Lami, H.; Glasser, N. *J. Chem. Phys.* **1986**, *84*, 597.

[9] Chang, C. T.; Wu, C. Y.; Muirhead, A .R.; Lombardi, J. R. *Photochem. Photobiol.* **1974**, *19*, 347.

[10] Caminati, W.; Di Bernardo, S. *J. Mol. Struct.* **1990**, *240*, 253.

[11] Glasser, N.; Lami, H. *J. Chem. Phys.* **1981**, *74*, 6526.

[12] Lin, M. F.; Tseng, C. M.; Lee, Y. T.; Ni, C. K. *J. Chem. Phys.* **2005**, *123*, 124303.

[13] Nix, M. G. D.; Devine, A. L.; Cronin, B.; Ashfold, M. N. R. *Phys. Chem. Chem. Phys.* **2006**, *8*, 2610.

[14] Borisevich, N. A.; Sukhodola, A. A.; Tolstorozhev, G. B. *Chem. Phys.* **2008**, *354*, 44.

[15] Zuckich, J.; von Schütz, J. U.; Maki, A. M. *J. Am. Chem. Soc.* **1974**, *96*, 710.

[16] Wilkinson, F.; Garmer, A. *J. Chem. Soc., Faraday Trans. 2* **1977**, *73*, 222.

[17] Brand, C.; Küpper, J; Pratt, D. W.; Meerts, W. L.; Krügler, D.; Tatchen, J.; Schmitt, M. *Phys. Chem. Chem. Phys.* **2010**, *12*, 4968.

[18] Küpper, J; Pratt, D. W.; Meerts, W. L.; Brand, C.; Tatchen, J.; Schmitt, M. *Phys. Chem. Chem. Phys.* **2010**, *12*, 4980.

[19] Serrano-Andrés, L.; Roos, B. O. *J. Am. Chem. Soc.* **1996**, *118*, 185.

[20] Sobolewski, A. L.; Domcke, W. *Chem. Phys. Lett.* **1999**, *315*, 293.

[21] Borin, A. C.; Serrano-Andrés, L. *Chem. Phys.* **2000**, *262*, 253.

[22] Serrano-Andrés, L.; Borin, A. C. *Chem. Phys.* **2000**, *262*, 267.

[23] Sobolewski, A. L.; Domcke, W.; Dedonder-Lardeux, C.; Jouvet, C. *Phys. Chem. Chem. Phys.* **2002**, *4*, 1093.

[24] Sobolewski, A. L.; Domcke, W. *J. Phys. Chem. A* **2007**, *111*, 11725.

[25] Platt, J. R. *J. Chem. Phys.* **1949**, *17*, 489.

[26] De Vico, L.; Olivucci, M.; Lindh, R. *J. Chem. Theory Comput.* **2005**, *1*, 1029.

[27] Anglada, J. M.; Bofill, J. M. *J. Comput. Chem.* **1997**, *18*, 992.

[28] Merchán,M.; González-Luque, R.; Climent, T.; Serrano-Andrés, L.; Rodríguez, E.; Reguero, M.; Peláez, D. *J. Phys. Chem. B* **2006**, *110*, 26471.

[29] Serrano-Andrés, L.; Merchán, M.; Borin, A. C. *J. Am. Chem. Soc.* **2008**, *130*, 2473.

[30] Andersson, K.; Malmqvist, P.-Å.; Roos, B. O. *J. Chem. Phys.* **1992**, *96*, 1218.

[31] Roos, B. O.; Andersson, K.; Fülscher, M. P.; Malmqvist, P.-Å.; Serrano-Andrés, L.; Pierloot, K.; Merchán, M. *Adv. Chem. Phys.* **1996**, *93*, 219.

[32] Serrano-Andrés, L.; Merchán, M. Spectroscopy: Applications. In *Encyclopedia of Computational Chemistry*; Schleyer, P. v. R., Schreiner, P. R., Schaefer, H. F., III, Jorgensen, W. L., Thiel, W., Glen, R. C., Eds., Wiley, Chichester, 2004, pp 1-51.

[33] Roca-Sanjuán, D.; Aquilante, F.; Lindh, R. *WIREs: Comput. Mol. Sci.* **2012**, *2*, 585.

[34] Aquilante, F.; De Vico, L.; Ferré, N.; Ghigo, G.; Malmqvist, P.Å.; Pedersen,T.; Pitonak, M.; Reiher, M.; Roos, B. O.; Serrano-Andrés, L.; Urban, M.; Veryazov, V.; Lindh, R. *J. Comput. Chem.* **2010**, *31*, 224.

[35] Merchán, M.; Serrano-Andrés, L. In *Computational Photochemistry, 1st ed.*; Olivucci, M., Ed.; Elsevier: Amsterdam, The Netherlands, 2005; Vol. 16, pp 35-91.

[36] Serrano-Andrés, L.; Merchán, M. In *Radiation Induced Molecular Phenomena in Nucleic Acids;* Eds. M. K. Shukla and J. Leszczynski, Springer, The Netherlands, 2008, pp 435-472.

[37] Garavelli, M. T*heor. Chem. Acc.* **2006**, *116*, 87.

[38] Garavelli, M.; Bernardi, F.; Cembran, A. In *Computational Photochemistry, 1rd ed.*; Olivucci, M., Ed.; Elsevier: Amsterdam, The Netherlands, 2005; Vol. 16, pp 191-223.

[39] Takigawa, T.; Ashida, T.; Sasado, Y.; Kakuda, M. *Bull. Chem. Soc. Jpn.* **1966**, *39*, 2369.

[40] Michl, J. In *Computational Photochemistry, 1rd ed.*; Olivucci, M., Ed.; Elsevier: Amsterdam, The Netherlands, 2005; Vol. 16, pp ix-xi.

[41] Song, P. S.; Kurtin, W. E. *J. Am. Chem. Soc.* **1969**, *91*, 4892.

[42] Eftink, M. R. In *Methods of Biochemical Analysis*; Suelter, C. H., Ed.; John Wiley & Sons: New York, 1991; Vol. 35.

[43] Garavelli, M.; Celani, P.; Yamamoto, N.; Bernardi, F.; Robb, M. A.; Olivucci, M. *J. Am. Chem. Soc.* **1996**, *118*, 11656.

[44] Garavelli, M.; Bernardi, F.; Cembran, A.; Castaño, O.; Frutos, L. M.; Merchán, M.; Olivucci, M. *J. Am. Chem. Soc.* **2002**, *124*, 13770.

[45] Wohlgemuth, M.; Bonai-Koutecký, V.; Mitric, R. *J. Chem. Phys.* **2011**, *135*, 054105.

Thymine-Thymine (6-4) adduct, a DNA photolesion

[1] Cadet, J.; Vigny, P. In *Bioorganic Photochemistry*; Morrison, H., Ed.; John Wiley & Sons, Inc.: New York, 1990; Vol. 1, pp 1-272.

[2] Sinha, R. P.; Hader, D. P. *Photochem. Photobiol. Sci.* **2002**, *1*, 225.

[3] Douki, T.; Cadet, J. *Biochemistry* **2001**, *40*, 2495.

[4] Roca-Sanjuán, D.; Olaso-González, G.; González-Ramírez, I.; Serrano-Andrés, L.; Merchán, M. *J. Am. Chem. Soc.* **2008**, *130*, 10768.

[5] Serrano-Pérez, J. J.; González-Ramírez, I.; Coto, P. B.; Merchán, M.; Serrano-Andrés, L. *J. Phys. Chem. B* **2008**, *112*, 14096.

[6] Climent, T.; González-Ramírez, I.; González-Luque, R.; Merchán, M.; Serrano-Andrés, L. *J. Phys. Chem. Lett.* **2010**, *1*, 2072.

[7] Manson, F.; Laino, T.; Tavernelli, I.; Rothlisberger, U.; Hutter, J. *J. Am. Chem. Soc.* **2008**, *130*, 3443.

[8] Schreier, W. J.; Schrader, T. E.; Koller, F. O.; Gilch, P.; Crespo-Hernández, C. E.; Swaminathan, V. N.; Carell, T.; Zinth, W.; Kohler, B. *Science* **2007**, *315*, 625.

[9] Mouret, S.; Baudouin, C.; Charveron, M.; Favier, A.; Cadet, J.; Douki, T. *Proc. Natl. Acad. Sci. U.S.A.* **2006**, *103*, 13765.

[10] Kwok, W. M.; Ma, C.; Phillips, D. L. *J. Am. Chem. Soc.* **2008**, *130*, 5131.

[11] Cuquerella, M. C.; Lhiaubet-Vallet, V.; Bosca, F.; Miranda, M. A. *Chem. Sci.* **2011**, *2*, 1219.

[12] Blancafort, L.; Migani, A. *J. Am. Chem. Soc.* **2007**, *129*, 14540.

[13] Yang, Z. B.; Zhang, R. B.; Eriksson, L. A. *Phys. Chem. Chem. Phys.* **2011**, *13*, 8961.

[14] Yang, Z. B.; Eriksson, L. A.; Zhang, R. B. *J. Phys. Chem. B* **2011**, *115*, 9681.

[15] Marguet, S.; Markovitsi, D. *J. Am. Chem. Soc.* **2005**, *127*, 5780.

[16] Domratcheva, T.; Schlichting, I. *J. Am. Chem. Soc.* **2009**, *131*, 17793.

[17] Li, J.; Liu, Z.; Tan, C.; Guo, X.; Wang, L.; Sancar, A.; Zhong, D. *Nature* **2010**, *466*, 887.

[18] Faraji, S.; Dreuw, A. *J. Phys. Chem. Lett.* **2012**, *3*, 227.

[19] Paternò, E.; Chiefi, G. *Gazz. Chim. Ital.* **1909**, *39*, 431.

[20] Palmer, I. J.; Ragazos, I. N.; Bernardi, F.; Olivucci, M.; Robb, M. A. *J. Am. Chem. Soc.* **1994**, *116*, 2121.

[21] Andersson, K.; Malmqvist, P.-Å.; Roos, B. O. *J. Chem. Phys.* **1992**, *96*, 1218.

[22] Roos, B. O.; Andersson, K.; Fülscher, M. P.; Malmqvist, P.-Å.; Serrano-Andrés, L.; Pierloot, K.; Merchán, M. *Adv. Chem. Phys.* **1996**, *93*, 219.

[23] Serrano-Andrés, L.; Merchán, M. In *Encyclopedia of Computational Chemistry*; Schleyer, P. v. R., Schreiner, P. R., Schaefer, H. F., III, Jorgensen, W. L., Thiel, W., Glen, R. C., Eds.; Wiley: Chichester, U.K., 2004; pp 1-51.

[24] Roca-Sanjuán, D.; Aquilante, F.; Lindh, R. *WIREs: Comput. Mol. Sci.* **2012**, *2*, 585.

[25] Aquilante, F.; De Vico, L.; Ferré, N.; Ghigo, G.; Malmqvist, P.-Å.; Pedersen, T.; Pitonak, M.; Reiher, M.; Roos, B. O.; Serrano-

Andrés, L.; Urban, M.; Veryazov, V.; Lindh, R. *J. Comput. Chem.* **2010**, *31*, 224.

[26] Pierloot, K.; Dumez, B.; Widmark, P.-O.; Roos, B. O. *Theor. Chem. Acta* **1995**, *90*, 87.

[27] Merchán, M.; Serrano-Andrés, L. In *Computational Photochemistry, 1st ed.*; Olivucci, M., Ed.; Elsevier: Amsterdam, The Netherlands, 2005; Vol. 16, pp 35-91.

[28] Serrano-Andrés, L.; Merchán, M. In *Radiation Induced Molecular Phenomena in Nucleic Acids;* Eds. M. K. Shukla and J. Leszczynski, Springer, The Netherlands, 2008, pp 435-472.

[29] Giussani, A.; Merchán, M.; Roca-Sanjuán, D.; Lindh, R. *J. Chem. Theory Comput.* **2011**, *7*, 4088.

[30] Boys, S. F.; Bernardi, F. *Mol. Phys.* **2002**, *100*, 65.

[31] Merchán, M.; González-Luque, R.; Climent, T.; Serrano-Andrés, L.; Rodríguez, E.; Reguero, M.; Peláez, D. *J. Phys. Chem. B* **2006**, *110*, 26471.

[32] Serrano-Pérez, J. J.; González-Luque, R.; Merchán, M.; Serrano-Andrés, L. *J. Phys. Chem. B* **2007**, *111*, 11880.

[33] Etinski, M.; Fleig, T.; Marian, C. M. *J. Phys. Chem. A* **2009**, *113*, 11809.

[34] Brogaard, R. Y.; Schalk, O.; Boguslavskiy, A. E.; Enright, G. D.; Hopf, H.; Raev, V.; Tarcoveanu, E.; Sølling, T. I.; Stolow, A. *Phys. Chem. Chem. Phys.* **2012**, *14*, 8572.

Cytosine, a DNA building block chromophore

[1] Shukla, M. K.; Leszczynski, J. *J. Comp. Chem.* **2004**, *25*, 768.

[2] Fleig, T.; Knecht, S.; Hättig, C. *J. Phys. Chem. A* **2007**, *111*, 5482.

[3] Szalay, P. G.; Watson, T.; Perera, A.; Lotrich, V. F.; Bartlett, R. J. *J. Phys. Chem. A* **2012**, *116*, 6702.

[4] Silva-Junior, M.R.; Schreiber, M.; Sauer, S. P. A.; Thiel, W. *J. Chem. Phys.* **2008**, *129*, 104103.

[5] Serrano-Andrés, L.; Merchán, M. In *Radiation Induced Molecular Phenomena in Nucleic Acids;* Eds. M. K. Shukla and J. Leszczynski, Springer, The Netherlands, 2008, pp 435-472.

[6] Schreiber, M.; Silva, M. R.; Sauer, S. P. A.; Thiel, W. *J. Chem. Phys.* **2008**, *128*, 134110.

[7] Ismail, N.; Blancafort, L.; Olivucci, M.; Kohler, B.; Robb, M. A. *J. Am .Chem. Soc.* **2002**, *124*, 6818.

[8] Merchán, M.; Serrano-Andrés, L. *J. Am .Chem. Soc.* **2003**, *125*, 8108.

[9] Blancafort, L.; Robb, M. A. *J. Phys. Chem. A* **2004**, *108*, 10609.

[10] Blancafort, L.; Cohen, B.; Hare, P. M.; Kohler, B.; Robb, M. A. *J. Phys. Chem. A* **2005**, *109*, 4431.

[11] Merchán, M.; Serrano-Andrés, L.; Robb, M. A.; Blancafort, L. *J. Am .Chem. Soc.* **2005**, *127*, 1820.

[12] Tomić, K.; Tatchen, J.; Marian, C. M. *J. Phys. Chem. A* **2005**, *109*, 8410.

[13] Sobolewski, A. L.; Domcke, W. *Phys. Chem. Chem. Phys.* **2004**, *6*, 2763.

[14] Zgierski, M. Z.; Patchkovskii, S.; Lim, E. C. *J. Chem. Phys.* **2005**, *123*, 081101.

[15] Zgierski, M. Z.; Patchkovskii, S.; Fujiwara, T.; Lim, E. C. *J. Phys. Chem. A* **2005**, *109*, 9384.

[16] Zgierski, M. Z.; Fujiwara, T.; Lim, E. C. *Chem. Phys. Lett.* **2008**, *463*, 289.

[17] Merchán, M.; González-Luque, R.; Climent, T.; Serrano-Andrés, L.; Rodríguez, E.; Reguero, M.; Peláez, D. *J. Phys. Chem. B* **2006**, *110*, 26471.

[18] Serrano-Andrés, L.; Merchán, M. *J. Photochem. Photobiol. C: Photochem. Rev.* **2009**, *10*, 21.

[19] Kistler, K. A.; Matsika, S. *J. Phys. Chem. A* **2007**, *111*, 2650.

[20] Kotur, M.; Weinacht, T. C.; Zhou, C.; Kistler, K. A.; Matsika, S. *J. Chem. Phys.* **2011**, *134*, 184309.

[21] Blancafort, L. *Photochem. Photobiol.* **2007**, *83*, 603.

[22] Kistler, K. A.; Matsika, S. *J. Chem. Phys.* **2008**, *128*, 215102.

[23] Barbatti, M.; Aquino, A. J. A.; Szymczak, J. J.; Nachtigallová, D.; Hobza, P.; Lischka, H. *Proc. Natl. Acad. Sci. U.S.A.* **2010**, *107*, 21453.

[24] Hudock, H. R.; Martínez, T. J. *ChemPhysChem* **2008**, *9*, 2486.

[25] González-Vázquez, J.; González, L. *ChemPhysChem* **2010**, *11*, 3617.

[26] Barbatti, M.; Aquino, A. J. A.; Szymczak, J. J.; Nachtigallová, D.; Lischka, H. *Phys. Chem. Chem. Phys.* **2011**, *13*, 6145.

[27] Richter, M.; Marquetand, P.; González-Vázquez, J.; Solá, I.; González, L. *J. Phys. Chem. Lett.* **2012**, *3*, 3090.

[28] Lan, Z.; Fabiano, E.; Thiel, W. *J. Phys. Chem. B* **2009**, *113*, 3548.

[29] González-Luque, R.; Climent, T.; González-Ramírez, I.; Merchán, M.; Serrano-Andrés, L. *J. Chem. Theory Comput.* **2010**, *6*, 2103.

[30] Nakayama, A.; Harabuchi, Y.; Yamazaki, S.; Taketsugu, T. *Phys. Chem. Chem. Phys.* **2013**, *15*, 12322.

[1] Bazyl, O. K.; Chaikovskaya, O. N.; Artyukhov, V. Y. *Opt. Spectrosc.* **2005**, *98*, 838.

[2] Bazyl, O. K.; Chaikovskaya, O. N.; Artyukhov, V. Y.; Maier, G. V. *Opt. Spectrosc.* **2004**, *97*, 42.

[3] Catastini, C.; Sarakha, M.; Mailhot, G.; Bolte, M. *Sci. Total Environ.* **2002**, *298*, 219.

[4] Franck, R.; Klopffer, W. *Chemosphere* **1988**, *17*, 985.

[5] Catastini, C.; Sarakha, M.; Mailhot, G. *Int. J. Environ. Anal. Chem.* **2002**, *82*, 591.

[6] Roos, B. O.; Fülscher, M. P.; Malmqvist, P-Å.; Serrano-Andrés, L.; Pierloot, K.; Merchán, M. *Adv. Chem. Phys.* **1996**, *93*, 219.

[7] Serrano-Andrés, L.; Merchán, M.; Nebot-Gil, I.; Lindh, R.; Roos, B. O. *J. Chem. Phys.* **1993**, *98*, 3151.

[8] Serrano-Andrés, L.; Merchán, M.; Borin, A. C. *Proc. Natl. Acad. Sci. U.S.A.* **2006**, *103*, 8691.

[9] Serrano-Andrés, L.; Merchán, M.; Lindh, R. *J. Chem. Phys.* **2005**, *122*, 104.

[10] Aquilante, F.; De Vico, L.; Ferré, N. *J. Comput. Chem.* **2010**, *31*, 224.

[11] Frisch, M. J.; Trucks, G. W.; Schlegel, H. B.; et al. *Gaussian 09*; Gaussian Inc.: Wallingford, CT, 2009.

[12] Platt, J. R. *J. Chem. Phys.* **1949**, *17*, 484.

[13] Evans, D. G.; Boeyens, J. C. A. *Acta Crystallogr., Sect. B: Struct. Sci.* **1989**, *45*, 581.

[14] Palmer, I. J.; Ragazos, I. N.; Bernardi, F.; Olivucci, M.; Robb, M. A. *J. Am. Chem. Soc.* **1993**, *115*, 673.

[15] McHale, J. L. *Molecular Spectroscopy*; Prentice Hall: New York, 1999.

[16] Strickler, S. J.; Berg, R. A. *J. Chem. Phys.* **1962**, *37*, 814.

[17] Rubio-Pons, O.; Serrano-Andrés, L.; Merchán, M. *J. Phys. Chem. A* **2001**, *105*, 9664.

[18] Tatchen, J.; Gilka, N.; Marian, C. M. *Phys. Chem. Chem. Phys.* **2007**, *9*, 5209.

[19] Climent, T.; González-Luque, R.; Merchán, M.; Serrano-Andrés, L. *Chem. Phys. Lett.* **2007**, *441*, 327.

[20] Serrano-Pérez, J. J.; González-Luque, R.; Merchán, M.; Serrano-Andrés, L. *J. Phys. Chem. B* **2007**, *111*, 11880.

Chapter 5

Conclusions

5.1 Basic aromatic biological chromophores

5.1.1 1-aminonaphthalene

The photophysics of AMN has been investigated by combining experimental time-resolved transient ionization measurements with femtosecond resolution and quantum-chemical ab initio CASPT2//CASSCF theoretical calculations. The two lowest electronic excited state ^1L_b and ^1L_a of $\pi\pi^*$ character are computed to lie very close in energy, with minima at 3.50 and 3.69 eV, respectively. The bright $^1L_a\pi\pi^*$ state is essentially populated following excitation in the 330-267 nm studied region. Despite the theoretical calculations predict a surface crossing between the ^1L_a and ^1L_b states, no related signal is observed in the time-dependent measurements. According to the experimental data, the system primarily remains on the ^1L_a state after going through the crossing region, this state being responsible of the anomalous emission observed in the fluorescence spectrum. The decay lifetime observed in the transients, τ_2, shortens from nanoseconds to 13.5 ps with the exci-

tation energy in the 330-267 nm range. This lifetime is assigned at the low-energy part of the excitation range to the simultaneous relaxation of ^1L_a state by IC and ISC mechanisms. The IC is mediated by the conical intersection (CI) $(^1L_a/S_0)_{CI}$ placed 0.7 eV above the minimum, which exhibits an ethene-like CI character, i.e., a ring deformation by twisting of the carbon-carbon double-bond neighbor of the amino group. The excitation energy excess above the location of the CI decreases the excited-state lifetime from nanoseconds to picoseconds and, hence, the fluorescence quantum yield. The photophysics of the system in solution, with a internal conversion process less efficient in polar phases, is explained on the sole basis of the difference between the highly polar ^1L_a state minimum, with a partial charge-transfer character from the coplanar amino group and the less polar ground state at the $(^1L_a/S_0)_{CI}$ conformation. In polar solvents the barrier to access the CI from the ^1L_a minimum largely increases due to the relative stabilization of the latter. A similar effect is expected for the singlet-triplet gaps, in particular at the ^1L_a state minimum, where the ISC between the close-lying ^1L_a and T_2 states is more probable because of the longer lifetime of the singlet state at the minimum structure.

5.1.2 Indole, the main emissive source of proteins

On the basis of the exploration of the PEH on the low-lying singlet and triplet excited states by means of accurate state-of-the-art computational strategies, a global and comprehensive description of the photophysics of bare indole under UV irradiation is provided. Two types of processes have been identified and characterized in the molecule after excitation to the low-lying singlet valence excited states ($^1L_a\,\pi\pi^*$) and ($^1L_b\,\pi\pi^*$): radiative and nonradiative energy decays. After UV absorp-

tion, most of the molecules reach the bright ($^1L_a\,\pi\pi^*$) excited state, which may evolve through a steepest descent path toward a CI implying the ($^1L_b\,\pi\pi^*$) state, mediating in this manner its population. The relaxed structure $(^1L_b)_{min}$ on the S_1 hypersurface might be accessed subsequently and from this region the fluorescence emission can take place. All the secondary energy decay paths studied also lead to the emissive state, $(^1L_b)_{min}$. A radiationless decay specific to the ($^1L_b\,\pi\pi^*$) state has been predicted involving a nonplanar ethene-like CI between ($^1L_b\,\pi\pi^*$) and the ground state. According to the obtained pathways profiles, the process is inhibited at the energy around the ($^1L_b\,\pi\pi^*$) band origin and becomes competitive with the fluorescence emission at excitation energies close the ($^1L_a\,\pi\pi^*$) band maximum. The current findings explain for the first time the low fluorescence quantum yield measured experimentally after excitation to energy lower that 5.00 eV because of the presence of a not previously reported nonradiative decay mechanism specific for the ($^1L_b\,\pi\pi^*$) state. No efficient intersystem crossings have been found along the decay paths analyzed. The phosphorescence properties are in agreement with previous theoretical and experimental studies.

Two additional comments are appropriate at this final stage. Firstly, as many other organic molecules, the nonradiative decay to the ground state of excited indole is mediated by the presence of an ethene-like CI. For instance, the photostability of the natural purine and pyrimidine nucleobases has been proven to be determined by the presence of easily accessible ethene-like CI, which provides the molecules with nonradiative paths to release the absorbed energy in an ultrafast manner [1,2,3-8]. The present study on the photophysics of bare indole further highlights the importance of such type of degenerate regions, which can be considered nowadays as a well-established concept in the field of effi-

cient nonradiative decay funnels of organic systems. Secondly, since the topology of indole and the canonical nucleobase 9H-adenine are similar, that is, they are both built as six- and five-fused rings and the molecules have the same energetic ordering of the lowest ($^1L_b\,\pi\pi^*$) and ($^1L_a\,\pi\pi^*$) states at the FC region, the photophysics of 9H-adenine [3-7] might be compared with the results obtained here. The presence of a main nonradiative decay path toward the ground state, after excitation to the bright state, associated with an ethene-like CI appears as a common feature between the two systems, although involving the ($^1L_b\,\pi\pi^*$) and ($^1L_a\,\pi\pi^*$) states in indole and 9Hadenine, respectively. This can be ascribed to the different nature of the double bond implied in the CI of indole and 9H-adenine ($C_6 = C_7$ versus $C_2 = N_3$) and can consequently be related to the intrinsic nature of the two molecules.

5.2 DNA related chromophores

5.2.1 Thymine-Thymine (6-4) adduct, a DNA photolesion

On the basis of ab initio CASPT2//CASSCF quantum-chemical calculations, we have studied in the present contribution the photoinduced process that leads the system consisting of two adjacent thymine molecules (TT) to the formation of the thymine-thymine (6-4) adduct, with the aim of elucidating the key drivers of the global photochemical event.

One of the main conclusions of our work is that in order to activate the photoinduced process, the initial excitation has to be localized on a single nucleobase. Such a condition determines the intrinsic photostability against thymine-thymine (6-4) adduct formation because it is well-known that the main photoresponse of thymine is the ultrafast

decay to the original ground state. The requirement of a localized excitation is due to the possibility that along the decay path of the bright $^1(\pi\pi^*)$ state of thymine, the dark $(n\pi^*)$ states might be populated. This is in turn a key driver of the global mechanism because it enables the T' nucleobase to evolve in a reactive conformation prone to interact with the adjacent thymine. The $^3(n\pi^*)_{min-TT}$ geometry is in fact characterized by a strongly elongated $C_{4'} = O$ bond, determining its ability to react with the $C_5 = C_6$ double bond of the T moiety along the described path mediated by the presence of the $(^3n\pi^*/^3\pi\pi^*)_{CI-TT}$ structure and the $(^3\pi\pi^*/gs)_{STC-TT}$ intersystem crossing region.

Another important conclusion is that the triplet states are involved in the formation of the thymine-thymine (6-4) adduct. As pointed out above, the initial step of the process might take place along the $^1(n\pi^*)$ state, the only barrierless path connecting the $^3(n\pi^*)_{min-TT}$ structure with the $(^3\pi\pi^*/gs)_{STC-TT}$ region is along the triplet state $^3(\pi\pi^*)$. In agreement with our findings, the importance of the triplet states in the Paternò-Büchi reaction involving aromatic carbonyl compounds has been highlighted in a recent femtosecond study, which has shown that for their model, the ISC rate exceeds the rate of the singlet reaction and that, consequently, the photoprocess will mainly take place along the triplet manifold [9]. The participation of triplet states in the mechanism is an important clue in order to study the rate of formation of such a photoproduct, which, to the best of our knowledge, has not been already experimentally determined. The only information regarding the timescales for thymine-thymine (6-4) adduct formation has been provided by transient absorption experiments performed by Marguet and Markovitsi [10]. They conclude that the photoproduct is formed within 4 ms via a reaction intermediate. Such a time scale is plausible with the described mechanism involving two singlet- triplet crossing processes,

although the possibility of an ultrafast reaction under favorable ISC conditions cannot be excluded.

5.2.2 Cytosine, a DNA building block chromophore

The published studies on the primary photophysical and photochemical events that follow the photoinduced population of the bright state $^1(\pi\pi^*)$ of the canonical nucleobases cytosine have been here critically analyzed. It has emerged that the cytosine system can decay back to the original ground state along three main decay channels, each one characterized by a different CI involving the ground and the lowest singlet excited state. In the first obtained relaxation path, the main feature of the involved CI is a single-double bond inversion with respect to the equilibrium geometry of the ground state, and a slight pyramidalization of the C_6 atom. According to the second possible decay mechanism, the bright excited state $^1(\pi\pi^*)$ of the molecule will reach a degenerate region with the ground state that describes a localized distortion on the carbon-carbon double bond, similar to the one found in the CI obtained in ethene. The third and last relaxation path proceeds through the population of a CI characterized by a strong bending of the amino group out of the plane of the ring. Despite the large amount of research performed up to now, it is not totally clear the relative photochemical relevance of each of these paths, and it is still under debate the possibility for the bright state $^1(\pi\pi^*)$ to reach a weakly bound minimum region. It is worth pointing out that even in the latter case the energy barriers found in order to surmount the minimum region and decay to one of the three CIs are low enough to be consistent with an efficient and ultrafast decay from the bright excited state to the ground state. In the context of the present thesis, a minimum energy path (MEP) calculation at the

CASPT2//CASPT2 level has been undertaken employing the whole π system of the molecule as active space, and the ANO-L basis set contracted to O,C,N [4s,3p,1d]/ H[2s1p]. The results derived from such a highly computationally demanding benchmark point out to the presence of a weakly bound minimum. Ongoing research further indicates that it is connected by surmounting an small energy barrier to a bond-inversion type CI involving the ground state.

5.3 Chromophores introduced by humans

5.3.1 Asulam, a widely used pesticide

A combined experimental and quantum-chemical research at the CASPT2 level have been performed in order to unveil the photophysical behavior of asulam. Two low-lying singlet excited states, labeled as S_1 ($^1L_b\,\pi\pi^*$) and S_2 ($^1L_a\,\pi\pi^*$), have been characterized. The absorption band maximum has been assigned to the S_2 ($^1L_a\,\pi\pi^*$) state, whereas the lowest-lying state S_1 ($^1L_b\,\pi\pi^*$) has been found to be responsible for the fluorescence spectrum. Fluorescence quantum yield at room temperature is low and varies with the solvent, highest in water ($\phi_f = 0.16$) and independent of its acidity ($3 < \mathrm{pH} < 11$), and lowest in methanol and 1-propanol (ϕ_f ca. 0.02). Fluorescence lifetime in aqueous solution is 1 ns ($k_f = 1,5\,10^{-8}s^{-1}$). There is an efficient intersystem crossing from the phosphorescence quantum yield found in glassy ethanol ($\phi_p = 0.36$) at 77 K, the phosphorescence lifetime being 1.1 s. Thus, the remaining 48% decays through nonradiative pathways. In agreement with such outcomes, the decay pathway of the spectroscopic S_2 ($^1L_a\,\pi\pi^*$) state can be considered barrierless from the FC structure toward the region of the internal conversion between the ground and the lowest singlet

excited state, $(gs/\pi\pi^*)_{CI}$. Along the main decay path, the presence of a CI between the two low-lying singlet excited states switches part of the population to the fluorescent ($^1L_b\,\pi\pi^*$) state, which decays to its emitting minimum. Different intersystem crossing regions have been also characterized on the potential energy hypersurface (PEH) connecting the FC region and the $(gs/\pi\pi^*)_{CI}$, which accounts for the phosphorescent features detected experimentally. Finally, the minimum of the emitting triplet state might reach an intersystem crossing region $(^1gs/^3L_a{}^*)_{STC}$ surmounting a barrier of 0.41 eV, which constitutes a second nonradiative decay path to the ground state.

5.4 References

[1] Merchán, M.; González-Luque, R.; Climent, T.; Serrano-Andrés, L.; Rodríguez, E.; Reguero, M.; Peláez, D. *J. Phys. Chem. B* **2006**, *110*, 26471.

[2] Serrano-Andrés, L.; Merchán, M.; Borin, A. C. *J. Am. Chem. Soc.* **2008**, *130*, 2473.

[3] Perun, S.; Sobolewski, A. L.; Domcke, W. *J. Am. Chem. Soc.* **2004**, *127*, 6257.

[4] Blancafort, L. *J. Am. Chem. Soc.* **2006**, *128*, 210.

[5] Serrano-Andrés, L.; Merchán, M.; Borin, A. C. *Chem. Eur. J.* **2006**, *12*, 6559.

[6] Serrano-Andrés, L.; Merchán, M.; Borin, A. C. *Proc. Natl. Acad. Sci. U.S.A.* **2006**, *103*, 8691.

[7] Conti, I.; Garavelli, M.; Orlandi, G. *J. Am. Chem. Soc.* **2009**, *131*, 16108.

[8] Gobbo, J. P.; Borin, A. C.; Serrano-Andrés, L. *J. Phys. Chem. B* **2011**, *115*, 6243.

[9] Brogaard, R. Y.; Schalk, O.; Boguslavskiy, A. E.; Enright, G. D.; Hopf, H.; Raev, V.; Tarcoveanu, E.; Sølling, T. I.; Stolow, A. *Phys. Chem. Chem. Phys.* **2012**, *14*, 8572.

[10] Marguet, S.; Markovitsi, D. *J. Am. Chem. Soc.* **2005**, *127*, 5780.

Chapter 6

Resumen

La presente tesis se enmarca dentro de las líneas de investigación del grupo QCEXVAL, y en particular en el estudio de la fotofísica y fotoquímica de cromóforos de interés biológico. A continuación, se van a resumir los resultados obtenidos en los cinco trabajos publicados y presentados en esta tesis: la fotofísica de la molécula 1-aminonaftaleno, la fotofísica del cromóforo indol, el mecanismo fotoinducido de formación del fotodímero (6-4) timina-timina, el estudio y descripción crítica de la principal vía de decaimiento no-radiativo en la citosina, y la respuesta del herbicida asulam frente a la radiación UVA y UVB.

Los estudios teóricos han sido realizados utilizando principalmente el protocolo CASPT2//CASSCF, en el cual las optimizaciones geométricas (búsqueda de mínimos, caminos de mínima energía, etc.) se efectúan a nivel CASSCF, y para cada geometría y camino así obtenidos, se recalcula la energía utilizando el método CASPT2. Dicho protocolo resulta ser particularmente apto para el estudio de procesos fotofísicos y fotoquímicos, siendo capaz de describir el carácter multiconfiguracional del sistema (a través del cálculo CASSCF) y de considerar en suficiente me-

dida la correlación dinámica (a través del sucesivo cálculo CASPT2). El principal objetivo del trabajo reside en la descripción de los procesos fotoinducidos más probables que tienen lugar tras la absorción de luz ultravioleta. Los principios de la llamada aproximación del camino reactivo fotoquímico (*photochemical reaction path approach*) se han tenido en cuenta, considerando los posibles procesos de decaimiento que el sistema puede sufrir, los cuales quedan determinados principalmente por las características topográficas de las superficies de energía potencial de los estados involucrados. Por tanto, se ha prestado una atención especial a la determinación de los caminos de mínima energía que el sistema puede experimentar, y a las posibles barreras energéticas que separan las regiones de mayor interés.

6.1 Cromóforos aromáticos de importancia biológica fundamental

6.1.1 1-aminonaftaleno

El interés de dicha molécula se enmarca en el estudio de los cromóforos de base aromática, y también en que permite analizar los efectos que ocasiona en las propiedades fotofísicas y fotoquímicas del sistema la introducción de un grupo funcional adicional en el propio cromóforo. Efectivamente, el sistema 1-aminonaftaleno puede ser visto como una molécula de naftaleno en la cual un átomo de hidrógeno ha sido sustituido por un grupo amino. La caracterización de su fotofísica y fotoquímica proporciona, por tanto, información útil para la descripción de sistemas más complejos relacionados con la molécula objeto de estudio, así como para la determinación de las características intrínsecas de la propia molécula de naftaleno y de los efectos imputables a la presencia

del grupo amino. Dicho trabajo ha sido realizado en colaboración con el grupo experimental del Profesor Fernando Castaño de la Universidad del País Vasco, y nos ha permitido comparar directamente los resultados teóricos con los hallazgos experimentales.

El espacio activo de 12 electrones y 11 orbitales ha sido utilizado, CASSCF(12,11). En todos los cálculos el conjunto de base ANO-S contraída según el esquema C,N [3s,2p,1d]/ H[2s,1p] ha sido empleado. Cuatro estados han sido calculados y, por tanto, utilizados en el proceso de optimización de los orbitales (*state averaging*). Dicho estudio ha sido realizado empleando el programa MOLCAS 6.

La optimización del estado fundamental converge a una estructura en la cual el grupo amino está fuera del plano descrito por los anillos aromáticos. Los ángulos diedros $H_{1a}NC_1C_{10}$ y $H_{1b}NC_1C_2$ de ello, los cuales caracterizan la posición del grupo amino con respecto al plano del naftaleno, resultan ser 49.9° y 10.2°, respectivamente. En dicha geometría los primeros estados excitados singlete corresponden, utilizando la nomenclatura de Platt, a los estados $^1(L_b\,\pi\pi^*)$ y $^1(L_a\,\pi\pi^*)$, situados a 3.80 y 4.35 eV, respectivamente, desde el mínimo del estado fundamental.

El mismo tipo de estados y con el mismo orden energético se encuentra también para el sistema naftaleno. La fuerza de oscilador asociada a la transición al estado $^1(L_a\,\pi\pi^*)$ es dos veces el orden de magnitud de la calculada para la transición al estado $^1(L_b\,\pi\pi^*)$. Como consecuencia de ello, el estado $^1(L_a\,\pi\pi^*)$ resulta ser el estado más brillante del sistema, a partir del cual los principales procesos fotoquímicos tendrán lugar. Con el fin de estudiar la evolución del sistema una vez excitado, se ha determinado el camino de mínima energía en el estado $^1(L_a\,\pi\pi^*)$ partiendo de la geometría de Franck-Condon. El análisis de los resultados correspondientes nos permite concluir que el estado $^1(L_a\,\pi\pi^*)$ puede

evolucionar a lo largo de un camino sin barrera hacia una región de intersección cónica con el estado $^1(L_b\,\pi\pi^*)$, llegando finalmente a una región de mínimo. La presencia de dicha región de degeneración hace suponer que parte de la población del estado $^1(L_a\,\pi\pi^*)$ pueda pasar al estado $^1(L_b\,\pi\pi^*)$. No obstante, los datos experimentales obtenidos en la escala de los femtosegundos no detectaron tal transición. Desde la geometría de cruce, el estado $^1(L_b\,\pi\pi^*)$ puede evolucionar a una estructura de mínimo. Los orígenes de banda de los estados $^1(L_a\,\pi\pi^*)$ y $^1(L_b\,\pi\pi^*)$ se evalúan en 3.69 y 3.50 eV, respectivamente. Ambos resultados confirman un desplazamiento hacia el rojo de las bandas de fluorescencia del sistema con respecto a la molécula de naftaleno, cuyo origen de banda está situado a 3.96 eV. La producción de emisión no es el único mecanismo de desactivación operativo en la molécula de 1-aminonaftaleno. De hecho, una intersección cónica entre el estado $^1(L_a\,\pi\pi^*)$ y el estado fundamental ha sido identificada, la cual puede mediar un proceso de conversión interna hacia el estado fundamental. Dicha geometría se caracteriza por una distorsión localizada en el doble enlace $C_2 = C_3$, el cual experimenta una torsión típica de las llamadas cónicas de tipo eteno. De esta forma, el sistema 1-aminonaftaleno constituye otro ejemplo de cromóforo aromático donde una cónica de tipo eteno juega un papel significativo. La región de degeneración está situada a 0.7 eV con respecto al mínimo del estado $^1(L_a\,\pi\pi^*)$. Su importancia en la fotoquímica del sistema queda por tanto ligada a la energía en exceso proporcionada. Dicha circunstancia explica los resultados experimentales obtenidos en la escala de picosegundos, los cuales registran un tiempo de vida media que disminuye al aumentar la energía de la radiación de excitación. Al aumentar la energía proporcionada al sistema, se favorece la posibilidad de alcanzar la región de intersección cónica con el estado fundamental y como consecuencia el tiempo de vida medio del estado

excitado será menor. La presencia de un mecanismo de desactivación no radiativo se había identificado experimentalmente con anterioridad para varios derivados de 1-aminonaftaleno en diferentes solventes. Se había detectado que en general la eficiencia del proceso de conversión interna disminuye al aumentar la polaridad del solvente. Utilizando los resultados obtenidos, podemos justificar dicho comportamiento en base a los diferentes valores del momento dipolar de los estados implicados. En el mínimo del estado $^1(L_a\,\pi\pi^*)$ el sistema presenta un momento dipolar mucho más alto que en la cónica con el estado fundamental (5.54 y 1.20 D, respectivamente) y, por tanto, un aumento de la polaridad del entorno determinará una mayor estabilización del mínimo $^1(L_a\,\pi\pi^*)$ con respecto a la región de cónica, ocasionando una mayor barrera energética que tiene que ser superada con objeto de activar el mecanismo de conversión interna.

6.1.2 Indol, la principal fuente de emisión en las proteínas

Esta molécula resulta ser de particular importancia ya que es el cromóforo presente en diferentes compuestos bioquímicos, tales como el aminoácido esencial triptófano, el neurotransmisor serotonina y otros análogos moleculares de interés. Debido a la diferente respuesta fotoinducida del indol dependiendo del entorno en el cual se encuentra, es posible obtener información estructural de proteínas que contienen el aminoácido triptófano. Por ejemplo, si una proteína en solución acuosa presenta una estructura para la cual el aminoácido triptófano está rodeado por el solvente, entonces su emisión será diferente de aquella en la que el cromóforo esté rodeado por otros aminoácidos de la macromolécula proteica.

El espacio activo de 10 electrones y 9 orbitales ha sido utilizado, CASSCF(10,9), lo cual corresponde a todo el espacio π del sistema. En todos los cálculos el conjunto de base ANO-L contraída según el esquema C,N [4s,3p,1d]/ H[2s,1p] ha sido empleado. Cuatro estados han sido calculados y, por tanto, utilizados en el proceso de optimización de los orbitales (*state averaging*). Dicho estudio ha sido realizado empleando el programa MOLCAS 7.4.

Se ha realizado un estudio exhaustivo de los posibles procesos inducidos en la molécula de indol como consecuencia de la interacción con radiación UV. A la geometría optimizada para el estado fundamental, los dos estados excitado singlete más bajos han resultado ser, utilizando la nomenclatura de Platt, $^1(L_b\,\pi\pi^*)$ y $^1(L_a\,\pi\pi^*)$. Dichos estados están situados verticalmente a 4.36 y 4.79 eV, respectivamente, desde el mínimo del estado fundamental. El cálculo de la fuerza de oscilador para las respectivas transiciones electrónicas nos ha permitido identificar el $^1(L_a\,\pi\pi^*)$ como el estado excitado más brillante, a partir del cual los procesos fotoquímicos y fotofísicos más relevantes del sistema tendrán lugar. De todas formas, la diferencia de fuerza de oscilador para las transiciones hacia los estados $^1(L_a\,\pi\pi^*)$ y $^1(L_b\,\pi\pi^*)$ no es tan grande como para excluir la posibilidad de que el estado $^1(L_b\,\pi\pi^*)$ sea poblado directamente. El cálculo del camino de mínima energía en el estado $^1(L_a\,\pi\pi^*)$ nos ha permitido estudiar la evolución del sistema. Dicho estado alcanza una región de intersección cónica con el estado $^1(L_b\,\pi\pi^*)$ y, por tanto, parte de la población del primer estado excitado puede pasar al estado $^1(L_b\,\pi\pi^*)$. Este último evoluciona hacia una estructura de mínimo, desde la cual se produce la fluorescencia típica del sistema indol. El origen de banda calculado para el estado $^1(L_b\,\pi\pi^*)$ es igual a 4.11 eV. Esta misma región de equilibrio ha sido determinada por medio del cálculo del camino de mínima energía en el estado $^1(L_b\,\pi\pi^*)$ desde

la geometría Franck-Condon. Dicho resultado corrobora la importancia de la estructura de mínimo del estado $^1(L_b\,\pi\pi^*)$ para el proceso de fluorescencia en el indol. Estos fenómenos constituyen los principales decaimientos experimentados por el sistema. En función de la energía de excitación dada a la molécula, otros mecanismos de desactivación también pueden ser activados. De hecho, un proceso no-radiativo estrictamente relacionado con el exceso de energía presente en el sistema, mediado por una intersección cónica entre el estado $^1(L_b\,\pi\pi^*)$ y el estado fundamental situada a 0.4 eV respecto al mínimo del estado $^1(L_b\,\pi\pi^*)$, también ha sido caracterizado. La presencia de dicha barrera energética explica la fuerte disminución del rendimiento de fluorescencia observada experimentalmente al aumentar la energía de excitación. Previamente a este trabajo otro mecanismo no-radiativo de desactivación había sido propuesto, involucrando a la población de un estado $\pi\sigma^*$ repulsivo y a un sucesivo proceso de conversión interna a través de una intersección cónica con el estado fundamental. Aunque este último mecanismo puede ser plausible, el proceso no-radiativo aquí descrito y mediado por la cónica entre el estado $^1(L_b\,\pi\pi^*)$ y el estado fundamental requiere un menor exceso de energía para poder ser activado.

6.2 Cromóforos relacionados con el ADN

6.2.1 Aducto Timina-Timina (6-4), una fotolesión del ADN

Los procesos fotofísicos y fotoquímicos del ADN constituyen fenómenos de fundamental interés. Entre ellos, es de destacar la formación de fotodímeros pirimidínicos inducidos por irradiación con luz UV. Dos clases de compuestos se han encontrado con más frecuencia. Los dímeros llamados [2+2], en los cuales se produce una reacción de cicloadición entre

los dos dobles enlaces carbono-carbono de las bases pirimidínicas, y los dímero (6-4), cuya formación es debida a la reacción entre el doble enlace carbono-carbono de una base pirimidínica y el enlace carbonilo o el grupo amino de otra nucleobase. Estos últimos conllevan la formación de una estructura de tipo oxetano o azedina, que sucesivamente evoluciona por vía térmica al fotoproducto final.

Debido a que el principal objetivo del trabajo ha sido el estudio del mecanismo de una reacción cuyo rendimiento cuántico es muy bajo, el llamado "*photochemical reaction path approach*", capaz de describir los principales procesos fotoinducidos, resulta en el presente caso de poca utilidad. El trabajo ha sido realizado a través de la verificación por medio de cálculos químico-cuánticos de diferentes hipótesis, basadas en la experiencia del grupo en la fotoquímica de las nucleobases, así como en los datos disponibles en la literatura. Muchos cálculos realizados se han basado en la técnica de interpolación lineal de las coordenadas internas entre dos estructuras de interés. Dicha estrategia permite obtener un camino conectado entre dos geometrías y ha sido utilizada para determinar la importancia de diferentes regiones de la superficie de energía potencial en la reacción estudiada. El espacio activo ha constado de doce electrones y doce orbitales, CASSCF(12,12), empleando el conjunto de base ANO-S contraída según el esquema O,C,N [3s,2p,1d]/ H[2s,1p]. Dos estados han sido calculados, y por tanto, utilizados en el proceso de optimización de los orbitales (*state averaging*), aunque varios cálculos con un número mayor de raíces han sido efectuados con el fin de explorar los estados de más alta energía. Dicho estudio ha sido realizado empleando el programa MOLCAS 7.4.

En este estudio se ha determinado un posible mecanismo de formación del aducto timina-timina (6-4). Como modelo se ha utilizado un sistema compuesto por dos moléculas de timina posicionadas en la ge-

ometría en la que se encuentran en una misma hebra de B-ADN. El mecanismo obtenido describe un posible camino de reacción a partir de la absorción de radiación por el sistema hasta la formación del intermedio oxetano. En dicha orientación, los estados excitados singlete más brillantes son los correspondientes a dos moléculas de timina aisladas y, por tanto, describen excitaciones $\pi\pi^*$ localizada cada una en el doble enlace carbono-carbono de una nucleobase. La clave para que el proceso fotoquímico tenga lugar ha sido identificada en la población de los estados $^{1,3}n\pi^*$ localizados en el grupo carbonilo reactivo, los cuales evolucionan a una estructura de mínimo caracterizada por un fuerte alargamiento del enlace carbono-oxígeno. Dichos estados $^{1,3}n\pi^*$ pueden ser poblados a lo largo del camino principal de decaimiento descrito por el estado brillante $^1\pi\pi^*$ de la correspondiente nucleobase. Debido a la distorsión presente en la geometría de mínimo $^{1,3}n\pi^*$, el oxígeno originalmente constituyente del grupo carbonilo se encuentra enlazado a la molécula por un enlace doble debilitado y, como consecuencia, puede reaccionar más fácilmente con el doble enlace carbono-carbono de otra nucleobase timina. Dicha reacción tiene lugar a través del estado de triplete más bajo, $^3\pi\pi^*$, el cual puede ser poblado debido a la presencia de un región de degeneración entre los estados $^3\pi\pi^*$y $^{1,3}n\pi^*$, accesible desde el mínimo de los estados $^{1,3}n\pi^*$. El estado $^3\pi\pi^*$ puede sucesivamente evolucionar hacia una región de degeneración con el estado fundamental, a lo largo de un camino en la correspondiente superficie de energía potencial en el cual los dos monómeros se van acercando, estando ya parcialmente enlazados en la geometría final de cruce. La reacción entre las dos moléculas de timina determina que el estado triplete $^3\pi\pi^*$, inicialmente localizado en una sola nucleobase, se transforma finalmente en un estado de transferencia de carga implicando a los dos monómeros. A partir de dicha región de degeneración, el estado fun-

damental así poblado puede evolucionar hacia la estructura oxetano, cuya formación constituye la parte fotoinducida del mecanismo global de producción del aducto timina-timina (6-4). El punto de partida del mecanismo presentado lo constituye la población de los estados $^{1,3}n\pi^*$ desde el estado brillante $^1\pi\pi^*$ a lo largo de su camino de desactivación. Dicha característica permite que la radiación absorbida sea disipada eficazmente de forma no radiativa. Por tanto, el mecanismo de formación aquí descrito, tiene lugar a partir de una situación en la cual la mayoría de la población del estado brillante decae hacia el estado fundamental. Este hecho puede explicar el bajo rendimiento cuántico de formación de dicho producto, más de un orden de magnitud menor con respecto a los fotodímeros ciclobutano.

6.2.2 Citosina, un cromóforo del ADN

El ADN es químicamente un polímero compuesto por unidades que se repiten llamadas nucleótidos. Estos últimos están formados por una nucleobase, un azúcar, y un grupo fosfato. En el ADN hay cuatro tipos de bases, entre las cuales está la nucleobase pirimidínica citosina. Como consecuencia, la determinación de la fotorespuesta de la citosina a la luz UV se enmarca tanto en la investigación de cromóforos de interés biológico fundamental, como en el estudio de la fotofísica y fotoquímica del ADN.

Debido a la importancia del tema, numerosos estudios teórico han sido realizados con el fin de dilucidar la fotoquímica de la citosina. Desde 2002, tres diferentes mecanismos de decaimiento no-radiativo han sido descritos empleando diferentes métodos de estructura electrónica y varias estrategias para explorar las regiones de las superficies de energía potencial más relevantes. Dichos mecanismos conllevan la presencia

de una intersección cónica fácilmente accesible entre el estado excitado singlete más bajo y el estado fundamental. Cada uno de los tres procesos diferentes está caracterizado por una intersección cónica concreta. El primer camino de desactivación es mediado por una estructura de degeneración energética en la cual los dobles y simples enlaces de la molécula resultan invertidos con respecto a la geometría de mínimo del estado fundamental y el carbono C_6 está ligeramente piramidalizado. El decaimiento a través de esta intersección cónica ha sido caracterizado como el más importante utilizando tanto el método CASSCF como el protocolo CASPT2//CASSCF. La segunda posible vía de desactivación presenta una intersección cónica de tipo eteno, cuya distorsión principal está localizada en el doble enlace carbono-carbono, y determina que el átomo de hidrógeno H_5 esté casi perpendicular al plano de la molécula. La relevancia de este mecanismo ha sido demostrada efectuando cálculos CASPT2//CASSCF, MS-CASPT2//MS-CASPT2, DFT/MRCI, TDDFT, CR-EOM-CCSD(T)/CIS y MRCI. El tercer mecanismo de desactivación conlleva una intersección cónica caracterizada por una fuerte distorsión localizada en el grupo amino, la cual determina que dicho grupo se encuentre perpendicular al plano de la molécula. Esta última posibilidad de decaimiento ha sido obtenida en diferentes estudios. A pesar de eso, sólo en un trabajo realizado a nivel MRCI se considera dicho camino como el más relevante para la fotofísica de la molécula citosina.

En el contexto de la tesis doctoral, se ha realizado el cálculo de camino de mínima energía a nivel CASPT2//CASPT2 en el estado brillante $\pi\pi^*$ a partir de una geometría de mínimo del estado fundamental previamente publicada. En el espacio activo han sido considerados todos los orbitales de tipo π de la molécula. El conjunto de base ANO-L contraída según el esquema O,C,N [4s,3p,1d]/ H[2s1p] ha sido

empleado, utilizando dos estados en el proceso de optimización de los orbitales (*state averaging*). Dicho estudio ha sido realizado empleando el programa MOLCAS 7.6. Según los resultados obtenidos, el camino de mínima energía que caracteriza el estado excitado brillante $\pi\pi^*$ lleva a una geometría de mínimo.

Es de destacar que, a diferencia de uracilo y timina, cabe la posibilidad de que la citosina no decaiga a lo largo de un camino sin barreras hacia una cónica de tipo eteno. La razón intrínseca para dicho comportamiento podría estar relacionada con la presencia del doble enlace carbono-nitrógeno, ausente en las otras nucleobases canónicas pirimidínicas.

6.3 Cromóforos introducidos por los humanos

6.3.1 Asulam, un pesticida ampliamente utilizado

Los problemas causados por la intervención masiva del hombre en el ecosistema ha incentivado la búsqueda de procesos y productos cuyo impacto ambiental sea lo más reducido posible. Entre otras estrategias, se han investigado las moléculas fotodegradables, entre las que se encuentran los pesticidas. La molécula asulam es un herbicida perteneciente a la familia de los compuestos carbamato, que son aquellos sistemas orgánicos derivados del ácido carbámico. El interés del estudio de la fotofísica y fotoquímica de la molécula asulam se encuadra en la investigación enfocada al desarrollo de compuestos fotodegradables. Siendo el asulam un pesticida ampliamente utilizado para el control de helechos, la determinación de sus características fotofísica y fotoquímicas puede proporcionar información útil para la posible producción de pesticidas fotodegradables.

El espacio activo de seis electrones y seis orbitales ha sido utilizado, CASSCF(6,6), haciendo uso del conjunto de base ANO-S contraída según el esquema S [4s,3p,1d]/ O,C,N [3s,2p,1d]/ H[2s]. Cuatro estados han sido calculados en el proceso de optimización de los orbitales (*state averaging*). Dicho estudio ha sido realizado empleando el programa MOLCAS 7.2.

A la geometría optimizada del estado fundamental, los estados excitados singlete más bajos en energía son los denominados, según la notación de Platt, $^1(L_b\,\pi\pi^*)$ y $^1(L_a\,\pi\pi^*)$, y están situados a 4.36 y 5.02 eV, respectivamente. Siendo la fuerza de oscilador asociada a la transición al estado $^1(L_a\,\pi\pi^*)$ dos veces el orden de magnitud que la correspondiente al estado $^1(L_b\,\pi\pi^*)$, el estado $^1(L_a\,\pi\pi^*)$ puede ser considerado el más brillante. La transición a otro estado excitado singlete también posee un elevado valor de la fuerza de oscilador. A pesar de eso, la fotoquímica del sistema desde este estado no ha sido considerada debido a que la radiación necesaria para poblarlo no está comprendida en el rango asociado a la radiación UVA y UVB. El camino de mínima energía en el estado $^1(L_a\,\pi\pi^*)$ desde la geometría de Franck-Condon lleva a través de un camino sin barreras a una región de intersección cónica entre el estado $^1(L_a\,\pi\pi^*)$ y el estado fundamental. En esta geometría de degeneración, el anillo bencénico asume una conformación bote, un tipo de geometría conocida en la fotofísica del benceno. De esta forma, a través de un proceso de conversión interna, el estado fundamental puede volver a la geometría de equilibrio de partida. Como consecuencia la molécula asulam resulta ser fotoestable. Sin embargo, a lo largo del mecanismo principal de desactivación descrito, otros procesos pueden tener lugar debido a la presencia de varios cruces entre estados tanto singlete como triplete. Una intersección cónica con el estado $^1(L_b\,\pi\pi^*)$ ha sido de hecho identificada, la cual determina que parte de la población del estado

$^1(L_a\,\pi\pi^*)$ pase al estado $^1(L_b\,\pi\pi^*)$. Este último, puede evolucionar hacia una estructura de mínimo, desde donde se produce la fluorescencia típica del sistema. El origen de banda calculado en dicha región es igual a 4.39 eV. Cuatro estados triplete se cruzan a lo largo del camino de mínima energía descrito por el estado $^1(L_a\,\pi\pi^*)$. Una vez poblados, decaen a través de diferentes mecanismos de conversión interna al mínimo del estado triplete más bajo de naturaleza $\pi\pi^*$. Desde esta región, el sistema puede además evolucionar hacia una región accesible de cruce con el estado fundamental. La presencia de esta última contribuye a la fotoestabilidad de la molécula de asulam.

List of terms

A

A: Absorption

AMN: 1-Aminonaphthalene

ANO-S: Small Atomic Natural Orbital

ANO-L: Large Atomic Natural Orbital

AO: Atomic Orbital

au: atomic units

B

BCH: Baker-Campbell-Hausdorff expansion

BFGS: Broyden-Fletcher-Goldfarb-Shanno Hessian update procedure

BOA: Born-Oppenheimer approximation

BSSE: Basis Set Superposition Error

C

CAM-B3LYP: Coulomb-Attenuating Method Becke 3-parameter Lee-Yang-Parr functional

CASPT2: Second-Order Perturbation Theory Complete Active Space

CASSCF: Complete Active Space Self-Consistent Field

CBT: Cyclobutane Thymine dimer

cc-pVDZ: Correlation-Consistent Valence Double-ζ plus Polarization

CI: conical intersection, Configuration Interaction

CIS: Configuration Interaction Singles

CP: counterpoise correction

CR-EOM-CCSD(T): Completely Renormalized Equation of Motion Coupled Cluster Singles, Doubles, and perturbative Triples

D

DFT: Density Functional Theory

DNA: Deoxyribonucleic Acid

DZP: Double-ζ plus Polarization

E

EET: Electronic Energy Transfer

F

F: Fluorescence

FC: Franck-Condon

G

gs: Ground State

H

HF: Hartree-Fock

HOMO: Highest Occupied Molecular Orbital

I

IC: Internal Conversion process

ICMol: Instituto de Ciencia Molecular

IRC: Intrinsic Reaction Coordinate

ISC: Intersystem Crossing process

L

LE: Locally Excited

LIF: Laser-Induced Fluorescence

LIIC: Linear Interpolation of Internal Coordinates

LUMO: Lowest Unoccupied Molecular Orbital

M

MCSCF: Multiconfigurational Self-Consistent Field

MEP: Minimum Energy Path

MO: Molecular Orbital

MRCI: Multi-Reference Interaction Configuration method

MRSDCI: Multi-Reference Singly and Doubly Excited Configuration Interaction method

MS-CASPT2: Multi-State Second-Order Perturbation Theory Complete Active Space

N

NAB: Nucleic Acid Base

NO: Natural Orbital

O

OM2: Orthogonalization Model 2

Ox: Oxetane

P

P: Phosphorescence

PBE: Perdew, Burke, and Ernzerhof functional

PEH: Potential Energy Hypersurface

PET: Photoinduced Electron Transfer

Q

QCEXVAL: Quantum Chemistry of the Excited state of Valencia

S

SDCI: Singly and Doubly Excited Configuration Interaction method

SOC: Spin-Orbit Coupling

STC: Singlet-Triplet Crossing region

T

TDDFT: Time-Dependent Density Functional Theory

TDM: Transition Dipole Moment

TT: Thymine-Thymine

TZVP: Valence Triple-ζ plus Polarization

U

UV: Ultraviolet radiation

V

vis: Visible radiation